2009-01-01

The Use of Raman Spectroscopy in the Characterization of Single Walled Carbon Nanotubes

Elizabeth Gregan
Technological University Dublin

The Use of Raman Spectroscopy in the Characterization of Single Walled Carbon Nanotubes

By

Elizabeth Gregan BSc MSc

A thesis submitted to the Dublin Institute of Technology

for the degree of Doctor of Philosophy (PhD)

School of Physics,

Dublin Institute of Technology,

Kevin Street, Dublin 8

Prof. H.J.Byrne

June 2009

Abstract

Carbon nanotubes, long, thin cylinders of carbon are intriguing structures and have sparked much excitement in recent years. It is clear that understanding the fundamental properties of nanotubes is necessary to get a realisation of the full potential of these materials. Processing and purification on a mass scale will need to be carried out if these materials are to have large scale industrial applications and move beyond the laboratory bench. Highly sensitive, capital intensive equipment such as TEM and AFM, have been used to identify the state and morphology of tube samples as well as their levels of purity, however for large scale industrial applications there is a need for routine, high throughput, cost effective methods to give the same kind of detail.

In this thesis organic solvents are used to debundle single walled nanotubes. The debundling is confirmed and the degree measured using absorption spectroscopy and also the capitally intensive and low throughput techniques, TEM and AFM. Although Raman spectroscopy is a well established technique for characterising tube bundles and single tubes little is know about what subtle changes occur in the Raman spectrum as one goes from a highly bundled state to a lower degree of bundling. In this thesis these changes are examined and the use of previously unidentified spectral markers for the degree of debundling are identified. Finally, using Raman spectroscopy a temperature dependent study was carried out. Mean free paths due to plasmon-phonon scattering in nanotube bundles and electron-phonon scattering in debundled tubes are calculated and found to be different.

DECLARATION

I certify that this thesis which I now submit for examination for the award of doctor of philosophy, is entirely my own work and has not been taken from the work of others save and to the extent that such work has been cited and acknowledged within the text of my work.

This thesis was prepared according to the regulations for postgraduate study by research of the Dublin Institute of Technology and has not been submitted in whole or in part for an award in any other Institute or University.

The work reported on in this thesis conforms to the principles and requirements of the Institute's guidelines for ethics in research.

The Institute has permission to keep, or lend or to copy this thesis in whole or in part, on condition that any such use of the material or the thesis be duly acknowledged.

Signature _____ Date ____/____/____

Candidate

ACKNOWLEDGEMENTS

I would like to acknowledge the help and encouragement of my supervisor Professor Hugh Byrne. Over the years it took to complete this work he has always been available to advise and encourage me in the good and bad times. I would also like to acknowledge the help and assistance given to me by my colleagues in the School of Physics at DIT.

I would also like to acknowledge the help of Anne Shanahan and Margurite Hughes in the aquiring of TEM and AFM images.

To my family, Eugene, David, Sarah, Ruth and Greg I wish to say a big thank you. Without your understanding and love I never would have been able to keep going.

ABBREVIATIONS

ADSWNT	Arc Discharge Single Walled Carbon Nanotubes
AFM	Atomic Force Microscopy
APS	Amino propyl silane
BWF	Breit – Wigner- Fano
CNI	Carbon Nanotechnology Incorporated
CVD	Chemical Vapour Deposition
DCB	Dichlorobenzene
DCE	Dichloroethane
DMF	Dimethylformamide
DOS	Density of States
EPC	Electron Phonon Coupling
FWHM	Full Width Half Maximum
HiPco	High Pressure Carbon Monoxide disproportionation
HPLC	High Pressure Liquid Chromatography
IR	Infrared
LO	Longitudinal Optical
LNP	Liquid Nitrogen Pump
MCB	Monochlorobenzene
NMP	N-methyl – 2-pyrrolodine
RBM	Radial Breathing Mode
STS	Scanning Tunnelling Spectroscopy
SWNT	Single Walled carbon Nanotubes

TCB	Trichlorobenzene
TEM	Transmission Electron Microscopy
TO	Transverse Optical
UVVisNIR	Ultraviolet Visible Near Infrared

TABLE OF CONTENTS

Chapter 3 Spectroscopic Techniques

Chapter 4 Raman Spectroscopy of Single Walled Carbon Nanotube Bundles

Chapter 5 Debundling Of Single Walled Carbon Nanotubes Using Organic Solvents

TABLE OF ILLUSTRATIONS

CHAPTER 1

INTRODUCTION

1.1 Introduction

The discovery of Carbon nanotubes, long, thin cylinders of carbon, is accredited to Sumio Iijima[1] in 1991. However, in 1952, Radushkevich and Lukyanovich published clear images of 50 nm diameter tubes made of carbon in the Russian Journal of Physical Chemistry[2]. More recently it has been discovered that carbon nanotubes were a component of Damascus steel, an ancient sword metal[3][4]. What is not in dispute is that carbon nanotubes are large macromolecules that are unique for their size, shape, and are reported to have remarkable physical properties[5][6][7]. They are stronger than steel and as flexible as plastic, conduct both electrical and thermal energy better than almost any material ever discovered and can be made from simple raw materials such as methane gas[5][6][7].

These intriguing structures have sparked much excitement in recent years and a large amount of research has been dedicated to understanding their behaviour. Many potential applications have been proposed for carbon nanotubes. These include composites that are both conductive and high-strength in nature[8][9][10][11][12][13][14], nano-sized semiconductor devices[15][16], probes[17][18] and interconnects[19][20][21][22], energy storage[23] and energy conversion devices[24][25], sensors[26][27][28][29], field emission displays[30][31], radiation sources[32], hydrogen storage media[33][34][35][36][37] and drug delivery systems[38]. There is however a question as to whether the actual material can live up to the projections.

Characterizing and understanding the fundamental physical properties of carbon nanotubes is limited not only by the lack of purity of the specimen and difficulties with processibility, but also by the size distribution of the nanotubes and polydispersity of nanotube type in any given sample. The potential usefulness of these materials is hugely hindered by the lack of large scale, low cost robust selective synthesis techniques. Bulk availability of uniform materials is one of the major factors in extending their technological applications.

1.2 Historical Background

Iijima first discovered nanotubes while studying the material deposited on the cathode during the arc-evaporation synthesis of fullerenes[1]. It was found that the central core of the cathodic deposit contained a variety of closed graphitic structures including nanoparticles and nanotubes, of a type which had never previously been observed. A short time later[39], it was shown that nanotubes could be produced in bulk quantities by varying the arc-discharge evaporation conditions. This paved the way to an explosion of research into the physical and chemical properties of carbon nanotubes in laboratories all over the world. A major event in the development of carbon nanotubes was the synthesis in 1993 of single-walled nanotubes[40]. The standard arc-discharge method produces only multiwalled tubes. It was found that addition of metals such as cobalt to the graphite electrodes resulted in an extremely fine tube with a single-wall. An alternative method of preparing single-walled nanotubes was described in 1995[41]. Like the original method of preparing C_{60}, this involved the vaporisation of graphite but using lasers, and resulted in a high yield of single-walled tubes

with unusually uniform diameters. These highly uniform tubes had a greater tendency to form aligned bundles than those prepared using arc-evaporation. Initial analysis of the tubes produced by this method showed that the samples contained a very high proportion of nanotubes with a specific structure. However subsequent work showed that the samples were less homogeneous than originally thought. The HiPco process, high pressure CO disproportionation, has been shown to produce nanotubes of high purity, with current achievable purity levels as high as 90% atomic percent SWNT[42][43][44]. The yield and diameter size can be varied by controlling the process parameters.

1.3 Processing of Nanotubes

Carbon nanotubes are graphene sheets of sp^2-bonded carbon arranged in a cylindrical formation. A carbon nanotube is essentially a sheet of carbon atoms, arranged in hexagons, that curls up into a tube or cylinder. It has a length (up to several microns) to diameter (a few nanometers) ratio of about 1000[1] so nanotubes can be considered as nearly one dimensional structures. The ends of the cylinders, called the end cap, consist of a hemisphere of a fullerene. Carbon nanotubes come in two basic types, a single-walled nanotube, which is a single coil of carbon hexagons; and a multiwalled tube, in which a single tube is encased in a wider tube, which itself is inside other tubes, figure 1.1.

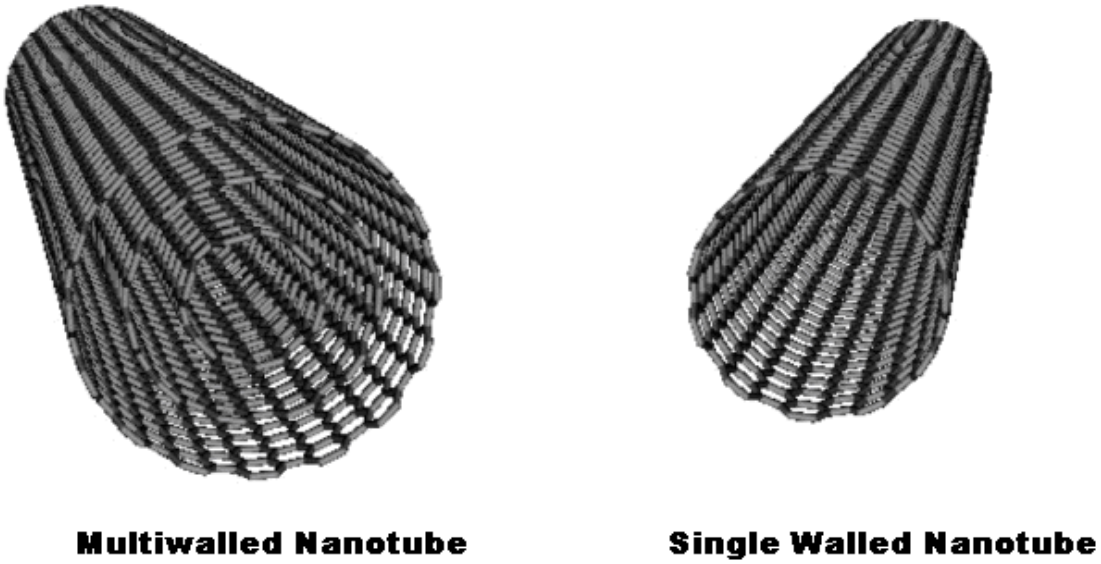

FIGURE 1.1: Diagrammatical representation of multiwalled and single walled nanotubes

The chemical reactivity of a nanotube, compared with graphene, is enhanced as a direct result of the curvature of the nanotube surface[45]. This reactivity is directly related to the π orbital mismatch caused by an increased curvature. Therefore a distinction must be made between the endcaps and the sidewalls when considering the potential behaviour of the tube. For the same reason a smaller tube diameter results in increased reactivity. Chemically carbon nanotubes are very stable and their properties are generally thought of as being between those of graphite, which has sp^2 atoms in a 2D plane and diamond, which has sp^3 atoms in a 3D space. The larger the diameter of tube the more planar and sp^2 in character are the carbon bonds. Depending on the extent to which the sp^2 bonds are strained into a third dimension, the bond character becomes more like sp^3. Therefore the study of nanotubes with different diameters is necessary to fully characterize and understand their properties.

The origin of the attractive forces between graphitic structures is well known. Due to the extended π electron system, these systems are highly polarizable, and so subject to large attractive van der Waals forces[46]. These forces are responsible for the secondary bonding that holds graphitic layers together. In the case of carbon nanotubes, these forces lead to so called “bundles” or “ropes”. Extended structures are formed by side-by-side aggregation of the nanotubes in ropes. Furthermore, these ropes tangle with one another. With high shear, these ropes can be untangled, but it is extremely difficult to further disperse them to produce single tubes.

As mentioned before, one of the main limitations in the large scale use of nanotubes arises from limitations in the processing of carbon nanotubes. This processing not only involves the removal of impurities and catalytic particles, the sorting of tubes into particular diameter and tube types but also the production of single tubes rather than the aggregated or bundled state. Whereas a lot of work has been carried out on the purification aspect of this problem there still remains difficulty in the isolation of single tubes of particular size and type. Nanotubes have been dispersed by acids[47][48], macromolecules[49][50][51][52][53][54], surfactants[55][56] as well as through functionalisation techniques[57]. However any debundling has only been demonstrated at low concentrations. More importantly these techniques either leave the tubes damaged[47][48] or the dispersion agent remains attached to the tubes after the debundling process[47,50,51,52,53,54,55,56,57]. It therefore would be of great advantage to find a solvent that can successfully debundle the nanotubes at high concentrations. A number of studies on the use of organic solvents in

this respect have been reported in literature[58][59][60][61][62][63][64]. N,N-dimethylformamide (DMF)[58], N-methyl-2-pyrrolidone (NMP)[59] and 1,2, dichloroethane (DCE)[60] have been demonstrated to solubilise to some extent. The consensus of these studies seems to be that the criteria for successful solvents are high electron pair donicity, low hydrogen bond donation parameter and a high solvatochromic parameter.

It is clear that understanding the fundamental properties of nanotubes is necessary to get a realisation of the full potential of these materials. Processing and purification on a mass scale will need to be carried out if these materials are to have large scale industrial applications and move beyond the laboratory bench. Highly sensitive, capital intensive equipment such as TEM and AFM, have been used to identify the state and morphology of tube samples as well as their levels of purity, however for large scale industrial applications there is a need for routine, high throughput, cost effective methods to give the same kind of detail.

In this thesis organic solvents are used to debundle single walled nanotubes. The debundling is confirmed and the degree measured using absorption spectroscopy and the highly capital and low through put techniques of TEM and AFM. Although Raman spectroscopy is a well established technique for characterising tube bundles and single tubes little is know about what subtle changes occurs in the Raman spectrum as one goes from a highly bundled state to a lower degree of bundling. In this thesis these changes are examined and the use of previously unidentified spectral markers to the degree of

debundling are identified. Finally, using Raman spectroscopy, a temperature dependent study was carried out. The study demonstrates the importance of sample processing for determining the true fundamental parameters of the material.

1.4 Thesis Outline

Chapter 2 examines the structure and physical properties of single walled carbon nanotubes. It also looks at the various production techniques. Chapter 3 looks at the various spectroscopic techniques employed in the thesis and discussed their particular application to carbon nanotubes. Two different types of single walled nanotubes were used in this study; a sample of HiPco tubes and a sample of arc discharge tubes. In Chapter 4 the Raman spectra of the two as produced tube samples are examined and characterised. In chapter 5 a study of the relative effectiveness of three different organic solvents to debundle the tubes is described. A novel use of absorption spectroscopy is used to determine the relative bundle size and this is confirmed using TEM and AFM. In chapter 6 Raman spectroscopy is carried out on these debundled tubes and spectral markers identified which can be used to determine relative bundle size. Chapter 7 describes a temperature dependent Raman study carried out on the bundled and debundle tubes. Differences in the Raman behaviour between the bundled and debundled samples are described. Chapter 8 summarizes the work.

1.5 References

[1] S.Iijima, Nature **354** , 56 (1991)

[2] L.V.Radushkevich, V.M.Lukyanovich Zurn Fisic Chim **26,** 88-95 (1952)

[3] M.Inman National Geographic November 16 (2006)

[4] M.Reibold, P.Paufler, A.A.Levin, W.Kochmann, N.Pätzke, D.C.Mayer Nature **444,** 286 (2006)

[5] M.Yu, O.Lourie, M.J.Dyer, T.F.Kelly, R.S.Ruoff, Science, **297**, 787 (2000)

[6] B.Q.Wei, R.Vajtai, P.M.Ajayan, App. Phys. Lett. **79**, 1172 (2001)

[7] P.Kim, L.Shi, A.Majumdar, P.L.McEuen, Phys. Rev. Lett. 8721 (2001)

[8] E.T.Thostenson, Z. F. Ren, T. W. Chou, Compos. Sci. Technol. **61**, 1899 (2001)

[9] K. T. Lau, D. Hui, Composites Part B, Engineering **33**, 263 (2002)

[10] M. Cochet, W. K. Maser, A. M. Benito, M. A. Callejas, M. T. Martı´nez, J.M. Benoit, J. Schreiber, O. Chauvet, Chem. Commun. 1450 (2001)

[11] V. Jamieson: New Scientist, **30, (** 2003)

[12] H. Zengin, W. S. Zhou, J. Y. Jin, W. R. Czerw, D. W. Smith, L. Echegoyen, D. L. Carroll, S. H. Foulger, J. Ballato, Adv. Mater. **14**, 480(2002)

[13] J. Deng, X. Ding, W. Zhang, Y. Peng, J. Wang, X. Long, P. Li, A. S. C. Chan, Eur. Polym. J., **38**, 2497 (2002)

[14] G. B. Blanchet, C. R. Fincher, F. Gao, Appl. Phys. Lett. **82**, 1290 (2003)

[15] Z. Yao, C. Dekker, Ph. Avouris, Top. Appl. Phys. **80**, 147 (2001)

[16] S. J.Tans, A.R.M. Verschueren, C.Dekker, Nature **393**, 49 (1998).

[17] W. A. de Heer, A. Châtelain, D. Ugarte, Science **270**, 1179 (1995)

[18] A. G. Rinzler, J.H.Hafner, P.Nikolaev, P.Nordlander, D.T.Colbert, R.E.Smalley, L.Lou, S.G.Kim, D.Tománek, Science **269**, 1550 (1995)

[19] J. Li, Q. Ye, A. Cassell, H.T. Ng, R. Stevens, J. Han, M. Meyyappan, Appl. Phys. Lett., **82**, 2491 (2003)

[20] M. Nihei, M. Horibe, A. Kawabata, Y. Awano, Japan. J. Appl. Phys, **43**, No. 4B, 1856 (2004)

[21] A.P. Graham, G.S. Duesberg, R. Seidel, M. Liebau, E. Unger, F. Kreupl, W. Hoenlein, Diamond and Related Materials, **13**, 1296 (2004)

[22] M. Liebau, A. P. Graham, Z. Gabric, R. Seidel, E. Unger, G. S. Duesberg, F. Kreupl, AIP Conference Proceedings **723,** 536 (2004)

[23] V.L. Pushparaj, M. M. Shaijumon, A.Kumar, S. Murugesan, L. Ci, R. Vajtai, R.J. Linhardt, O.Nalamasu, P. M. Ajayan, PNAS **104,** 34 (2007)

[24] P. V. Kamat, The Electrochemical Society Interface Spring (2006)

[25] T. Umeyama, H. Imahori, Energy Environ. Sci. **1**, 120 (2008)

[26] P. G. Collins, K. Bradley, M. Ishigami, A. Zettl, Science **287**, 1801 (2000)

[27] J. H. Hafner, C. L. Cheung, C. M. Leiber, Nature **398**, 761 (1999)

[28] J. Kong, N.R.Franklin, C.Zhou, M.G.Chapline, S.Peng, K.Cho, H.Dai, Science **287**, 622 (2000)

[29] H. Dai, J. H. Hafner, A. G. Rinzler, D. T. Colbert, R. E. Smalley, Nature **384**, 147 (1996)

[30] N. S. Lee, D.S.Chung, I.T.Han, J.H.Kang, Y.S.choi, H.Y.Kim, S.H.Park, Y.W.Jin, W.K.Yi, M.J.Yun, J.E.Jung, C.J.Lee, J.H.You, S.H.Jo, C.G.Lee, J.M.Kim, Diamond Related Materials **10**, 265 (2001)

[31] L.Yukui, Z.Changchun, L.Xinghui, Diamond Related Materials **11**, 1845 (2002)

[32] H. Sugie, M.Tanemura, V.Filip, K.Iwata, K. Takahashi, F.Okuyama, Appl. Phys. Lett. **78**, 2578 (2001)

[33] M. S. Dresselhaus, K. A. Williams, P. C. Eklund, Mater.Res. Soc. Bull. **24**, 45 (2000)

[34] G. G. Tibbetts, G. P. Meisner, C. H. Olk, Carbon **39**, 2291 (2001)

[35] F.von Zeppelin, H.Reule, M. Hirscher, J. Alloys Compounds **330–332**, 654 (2002)

[36] C. Zandonella, Nature **410**, 734 (2001)

[37] Y. Ye, C. C.Ahn, C.Witham, B.Fultz, J.Liu, A.G.Rinzler, D.Colbert, K.A.Smith, R.E.Smalley, Appl. Phys. Lett. **74**, 2307 (1999)

[38] A. Bianco, K. Kostarelos, M. Prato, Current Opinion in Chemical Biology **9** 674-679 (2005)

[39] T.W.Ebbesen, P.M.Ajayan, Nature, **358**, 220 (1992)

[40] S.Iijima, T.Ichihashi, Nature, **363**, 603 (1993)

[41] T.Guo, P.Nikolaev, A.Thess, D.T.Colbert R.E.Smalley Chem. Phys. Lett, **243,** 49(1995)

[42] H.J.Dai, A.G.Rinzler, P.Nikolaev, A.Thess, D.T.Colbert, R.E.Smalley Chem. Phys. Lett, **260,** 471(1996)

[43] I.W.Chiang, B.E.Brinson, A.Y.Huang, P.A.Willis, M.J.Bronikowski, R.E.Smalley, J.L.Margrave, R.H.Hauge, J. Phys. B **105**, 8297-8301 (2001)

[44] P.Nikolaev, M.Bronikowski, R.K.Bradley, F.Rohmund, D.Colbert, K.A.Smith, R.E.Smalley: Chem. Phys. Lett. **313**, 91-97 (1999)

[45] S.Niyogi, M.A.Hamon, H.Hu, B.Zhao, P.Bhowmik, R.Sen, M.E.Itkis, R.C.Haddon, Accounts of Chemical Research, **35**, 12, (2002)

[46] T.Yumura, K.Yoshizawa, Chem.Phys **279**, 111 (2002)

[47] S.Ramesh, L.M.Ericson, V.A.Davis, R.K.Saini, C.Kittrell, M.Pasquali, W.E.Billups, W.W.Adams, R.H.Hauge, R.E.Smalley, J. Phys.Chem. B **108,** 8794 (2004)

[48] V.A.Davis, L.M.Ericson, A.N.G.Parra-Vasquez, H.Fan, Y.H.Wang, V.Prieto, J.A.Longoria, S.Ramesh, R.K.Saini, C.Kittrell, W.E.Billups, W.W.Adams, R.H.Hauge, R.E.Smalley, M. Pasquali, Macromolecules **37,** 154 (2004)

[49] J.N.Coleman, A.Fleming, S.Maier, S.O Flaherty, A.I.Minnett, M.S.Ferrerira, S.Hutzler, W.J.Blau, J Phys. Chem B **108,** 3446 (2004)

[50] A.B.Dalton, C.Stephan, J.N.Coleman, B.McCarthy, P.M.Ajayan, S.Lefrant, P.Bernier, W.J.Blau, H.J.Byrne, J Phys. Chem B **104,** 10012 (2000)

[51] B.McCarthy, J.N.Coleman, S.A.Curren, A.B.Dalton, A.P.Davey, Z.Konya, A.Fonseca, J.B.Naby, W.J.Blau, J Mater.Sci.Lett. **19,** 2239 (2000)

[52] E.Gregan, S.M.Keogh, A.Maguire, T.K.Hedderman, L.O Neil, G.Chambers, H.J.Byrne Carbon **42,** 1031 (2004)

[53] S.M.Keogh, T.K.Hedderman, E.Gregan, G.Farrell, G.Chambers, H.J.Byrne J.Phys.Chem **108,** 6233-6241 (2004)

[54] T.K.Hedderman, S.M.Keogh, G.Chambers, H.J.Byrne J.Phys.Chem.**110,** 3895 (2006)

[55] G.S.Duesberg, M.Burghard, J.Muster, G.Philipp, S.Roth Chem. Commun. **435,** (1998)

[56] M.J.O Connell, S.M.Bachilo, C.B.Huffman, V.C.Moore, M.S.Strano, E.H.Haroz, K.L.Rialon, P.J.Boul, W.H.Noon, C.Kittrell, R.H.Hauge, R.B.Weisman, R.E.Smalley Science **297,** 593 (2002)

[57] R.Blake, Y.K.Gun'ko, J.N.Coleman, M.Cadek, A.Fonsecca, J.B.Nagy, W.J.Blau, J.Am.Chem.Soc.**126,** 10226 (2004)

[58] J.L.Bahr, E.T.Mickelson, M.J.Bronikowski, R.E.Smalley, J.M.Tour, Chem. Com. 193-194 (2001)

[59] K.D.Ausman, R.Piner, O.Lourie, R.S.Ruoff J.Phys. Chem **104,** 38 (2000)

[60] K.K.Kim, D.J.Bae, C.M.Yang, K.H.An, J.Y.Lee, Y.H.Lee, Nanoscience and Nanotechnology **5,** 1055-1059 (2005)

[61] J.Liu, M.J.Casavant, M.Cox, D.A.Walters, P.Boul, W.Lu, A.J.Rimberg, K.A.Smith, D.T.Colbert, R.E.Smalley, Chem. Phys.Lett. **303,** 125 (1999)

[62] C.A.Furtado, U.J.Kim, H.R.Gutierrez, L.Pan, E.Dickey, P.C.Eklund, J.Am.Chem.Soc **126,** 6095 (2004)

[63] B.J.Landi, H.J.Ruf, J.J.Worman, R.P.Raffaelle J.Phys.Chem B **108,** 17089 (2004)

[64] S.Giordani, S.D.Bergin, V.Nicolosi, S.Lebedkin, M.M.Kappes, W.J.Blau, J.N.Coleman, J.Phys.Chem B **110,** 15708-15718 (2006)

CHAPTER 2

CARBON NANOTUBES

2.1 Introduction

As discussed in chapter 1, although carbon nanotubes show great promise for a range of technological applications, their use is complicated by the variation in structure that exists from tube to tube which leads to a variation in the measured physical properties. This is compounded by the fact that different production techniques give rise to batches of tubes with different structural content and varying levels of purity. This chapter examines the structure of single walled carbon nanotubes, their proposed physical properties and the various techniques used to produce them.

2.2 Structure

Carbon nanotubes are graphene sheets of sp^2-bonded carbon arranged in a cylindrical formation[1]. Single Walled Nanotubes are classified into two primary groups *chiral* and *achiral*, as shown in figure 2.1.

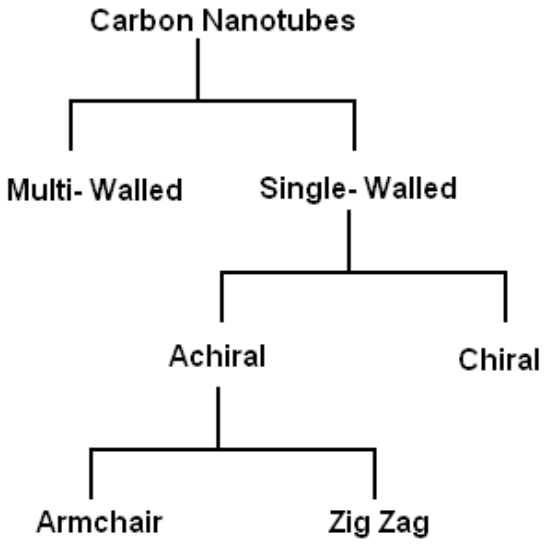

FIGURE 2.1: Chart Showing Various Kinds of Carbon Nanotubes

A nanotube is achiral if the mirror image of the nanotube has an identical structure to the original one. There are two types of achiral nanotubes; *armchair* and *zigzag.* These are formed by bisecting a C_{60} molecule at the equator and joining the two resulting hemispheres with a cylindrical tube one monolayer thick and with the same diameter as the C_{60}. If the C_{60} molecule is bisected normal to a five-fold axis of symmetry (i.e. through the equatorial hexagons), an *armchair* nanotube is formed, as shown in figure 2.2 (a).

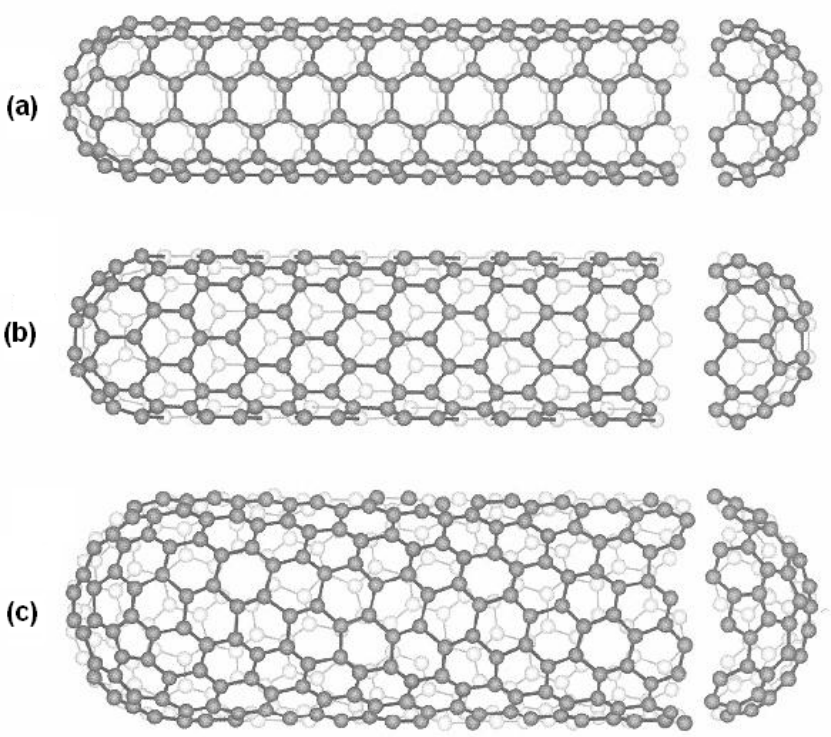

FIGURE 2.2: Classification of Single Walled Carbon Nanotube (a) armchair (b) zig zag and (c) chiral nanotube[1]

If the C_{60} molecule is bisected normal to a threefold axis (i.e. through the equatorial pentagons, a *zigzag* nanotube is formed, as shown in figure 2.2(b). The mirror image of a chiral nanotube (shown in figure 2.2(c)) image cannot be superimposed onto the original. The structure of a single walled nanotube can be described by the chiral vector $\mathbf{C_h}$, which corresponds to a section of the nanotube perpendicular to the nanotube axis, see figure 2.3.

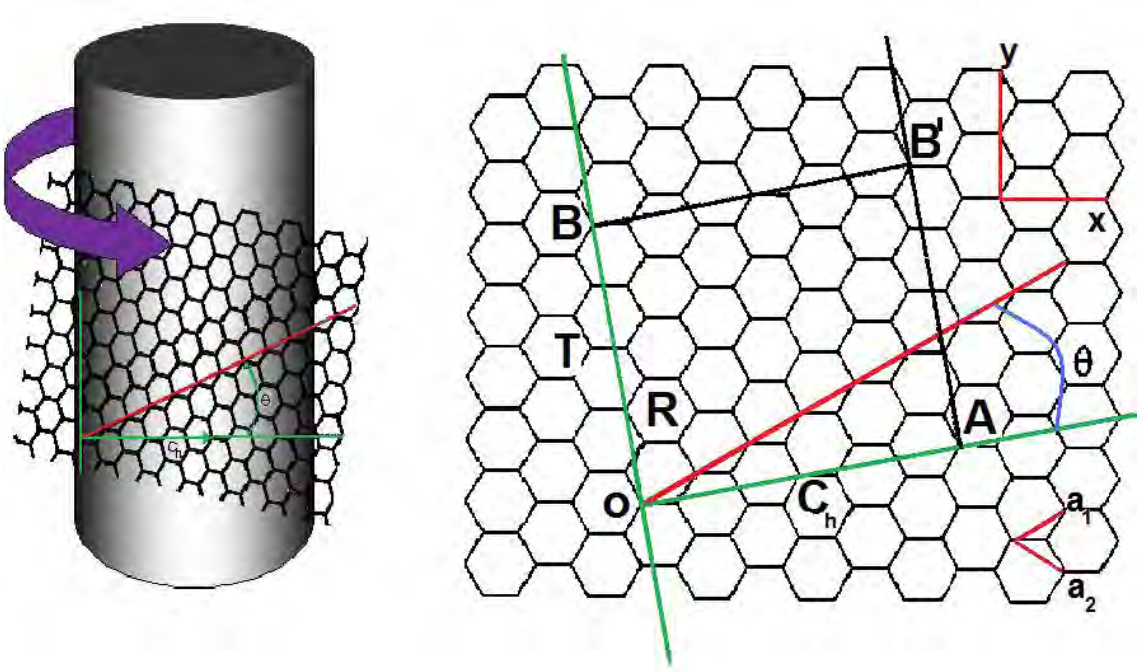

FIGURE 2.3: Unrolled Lattice of a Nanotube[adapted from [1]]

The chiral vector is defined by [1]

$$\mathbf{C}_h = n\mathbf{a}_1 + m\mathbf{a}_2 \qquad 2.1$$

where **n** and **m** are integers. An ensemble of possible chiral vectors can be specified by equation 2.1 in terms of pairs of integers **(n,m)** and this ensemble is shown in figure 2.4. The values of **n** and **m** determine the chirality, or "twist" of the nanotube. The chirality in turn affects the conductance of the nanotube, its density, its lattice structure, and other properties. The chiral vector makes an angle θ, called the chiral angle, with the a_1 (zig zag) direction[1]. The chiral angle for zig zag tubes is $\theta = 0^o$, for armchair tubes $\theta = 30^0$ and for all chiral tubes $0^o < \theta < 30^o$. Each pair of integers (*n*,*m*) defines a different way of rolling the graphene sheet to form a carbon nanotube.

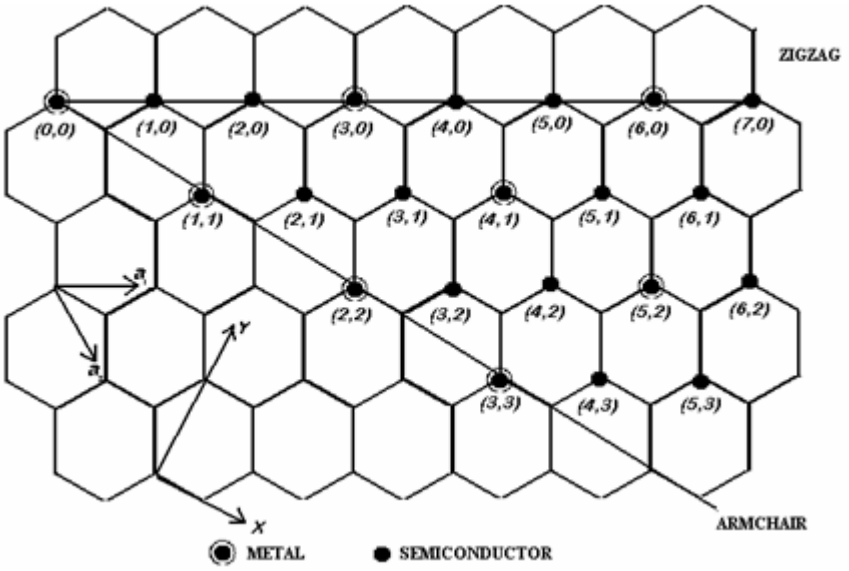

Figure 2.4: Graphene layer with atoms labelled using (n,m) notation. Unit vectors of the 2D lattice[2]

Given the chiral vector (n,m), the diameter of a carbon nanotube d_t can be determined using the relationship

$$d_t = \sqrt{3}a_{c-c}(n^2 + m^2 + nm)^{1/2} / \pi \qquad 2.2$$

where a_{c-c} is the nearest-neighbour C-C distance (1.421Å in graphite)[3]. The chiral angle therefore is given by

$$\theta = \tan^{-1}\left[\frac{\sqrt{3}m}{(m+2n)}\right] \qquad 2.3$$

A single walled nanotube is considered metallic if the value **n - m** is divisible by three[1]. Otherwise, the nanotube is semiconducting[1]. So, when tubes are formed with random values of **n** and **m**, it would be expected that two-thirds of nanotubes would be semi-conducting, while the other third would be metallic. Experimental results have shown that in fact this is the case[3][4].

For all metallic nanotubes, independent of their diameter and chirality, the density of states per unit length, $N(E_f)$ along the nanotube axis is a constant given by[1]

$$N(E_f) = \frac{8}{\sqrt{3}\pi a|t|} \qquad 2.4$$

where a is the lattice constant and **|t|** is the nearest neighbour carbon to carbon tight binding overlap energy usually denoted by γ_0 in graphite literature[5]. The density of states for the nanotubes at the Fermi energy $\mathbf{E}_f$ located at **E** =0, is zero for semi-conducting nanotubes, and is non-zero for metallic tubes. The Fermi velocity, v_f , is given by[1]

$$v_f = \frac{3|t|a_{c-c}}{2\hbar} \qquad 2.5$$

The energy gap $\mathbf{E}_g$ for semi-conducting nanotubes depends on the reciprocal of the nanotube diameter $\mathbf{d}_t$, which is independent of the chirality angle, and is given by[3]

$$E_g = \frac{|t|a_{C-C}}{d_t} \qquad 2.6$$

$a_{\mathbf{C\text{-}C}} = a/\sqrt{3}$ is the nearest neighbour C-C distance on the graphene sheet.

The average C-C bond length of 1.42 Å was measured by Spires and Brown[7] and later confirmed by Wildöer in 1998 using Scanning Tunneling Spectroscopy (STS)[3]. The C-C tight bonding overlap energy is of the order of 2.7 eV. Wildöer[3] estimated it to be between 2.6 eV - 2.9 eV while at the same time, Odom[8] estimated it to be 2.45 eV. Currently, the physical properties of SWNT are still being explored and disputed. What makes it so difficult is that nanotubes have a very broad range of electronic, thermal and structural

properties that change depending on the different kinds of nanotube (defined by diameter, length and chirality or twist) and this broad range potentially exists within any one as produced sample. Nanotubes vary in size, depending on how they are produced (see section 2.4) and they are not always perfectly cylindrical. The larger nanotubes, such as a (20, 20) tube, tend to bend under their own weight[6].

Another problem arises from the fact that nanotubes aggregate in bundles as a result of substantial van der Waals attractions between tubes. It has been observed that increased purity in a sample is associated with increased bundle size[9]. It is thought that this is a result of the fact that there are fewer small particles present to interfere with the van der Waals attraction between neighbouring tubes. It was found that the individual SWNTs pack into a close-packed triangular lattice with a lattice constant of about 17 Å[10]. In addition it was concluded that the density, lattice parameter, and interlayer spacing of the bundles was dependent on the chirality of the tubes in the mat[11]. The space between the tubes and therefore the binding energy of the bundles is also dependent on chirality and the diameter of the tubes in the aggregate[11]. It has been calculated that armchair tubes have a spacing of 3.38 Å, zigzag tubes have a spacing of 3.41 Å, and (2m, n) chiral tubes have an interlayer spacing value of 3.39 Å[11]. As a good estimate the lattice parameter in carbon nanotube bundles can therefore be taken as d+ 0.34nm where d is the tube diameter. On a macroscopic scale it has been observed that the bundles or "ropes" of carbon nanotubes mat together[10].

2.3 Electronic and Optical Properties

Graphene is a single atomic sheet of graphitic carbon atoms that are arranged into a honeycomb lattice. There are two carbon atoms in one unit cell where each carbon atom sits in two interpenetrated triangular lattices with inversion symmetry between them. This unique topology of the hexagonal arrangement of carbon atoms renders an unusual energy dispersion relation at the Fermi energy in graphene. In the energy band structure of graphene, figure 2.5, the valence band (lower band) and conduction band (upper band) touch at six Brillouin zone corners where the Fermi level is located.

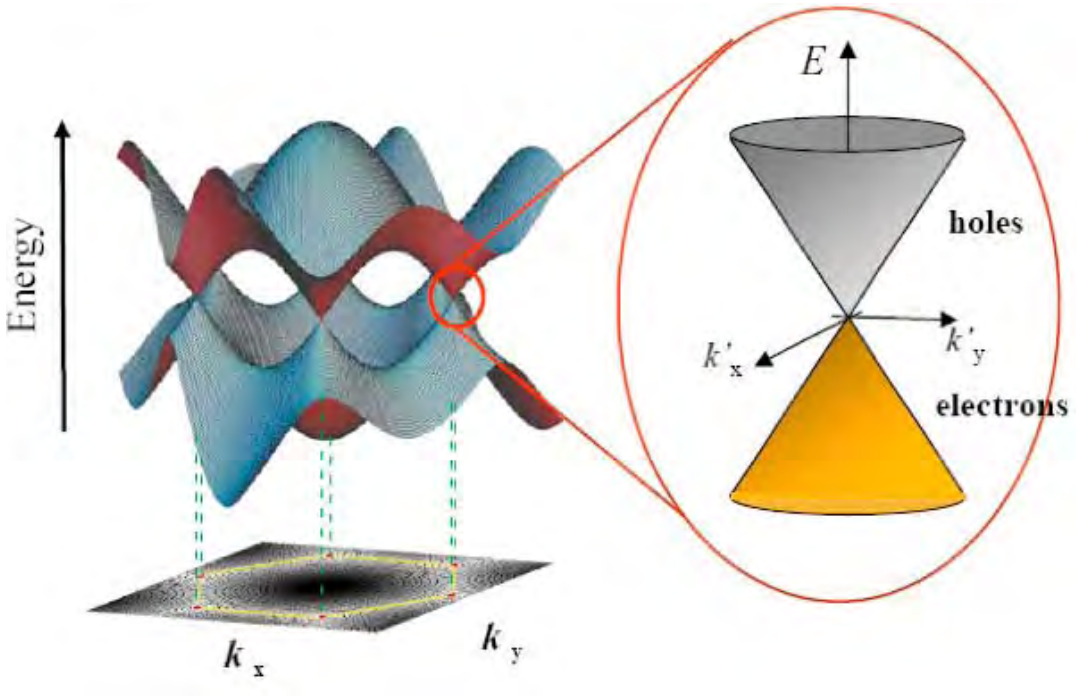

Figure 2.5: Energy band structure of graphene[12]

In the vicinity of these points, the energy dispersion relation is linear and thus the electrons always move at a constant speed, the Fermi velocity, v_F. This is also the case in carbon nanotubes[13].

The quantised electronic states of nanostructures, such as single wall nanotubes, determine their electronic and optical properties and they influence their physical and chemical properties. To describe these states, consider a nanoscale solid in the geometry of a wire. It is nanoscale along the **x** and **y** dimensions but it is continuous in the **z**. The energies and eigen-states of such a wire are given by[14]

$$E = E_{ij} + \frac{\hbar^2 k^2}{2m}; \quad \psi(x,y,z) = \psi_{ij}(x,y)e^{ikx} \qquad 2.7$$

where **i** and **j** are the quantum numbers labelling the eigenstates in the **x**,**y** plane and **k** is the wavevector in the **z** direction. The dispersion relationship consists of a series of 1D sub-bands, each corresponding to a different transverse energy state E_{ij}. The total density of electronic states N(E) is the sum of the density of states of the individual sub-bands:

$$N(E) = \sum_{ij} N_{ij}(E) \qquad 2.8$$

where $N_{ij}(E)$ is given by

$$N_{ij}(E) = \frac{dN_{ij}}{dk}\frac{dk}{dE} = (2)(2)\frac{L}{2\pi}\left[\frac{m}{2\hbar^2(E-E_{ij})}\right]^{\frac{1}{2}} = \frac{4L}{h v_{ij}} \quad \text{for } \mathbf{E>E_{ij}} \qquad 2.9$$

$$=0 \qquad \text{for } \mathbf{E<E_{ij}} \qquad 2.10$$

Here v_{ij} is the velocity of the electron in the i,j sub-band with kinetic energy $\mathbf{E-E_{ij}}$. From equation 2.9 it can be seen that the density of states diverges as $(\mathbf{E-E_{ij}})^{-1/2}$ at each sub-band threshold. These divergences are called van Hove singularities. This behaviour is in contrast to the 3D case where N(E) goes to

zero at low energies and the 2D case where N(E) steps up a constant value at the bottom of each 2D sub-band[14].

The van Hove singularities affect the electrical and optical properties including absorption and emission of 1D systems such as nanotubes. Figure 2.6 shows, as examples, the density of states function for two single wall nanotubes, one metallic the other semiconducting.

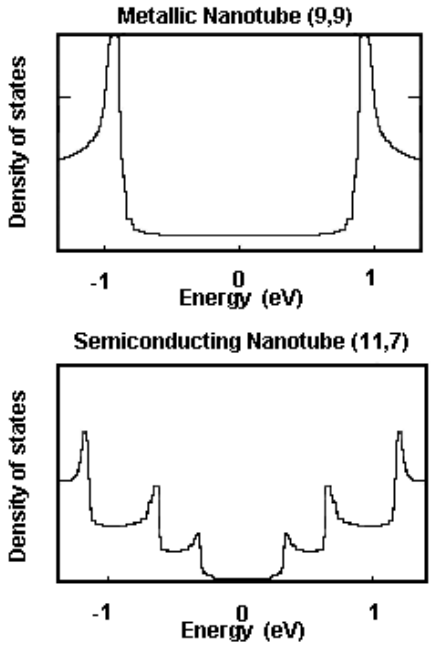

Figure 2.6: Density of States diagram, showing Van Hove singularities for a metallic and semi-conducting tube[15]

As mentioned before, at the Fermi energy (the highest occupied energy level), the density of states is finite for a metallic tube (though very small), and zero for semi-conducting tubes. It can also be seen that as the energy is increased, sharp peaks in the density of states, i.e. van Hove singularities, appear at specified energy levels. Despite the fact that single walled carbon nanotubes have a large number of van Hove singularities due to quantum confinement effects, only a small number of electronic levels can be accessed through

electromagnetic interaction associated with incident light due to symmetry selection rules. Because of these symmetry considerations optical transitions normally occur between symmetrical pairs of van Hove peaks in the valence band and the conduction band due to excitonic and other many body effects[14]. These transitions are labelled E_{11}, E_{22}, E_{33} etc. Generally denoted as E_{ii}, each single walled carbon nanotube has a unique set of E_{ii} values. The actual excited states are excitonic in nature because the excited electron is bound to the hole that is left behind in the excitation process, giving rise to a bound electron-hole pair or an exciton. The excited state energies are further perturbed by electron-electron repulsion effects, and it is the combination of these attractive and repulsive interactions that determine the optical transitions energies that are observed experimentally and calculated theoretically. These interactions are strongly enhanced in 1-D systems since the electrons and holes are highly confined in 1-D space.

The optical excitation energies between the van Hove singularities for a metallic and semi-conducting tube are given by equations of the type[16]

$$E_{11}^{M}(d_t) = \frac{6a_{c-c}\gamma_0}{d_t}$$
$$E_{11}^{S}(d_t) = \frac{2a_{c-c}\gamma_0}{d_t} \qquad 2.11$$
$$E_{22}^{S}(d_t) = \frac{4a_{c-c}\gamma_0}{d_t}$$

where $a_{c\text{-}c}$ is carbon-carbon bond distance and γ_0 is the interaction energy between neighbouring carbon atoms. The absorption of incident light is enhanced when the photon energy matches the transition energy. In figure 2.7 it can be seen that this will occur when $\mathbf{h\nu = c_2\text{-}v_2}$, the energy difference between

the 2nd Van Hove singularities in the conduction and valence bands. Once excited, the electrons and holes relax quickly to the bottom of the first sub-band, where they recombine, either non-radiatively or in semiconducting tubes radiatively producing luminescence with energy **E= c_1-v_1** see figure 2.7[14]. Excitation with energy equal to the transition energy between these van Hove singularities, is the basis not only of absorption spectroscopy of single walled nanotubes (section 3.3) but also the resonant enhancement of Raman scattering by single walled nanotubes (section 3.2). When dealing with polydisperse samples, multiple peaks appear in the energy spectrum corresponding to contributions from the many nanotubes of varying diameters and chiralities present in the samples. In addition tube – tube interactions shift the values of these peaks giving a complex energy spectrum from which information about individual tubes is hard to find.

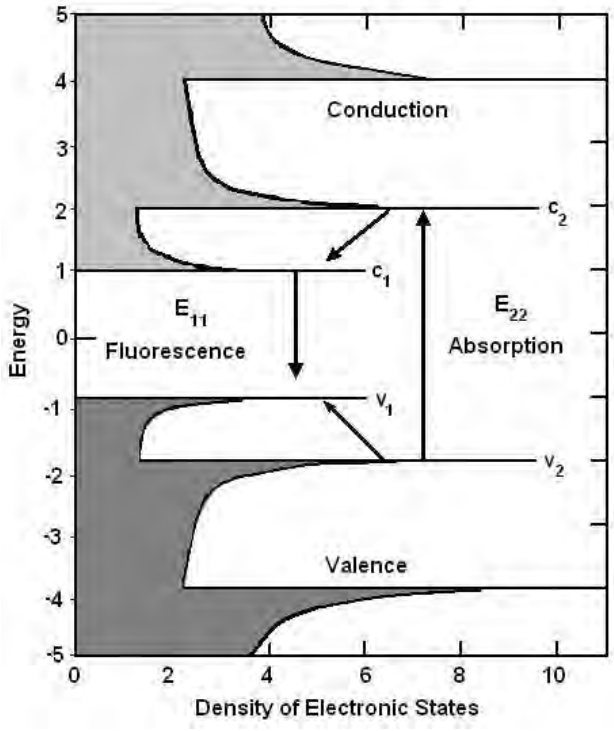

FIGURE 2.7: The Density of States for a Semiconducting Carbon Nanotube as a Function of Energy[14]

2.4 Single Wall Nanotube Synthesis

Single wall carbon nanotubes are generally produced by three main techniques, arc discharge[18][19][20], laser ablation[21] and HiPco[22] (gas-phase decomposition of carbon monoxide) although other techniques exist. In the arc discharge technique, a vapour is created by an arc discharge between two carbon electrodes with or without catalyst. Nanotubes self-assemble from the resulting carbon vapour. In the laser ablation technique, a high-power laser beam impinges on a volume of carbon containing feedstock gas (methane or carbon monoxide). In the HiPco process, catalysts for SWNT growth form in situ by thermal decomposition of iron pentacarbonyl in a heated flow of carbon monoxide. In the current state of the art, the laser ablation and HiPco techniques produce a small amount of clean nanotubes, whereas arc discharge methods generally produce large quantities of impure material[2].

The actual growth mechanism by which nanotubes are formed is not clearly understood. In fact there may actually be more than one mechanism operative during the formation of carbon nanotubes. One of the mechanisms being discussed consists of three steps[23]. First C_2, a precursor to the formation of nanotubes and fullerenes, is formed on the surface of metal catalyst particles. From this metastable carbide particle, a rodlike carbon structure quickly forms. Then there is a slow graphitization of its wall. This mechanism is proposed based on in-situ TEM observations[24]. The actual growth of the nanotube seems to be the same for all techniques. The exact atmospheric conditions required are dependent on the technique being used. There are several theories as to how the growth of nanotubes actually proceeds. One theory[25] suggests that the

metal catalyst particles, which it presumes are spherical or pear-shaped in structure, are floating or are supported on graphite or another substrate. The deposition of the carbon initially takes place on only one half of the surface. It diffuses along the concentration gradient and precipitates on the opposite half, around and below the bisecting diameter. However, it does not precipitate from the apex of the hemisphere. This accounts for the hollow core that is characteristic of these tubes. For supported metals, filaments can form either by 'extrusion' in which the nanotube grows upwards from the metal particles that remain attached to the substrate, or the particles detach and move at the head of the growing nanotube. This later process is called 'tip-growth'. The size of the metal particle determines whether SWNT or MWNT are grown.

2.3.1 Arc Discharge Method

The most common and perhaps easiest way to produce carbon nanotubes is the arc discharge method. Back in the early 1990's this was the normal method used to produce C_{60} fullerenes, and it was as a by-product of this procedure that carbon nanotubes were discovered by Iijima[18]. The nanotubes are created through arc-vaporisation of two carbon rods placed end to end, separated by approximately 1mm, in an enclosure that is usually filled with inert gas (helium, argon) at low pressure (between 50 and 700 mbar). Some recent investigations have shown that it is also possible to create nanotubes with the arc method in liquid nitrogen[26]. A direct current of 50 to 100 A driven by approximately 20 V creates a high temperature discharge between the two electrodes. This discharge vaporises one of the carbon rods and forms a small rod shaped deposit on the other rod. Producing a high yield of nanotubes depends on the uniformity of the plasma arc and the temperature of the deposit formed on the

carbon electrode[19]. Depending on the exact technique, it is possible to selectively grow SWNTs or MWNTs. A typical experimental setup is shown in figure 2.8.

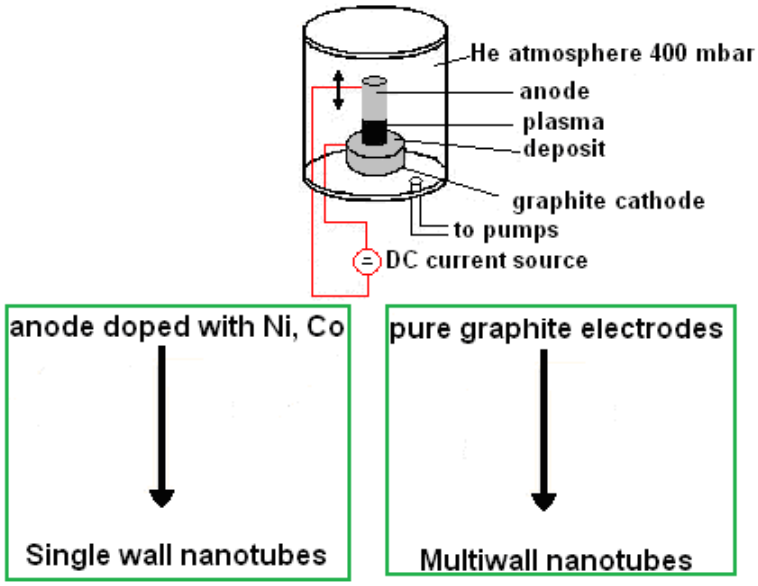

Figure 2.8: Experimental set-up of an arc discharge apparatus

To grow SWNT the anode is doped with metal catalysts, such as Fe, Mo, Ni, Co or Y. A lot of elements and mixtures of elements have been tested by various authors[27] and although there is a lot of variation in the results the quality and quantity of the nanotubes obtained depend on various parameters such as the current and system geometry, the metal concentration, inert gas pressure and the kind of gas used. The diameter of tubes produced using this method are in the range of 1.2 to 1.4 nm[2][28].

One of the main advantages of this technique is that the diameter of the tubes produced can be controlled somewhat by changing the thermal transfer, diffusion, and hence condensation of atomic carbon and metals between the

plasma and the vicinity of the cathode, by varying the plasma by changing the anode to cathode distance[29] or by using different metal catalysts[30].

In summary arc discharge methods can produce SWNT of diameter 0.8-1.4 nm with yields 30-90%. Tubes tend to be short with random sizes and the samples need a lot of purification. Tubes of this type are commercially available, for example Sigma Aldrich produces tubes commercially with typical purity levels of 70% and better[31].

2.3.2 Laser Ablation

In 1995, Smalley's group [21] at Rice University reported the synthesis of carbon nanotubes by laser vaporisation. A schematic of the laser vaporisation apparatus used by Smalley's group is shown in figure 2.9. A pulsed[32][33] or continuous [34][35] laser is used to vaporise a graphite target in an oven at 1200 °C. The main difference between the continuous and pulsed laser techniques is that the pulsed laser demands a much higher light intensity (100 kW/cm^2 compared with 12 kW/cm^2). The oven is filled with He or Ar gas in order to keep the pressure at 500 Torr. A very hot vapour plume forms, then expands and cools rapidly. As the vaporised species cool, small carbon molecules and atoms quickly condense to form larger clusters, possibly including fullerenes. The catalysts also begin to condense, but more slowly at first, and attach to carbon clusters and prevent their closing into cage structures [36]. Catalysts may even open cage structures when they attach to them. From these initial clusters, tubular molecules grow into single-wall carbon nanotubes until the catalyst particles become too large, or until conditions have cooled sufficiently that carbon no longer can diffuse through or over the surface of the catalyst particles.

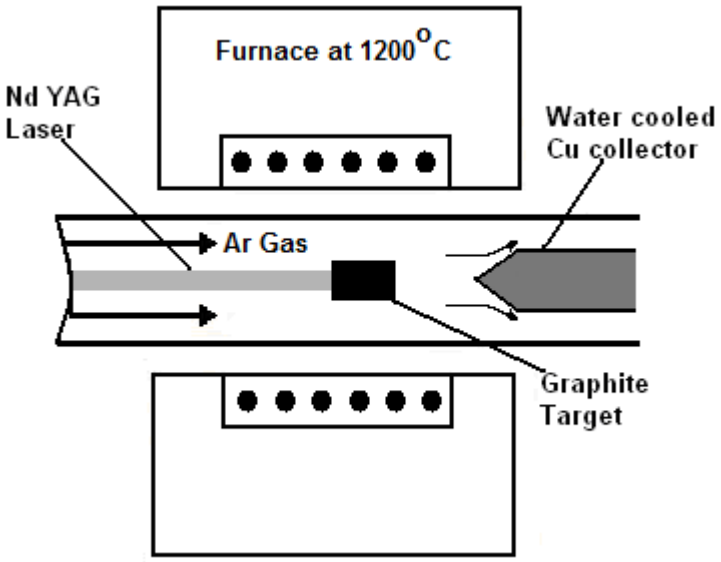

Figure 2.9: Schematic drawing of a laser ablation apparatus[35]

It is also possible that the particles become so much coated with a carbon layer that they cannot absorb more and the nanotube stops growing. The SWNTs formed in this case are bundled together by van der Waals forces [36].

The condensates obtained by laser ablation contain both carbon nanotubes and carbon nanoparticles. Laser vaporisation results in a higher yield for SWNT synthesis and the nanotubes have better properties and a narrower size distribution than SWNTs produced by arc-discharge. Nanotubes produced by laser ablation are purer (up to about 90 % purity) than those produced in the arc discharge process. A Ni/Y mixture catalyst gives the best yield. The size of the SWNTs ranges from 1-2 nm. For example the Ni/Co catalyst with a pulsed laser at 1470 °C gives SWNTs with a diameter of 1.3-1.4 nm[32]. In the case of a continuous laser at 1200 °C and Ni/Y catalyst (Ni/Y is 2:0.5), SWNTs with an average diameter of 1.4 nm were formed with 20 - 30 % yield.

Because of the quality of nanotubes produced by this method, scientists are trying to scale up laser ablation. Two of the newest developments towards large-scale synthesis are the use of Ultra Fast Pulses from a free electron laser [37], and the Continuous Wave Laser-Powder method [35]. Scaling up is possible, but the techniques are rather expensive due to the laser and the large amount of power required.

In summary laser ablation methods can produce SWNT of diameter 1-2nm with yields of up to 70%. Tubes tend to be long bundles of tubes of high purity.

2.3.3 High Pressure CO Disproportionation Process

First reported in 1999, the high pressure CO disproportionation process (HiPco) is a technique for catalytic production of SWNTs in a continuous-flow gas phase using CO as the carbon feedstock and $Fe(CO)_5$ as the Fe containing catalyst precursor[22]. SWNTs are produced by flowing CO, mixed with a small amount of $Fe(CO)_5$ through a heated reactor. Figure 2.10 shows the layout of a CO flow-tube reactor.

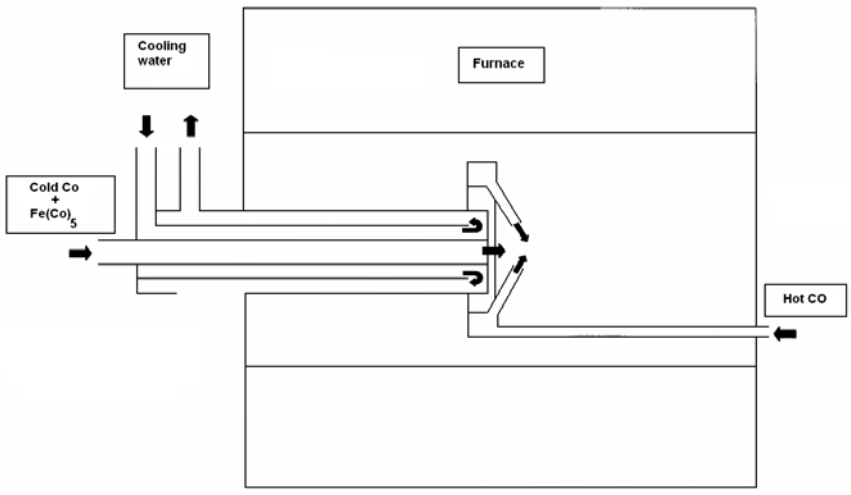

Figure 2.10: Layout of CO flow-tube reactor[22]

The products of the $Fe(CO)_5$ thermal decomposition react to produce iron clusters in the gas phase. These clusters act as nuclei upon which SWNTs nucleate and grow. The solid carbon is produced by CO disproportionation which occurs catalytically on the surface of the iron particles. These particles also promote the formation of the tube's characteristic graphitic carbon lattice. Size and diameter distribution of the nanotubes can be roughly selected by controlling the pressure of CO. This process is promising for bulk production of carbon nanotubes. Nanotubes as small as 0.7 nm in diameter, which are expected to be the smallest achievable chemically stable SWNTs[38], have been produced by this method. These tubes are found in bundles and the average diameter of HiPco SWNTs is approximately 1.1 nm[2][28]. The yield that could be achieved is approximately 70%. The highest yields and narrowest tubes can be produced at the highest accessible temperature and pressure [39].

In summary the HiPco method can produce SWNT of diameter 0.7-1.2 nm with a yield which depends on temperature and pressure. While purity levels of 60 - 80% are typical, up to 97% are possible[39].

2.3.4 Other Techniques

Other techniques have been used to produce single walled nanotubes. Chemical vapour deposition (CVD) synthesis is achieved by putting a carbon source in the gas phase and using an energy source, such as a plasma or a resistively heated coil, to transfer energy to a gaseous carbon molecule. Commonly used gaseous carbon sources include methane, carbon monoxide and acetylene[40]. The energy source is used to "crack" the molecule into reactive atomic carbon. Then, the carbon diffuses towards the substrate, which

is heated and coated with a catalyst (usually a first row transition metal such as Ni, Fe or Co) where it will bind. Carbon nanotubes will be formed if the proper parameters are maintained. Excellent alignment[40], as well as positional control on a nanometre scale[41], can be achieved by using CVD. Control over the diameter, as well as the growth rate of the nanotubes can also be maintained. The appropriate metal catalyst can preferentially grow single rather than multi-walled nanotubes[25]

In the CoMoCat process[42] SWNTs are grown by CO disproportionation at 700 – 950 ^{0}C. The technique is based on a unique Co-Mo catalyst formulation that inhibits the sintering of Co particles and therefore inhibits the formation of undesired forms of carbon that lower the selectivity. During the SWNT reaction, cobalt is progressively reduced from the oxidic state to the metallic form. Simultaneously Mo is converted to the carbidic form (Mo_2C). Co acts as the active species in the activation of CO, while the role of the Mo is possibly dual. It would stabilise Co as a well-dispersed Co^{2+} avoiding its reduction and would act as a carbon sink to moderate the growth of carbon inhibiting the formation of undesirable forms of carbon[42].

Flame synthesis is based on the synthesis of SWNTs in a controlled flame environment, that produces the temperature, forms the carbon atoms from the inexpensive hydrocarbon fuels and forms small aerosol metal catalyst islands [43][44][45]. SWNTs are grown on these metal islands in the same manner as in laser ablation and arc discharge. These metal catalyst islands can be made in three ways. Firstly the metal catalyst (cobalt) can be coated on a mesh[43], on which metal islands resembling droplets are formed by physical vapour

deposition. These small islands become aerosol after exposure to a flame. The second way[45] is to create aerosol small metal particles by burning a filter paper that is rinsed with a metal ion (e.g. iron nitrate) solution. The third way, is the thermal evaporation technique in which metal powder (e.g. Fe or Ni) is inserted in a trough and heated[44]. In a controlled way a fuel gas is partially burned to gain the right temperature of ~800 °C and the carbon atoms for SWNT production are released. On the small metal particles the SWNTs are then formed. As optimisation parameters the fuel gas composition, catalyst, catalyst carrier surface and temperature can be controlled[43]. In the available literature found, the yield, typical length and diameters are not stated.

The use of solar energy for synthesis of single walled nanotubes has been reported[46][47] using an experimental chamber where solar energy is focussed on the crucible to achieve a temperature of 3000 K on a clear day. A mixture of Ni and Y catalysts is used in an Ar atmosphere (pressure of approx 450 mbar). Further research is needed to optimise and control the synthesis process, increase the yield of tubes, minimize the concentration of carbon nanoparticles and amorphous carbon and to characterise the nanotubes produced.

2.5 Chapter Summary

The structures of SWNTs vary in both size and chirality leading to a range of physical properties. Due to their unique electrical properties, absorption spectroscopy and Raman spectroscopy are ideal techniques for their characterization. However although the signatures of individual carbon

nanotubes are discernible from bundled samples, the true characteristics and underlying physics of the SWNTs and their dependence on structure and state can only be determined in their debundled state. This will be explored further later on in the thesis. Production techniques currently employed yield batches composed of tubes with different diameters and chiralities which are bound together in bundles. The yield from many of these methods is not high enough to make them commercially viable as mass production techniques although some companies are commercially producing tubes[48]. The purity of the tubes is poor in many cases and further purification processes are necessary. Methods of isolation of particular tubes or tube types are also required.

2.6 References

[1] R.Saito, G.Dresselhaus, M.S.Dresselhaus, *Physical Properties of Carbon Nanotubes,* Imperial College Press, London (1998)

[2] E.Gregan, S.M.Keogh, T.Hedderman, G.Chambers, H.J.Byrne, SPIE Conference Proceedings “Opto-Ireland 2002, Optics and Photonics Technologies and Applications”, W.J. Blau, J.F. Donegan, A.F. Duke, B.D. MacCraith, J. A. McLaughlin, N.D. McMillan, G.M. O’Connor, E. O’Mongain and V. Toal eds., SPIE Proceedings Volume 4876, (2003), pp.1149

[3] J.W.G.Wildöer, L.C.Venema, A.G.Rinzler, R.E.Smalley, C.Dekker, Nature, **391**, 59(1998)

[4] C.H.Olk, J.P.Heremans, J.Mater. Res,**9**, 259-262 (1994)

[5] R.A.Jishi, D.Inomata, K.Nakao, M.S.Dresselhaus and G.Dresselhaus J.Phys.Soc.Jpn **63**, 2252-2260 (1994)

[6] P.Avouris, Researcher at the IBM labs, Lecture given at Michigan Sate University (2000)

[7] T.Spires and R.M.Browne: http://www.botany.utexas.edu/facstaff/facpages/mbrown/ongres/tspires/nano.htm (accessed 15th July 2007)

[8] T.W.Odom, J.L.Huang, P.Kim, C.M.Lieber, Nature, **391**, 62(1998)

[9] Strong, Anderson, Lafdi, Kuhn, Carbon **41**, 1477-1488 (2003)

[10] A.Thess, R. Lee, P.Nikolaev , H.Dai, P.Petit, J.Robert, C.Xu, Y.H.Lee, S.G.Kim, A.G.Rinzler, D.T.Colbert, G.E.Scuseria, D.Tománek, J.E.Fischer, R.E.Smalley, Science **273**, 483-487 (1996)

[11] G.Gao, T.Cagin, W.A.Goddard III http://www.wag.caltec.edu/foresight/foresight_2.html (accessed 15th July 2007)

[12] M.S.Purewal, Y.Zhang, P.Kim, Phys.Stat.Sol(b) **243**, 13 3418-3422 (2006)

[13] T. Ando, T. Nakaishi, and R. Saito, J. Phys. Soc. Jpn. **67**, 2857–2862 (1998)

[14] C.Kittel, *Introduction To Solid State Physics*, 8th edition Wiley and Sons, (2005)

[15] Y.Akai and S.Saito http://www.stat.phys.titech.ac.jp/saito/ldados.html (accessed 20th July 2007)

[16] G.Dresselhaus, M.A.Pimenta, R.Saito, Charlier, S.D.M.Brown, P.Corio, Marucci, M.S.Dresselhaus *Science and Applications of Nanotubes*, edited by D Tománek and R.J.Enbody, Kluwer Academic, New York (2000)

[17] S.M.Bachilo, M.S.Strano, C.Kittrell, R.H.Hauge, R.E.Smalley, R.B.Weisman, Science **298,** 2361-6 (2000)

[18] S.Iijima, Nature **354**, 56 (1991)

[19] T.W.Ebbesen, P.M.Ajayan Nature, **358**, 220-221, (1992)

[20] C.Journet, P.Bernier App. Phys. A-Materials Science & Processing, **67**, (1)**,** 1-9, (1998)

[21] T.Guo, P.Nikolaev, A.Thess, D.T.Colbert, R.E.Smalley, Chem. Phys. Lett. **243**, 1-2, (1995)

[22] P.Nikolaev, M.J.Bronikowski, R.K.Bradley, F.Rohmund, D.T.Colbert, K.A.Smith, R.E.Smalley, Chem. Phys. Lett., **313**, 1-2, (1999)

[23] M.Wilson, K.Kannangara, G.Smith, M.Simmons, B.Raguse, *Nanotechnology: Basic Science and Emerging Technologies* Chapmann and Hall (2002)

[24] A.Yasuda, N. Kawase, W. Mizutani, Journal of Physical Chemistry B, **106**, (51), (2002)

[25] S.B.Sinnot, R.Andrews, D.Qian, A.M.Rao, Z.Mao, E.C.Dickey, F.Derbyshire, Chem. Phys .Lett., **315**, 25-30, (1999)

[26] S.H.Jung, M.R.Kim, S.H.Jeong, S.U.Kim, O.J.Lee, K.H.Lee, J.H.Suh, C.K.Park, App. Phys. A-Materials Science & Processing, **76**, (2)**,** 285-286, (2003)

[27] C.Journet, P.Bernier App.Phys. A-Materials Science &Processing, **67,**(1) 1-9 (1998)

[28] S.M.Keogh, T.Hedderman, E.Gregan, G.Farrell, G.Chambers, H.J.Byrne, Phys. Chem. B, **108,** 6233-6241(2004)

[29] S.Farhat, I.Hinkov, D.I.Chapelle, S.S.Fan, G.H.Li, C.D.Scott, NASA Conference Publication, (2001)

[30] P.Costa, C.Xu, K. Coleman, J.Sloan, M.Green, Jour. Of Crystal Growth **244** 211-217 (2002)

[31] http://www.sigmaaldrich.com/catalog (accessed 10th November 2008)

[32] M.Yudasaka, R.Yamada, N.Sensui, T.Wilkins, T.Ichihashi, S.Iijima, Journal of Phys. Chem. B, **103**, 30, (1999)

[33] P.C.Eklund, B.K.Pradhan, U.J.Kim, Q.Xiong, J.E.Fischer, A.D.Friedman, B.C.Holloway, K.Jordan, M.W.Smith, Nano Lett. **2**, 6, (2002)

[34] W.K.Maser, E.Munoz, A.M.Benito, M.T.Martinez, G.F.de la Fuente, Y.Maniette, E.Anglaret, J.L.Sauvajol, Chem. Phys. Lett. **292**, 4-6, (1998)

[35] A.P.Bolshakov, S.A.Uglov, A.V.Saveliev, V.I.Konov, A.A.Gorbunov, W.Pompe, A.Graff, Diamond and Related Materials, **11**, 3-6, (2002)

[36] C.D.Scott, S.Arepalli, P.Nikolaev, R.E.Smalley, App. Phys. A: Materials Science & Processing, **72**, 5, (2001)

[37] H.Takikawa, Y.Tao, Y.Hibi, R.Miyano, T.Sakakibara, Y.Ando, S.Ito, K.Hirahara, and S.Iijima, AIP Conference Proceedings, 590, (Nanonetwork Materials), (2001)

[38] R.E.Smalley, B.I.Yakobson, Solid State Communications, **107**, 597, (1998)

[39] M.J.Bronikowski, P.E.Willis, D.T.Colbert, K.A.Smith, R.E.Smalley, Journ. Vacuum Science & Technology A: Vacuum, Surfaces and Films **19,** 4 (2001)

[40] Z.F.Ren, Z.P.Huang, J.W.Xu, J.H.Wang, P.Bush, M.P.Siegel, P.N.Provencio, Science, **282**, 5391, (1998)

[41] Z.F.Ren, Z.P.Huang, Z.P.Wang, J.G.Wen, J.W.Xu, J.H.Wang, L.E.Calvet, J.Chen, J.F.Klemic, M.A.Reed, App. Phys. Lett. **75**, 8, (1999)

[42] http://www.ou.edu/engineering/nanotube (accessed 12th September 2003)

[43] W.Vander, L.Randall L.J.Hall, G.M.Berger, Journal of Phys. Chem. B, **106**, 51, (2002)

[44] W.Vander, L.Randall, T.M.Ticich, Journal of Phys. Chem. B, **105**, 42, (2001)

[45] L.V.Wal, G.M.Berger, L.J.Hall, Journal of Phys. Chem. B, **106**, (14)**,** 3564-3567, (2002)

[46] Guillard, S.Cetout, L.Alvarez, J.L.Sauvajol, E.Anglaret, P.Biernier, G.Flamant, D.Laplaze, Eur.Phys.J.AP **5**, 251 (1998)

[47] D.Laplaze, P.Bernier, W.K.Maser, G.Flamant, T.Guillard, A.Loiseau, Carbon, **36**, 685-688 (1998)

[48] http://www.ptonline.com/articles/200707fal.html (accessed 21st September 2008)

CHAPTER 3

SPECTROSCOPIC TECHNIQUES

3.1 Introduction

Spectroscopy is concerned with the absorption, emission or scattering of electromagnetic radiation by atoms, molecules or solids. Therefore it can be defined as the study of the interaction of electromagnetic radiation with matter and can be used to provide accurate answers to important questions in relation to atomic and molecular structure. When an atom or molecule is exposed to electromagnetic radiation is may undergo rotational, vibrational, electronic or ionizing processes, in order of increasing energy as indicated in figure 3.1 below.

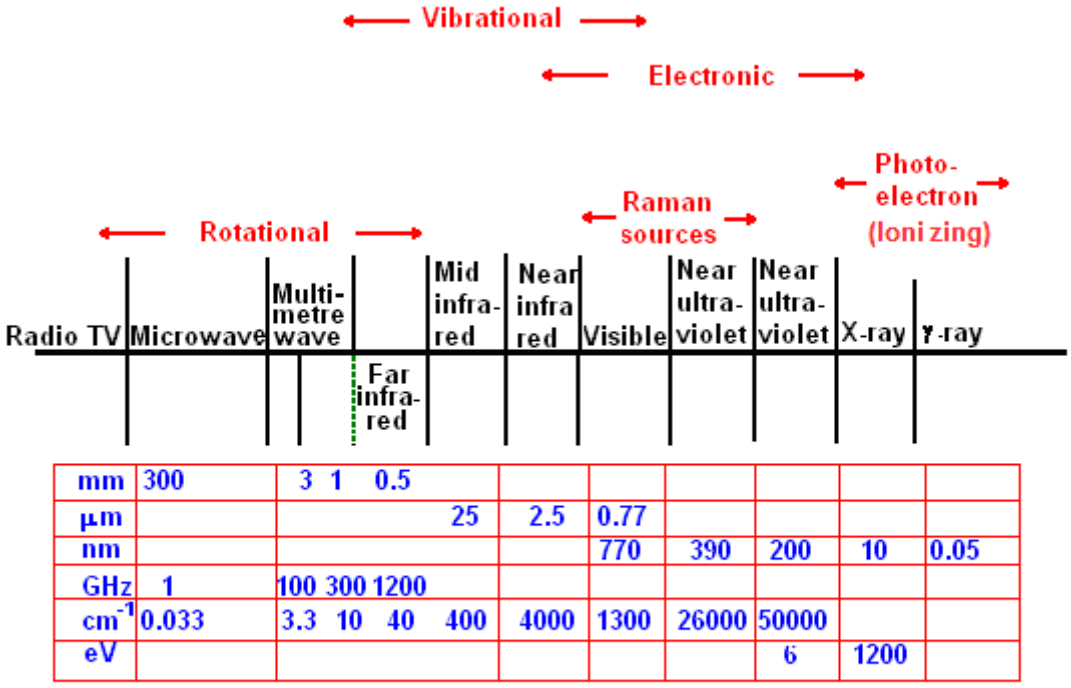

Figure 3.1: Molecular response to electromagnetic energy

Photo emission spectroscopy is confined largely to the visible and ultraviolet regions where spectra may be produced in an arc-discharge or by laser excitation. Photo absorption spectroscopy is generally a technique more used in all regions of the spectrum[1].

A molecule in space can manifest energy in many different ways; it may possess rotational energy by virtue of bodily rotation about its centre of gravity, whereby it will have vibrational energy due to the periodic displacement of its atoms from their equilibrium positions, and, in addition it will have electronic energy since the electrons associated with each atom or bond are in unceasing motion or potential[1]. In the same way that electronic energy is quantised, vibrational and rotational energies are also quantised. Transitions from one of these quantised energy states to another is only possible if the molecule is supplied with a discrete amount of energy equal to the difference in these energy states:

$$E_2 - E_1 = h\nu \qquad 3.1$$

where ν is the frequency, h is Planck's constant and E_1 and E_2 are the initial and final energy states respectively[1]. The significance of this is that if a molecule in state 1 is illuminated with a beam of radiation with photons of energy $h\nu$, then energy will be absorbed from this beam and the molecule will undergo a discrete transition to state 2. If, on the other hand, the radiation beam has a wide range of frequencies, analysis with a detector will show that only energies equal to $h\nu$ will have been absorbed, the intensity of all other energies remaining undiminished. Examination of the spectrum of absorbed energies gives vital information on the energies of the molecular vibrational states. Emission spectroscopy is just the converse of this. Which state is being probed in absorption or emission spectroscopy depends on the energy of the radiation absorbed or emitted. Infra- red spectroscopy probes the vibrational (and rotational) states of the molecules (as does Raman spectroscopy, see

section 3.3) whereas visible and ultraviolet spectroscopy probes the electronic transitions.

Spectroscopy is of particular importance in the study of the structure and the understanding of the properties of single walled nanotubes. Raman spectroscopy in particular is regarded as the chief diagnostic tool in the study of nanotubes and nanotube composites[2]. Absorption and fluorescence spectroscopy are also very important[2].

3.2 Absorption Spectroscopy

When a material absorbs energy from the ultraviolet or the visible part of the electromagnetic spectrum, excitation of the valence electrons occurs. This excitation of electronic charges in the molecules of the material causes changes to the electric dipoles. This change in electric dipole gives rise to a spectrum via the interaction with the undulating electric field of the radiation. UV-Visible spectra have broad features that are of limited use for sample identification of most materials but are very useful for quantitative measurement. One such example is the application of the Beer-Lambert law to calculate the concentration of solute in a solution from the sample absorbance A.

The Beer-Lambert Law[3] states that

$$A = \alpha l c \qquad 3.2$$

$$A = -\log_{10} \frac{I}{I_0} \qquad 3.3$$

where I is the intensity of the transmitted light, I_0 is the incident light intensity, c is the concentration and l is the path length of the sample. The absorption coefficient

$$\alpha = \frac{4\pi k}{\lambda} \qquad 3.4$$

where *k* is known as the extinction coefficient and λ is the wavelength of the absorbed radiation. Combining 3.2 and 3.3 gives

$$A = \frac{4\pi kl}{\lambda} c \qquad 3.5$$

All types of nanotubes are active in UV-Vis-NIR region. A typical absorption spectrum of a SWNT powder dispersed in thin film form can be seen in figure 3.2 below.

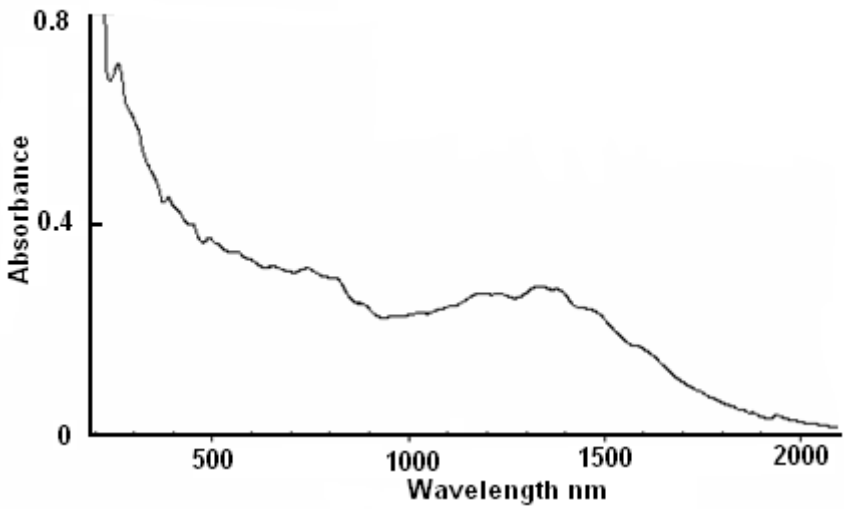

FIGURE 3.2: Typical absorption spectrum for single walled carbon nanotubes[4]

When measured using a single source over the visible region, SWNTs exhibit characteristic peaks of absorption due to 1D van Hove singularities[5]. Semiconducting SWNT's are characterised by absorptions in two regions originating from transitions between the principal mirror spikes in the electronic

density of states E_{11}^{S} and E_{22}^{S} whereas the metallic SWNTs show only their first transition E_{11}^{M}. The simplest theoretical treatments predict a simple inverse relationship between transition energy and diameter for these transitions[1]

$$E_{11}^{S} = \frac{2k}{d}$$
$$E_{22}^{s} = \frac{4k}{d} \qquad 3.6$$
$$E_{11}^{M} = \frac{6k}{d}$$

However, more recently it has been shown experimentally that the relationship is more complicated and that

$$E_{11}^{S} = hc\left[\frac{1x10^{7}\,cm^{-1}}{157.5+1066.9d} + \frac{A_1 Cos(3\theta)}{d^{2}}\right] \qquad 3.7$$

$$E_{22}^{S} = hc\left[\frac{1x10^{7}\,cm^{-1}}{145.6+575.7d} + \frac{A_2 Cos(3\theta)}{d^{2}}\right] \qquad 3.8$$

θ being the chiral angle[6].

Prominent features can be found as unresolved peaks for E_{11}^{S} near 1700nm, E_{22}^{S} near 1000 nm and E_{11}^{M} near 700 nm[7]. These features consist of several van Hove transitions of nanotubes of different diameters. Therefore the spectral positionings depend on the diameter distribution of the sample and the tube bundle size. Absorption spectra of bundled tubes, as with Raman

spectroscopy, are convoluted in nature[5]. Individual van Hove transitions of solitary nanotubes can become resolved in suspension[6]. Measurement of areas of prominent features have been used to estimate SWNT purity[7] and concentration.

Absorption spectroscopy has also been utilised to probe the aggregation state of SWNTs[9][10]. In this work, absorption spectroscopy is similarly employed to probe the concentration dependent aggregation state of SWNTs in the three identified solvents, DCE, DMF and toluene.

3.3 Raman Spectroscopy

When a beam of light is passed through a transparent substance, a small amount of the radiation energy is scattered. If monochromatic radiation, or radiation of a very narrow frequency band is used, the scattered energy will consist almost entirely of radiation of the incident frequency (Rayleigh scattering), but in addition certain discrete frequencies above and below that of the incident beam will be scattered. This extra inelastic scattering component is referred to as Raman scattering[3].

The occurrence of Raman scattering is best understood in terms of the quantum theory of radiation[3]. Photons undergo collisions with molecules and if the collisions are perfectly elastic, they will be deflected unchanged. However, it may happen that energy is exchanged between photon and molecule during the collision i.e. the collision is inelastic. The molecule will gain or lose amounts of energy as a result of such collisions in accordance with the laws of

quantum theory. In other words, this change in energy $\Delta E=E_1-E_2$ must represent a change in the vibrational and/or rotational energy of the molecule. Radiation scattered with a frequency lower than that of the incident beam is referred to as 'Stokes' radiation while that at a higher frequency is referred to as 'anti-Stokes' radiation. Since Stokes radiation is accompanied by an increase in molecular energy (which can always occur), while anti-Stokes involves a decrease in molecular energy (which can only occur if the molecule is originally in an excited vibrational state), Stokes radiation is generally more intense than anti-Stokes radiation at room temperature since most materials are in their lowest vibrational states at room temperature.

To understand the Raman effect, consider what happens to a molecule when it is placed in a static electric field. The molecule will be distorted, the positive nuclei being attracted towards the negative pole of the field while the electrons will be attracted towards the positive pole of the field. This separation of charge causes an induced electric dipole moment to be set up in the molecule. The molecule is said to be polarised. The size of this induced dipole, μ, depends on both the magnitude of the applied field, E, and on the ease with which the molecule can be distorted. It therefore is the case that

$$\mu = \alpha E \qquad 3.9$$

where α is the polarizability of the molecule[1].

When a molecule is subjected to a beam of electromagnetic radiation of frequency ν, the electric field experienced by each molecule varies according to the equation

$$E = E_0 \sin 2\pi\nu t \qquad 3.10$$

The induced dipole also undergoes oscillations of frequency ν:

$$\mu = \alpha E = \alpha E_0 \sin 2\pi\nu t \qquad 3.11$$

Such an oscillating dipole emits radiation of its own oscillation frequency, the classical explanation of Rayleigh scattering. If, in addition, however, the molecule undergoes some internal motion, such as vibration or rotation which changes the polarizibility periodically, then the oscillating dipole will have superimposed on it the vibrational or rotational oscillation. For example consider a vibration of frequency ν_v which changes the polarizibility.

$$\alpha = \alpha_0 + \beta \sin 2\pi\nu_v t \qquad 3.12$$

where α_0 is the equilibrium polarizability and β represents the rate of change of polarizability with the vibration. Therefore

$$\mu = \alpha E = (\alpha_0 + \beta \sin 2\pi\nu_v t) E_0 \sin 2\pi\nu t \qquad 3.13$$

Expanding and using the trigonometric relation

$$\sin A \sin B = \frac{1}{2}\{\cos(A-B) - \cos(A+B)\}$$

equation 3.13 becomes

$$\mu = \alpha_0 E_0 \sin 2\pi\nu t + \frac{1}{2}\beta E_0 \{\cos 2\pi(\nu - \nu_v)t - \cos 2\pi(\nu + \nu_v)t\} \qquad 3.14$$

From this equation it can be seen that the dipole not only oscillates at the exciting frequency ν, but also has frequency components $\nu \pm \nu_v$. These frequency components are the origin of the Stokes and anti-Stokes shifted Raman scattering. It should be noted that if the vibration (or rotation) does not alter the polarizability, then β =0 and the dipole oscillates only at the frequency of the incident radiation. So in order to be Raman active a molecular rotation or

vibration must cause some change in the component of the molecular polarizability. The Raman scattering cross section also depends on the occupancy of the initial level. The occupancy of the vibrational levels is determined by Boltzmann statistics. Thus, at low temperatures, only the ground state vibrational states are occupied and the anti-Stokes scattering goes to zero. If the vibrational population is initially in thermal equilibrium at absolute temperature T then the intensity ratio of the two lines is given by

$$\frac{I(\nu+\nu_\nu)}{I(\nu-\nu_\nu)} = \exp\left(\frac{-h\nu_\nu}{k_B T}\right) \qquad 3.15$$

where ν_ν is the Stokes shift, h Planck's constant and k_B Boltzmann's Constant[11].

In Raman spectroscopy, which measures the spectrum of vibrations which couple to the radiation field, of interest is the Raman shift. Therefore the laser frequency is set to zero and the Stokes side is usually measured (in wavenumbers for comparison to infra red spectroscopy) and taken to be positive.

It should be noted that in a simple harmonic model of a diatomic model, the vibrational frequencies are proportional to $(k/m)^{1/2}$[5], where k is the spring constant (or bond strength) and m is the effective mass of the molecule in question. In more complex molecules, the vibrations can be described in terms of the normal modes of constituent groups (e.g. C-H) and the more collective

multi-atomic vibrations which give rise to a fingerprint of the molecule. In solids, vibrations of individual atoms couple to give collective oscillations which can propagate throughout the material. These coupled oscillations are called phonons.

3.4 Raman Spectroscopy of Single Walled Carbon Nanotubes

Raman spectroscopy has been employed for the study of carbon nanotubes for some time[2]. Usually Raman spectra only involve vibrations or phonons, being independent of the electronic structure and the laser energy used to excite the Raman spectra. Also the usual Raman scattering signal is weak. However the scattering efficiency increases when the laser energy matches the energy between optically allowed electronic transitions in the material and this intensity enhancement process is called resonance Raman scattering[1]. The resonance Raman intensity depends on the density of electronic states available for optical transitions and this is very important in 1-D systems such as single walled carbon nanotubes, as described in chapter 2, section 2.2.

A strong resonantly enhanced Raman signal from SWNTs can be obtained when the laser energy is equal to the energy separation between the van Hove singularities in the valence and conduction bands, but restricted by the selection rules for optically allowed electronic transitions[13][14][15]. Raman spectra at the single nanotube level allow the study of the electronic and phonon structure of single walled carbon nanotubes in great detail. When Raman spectra of bundled samples are taken, only those tubes with E_{ii} in

resonance with the laser excitation energy will contribute strongly to the spectrum.

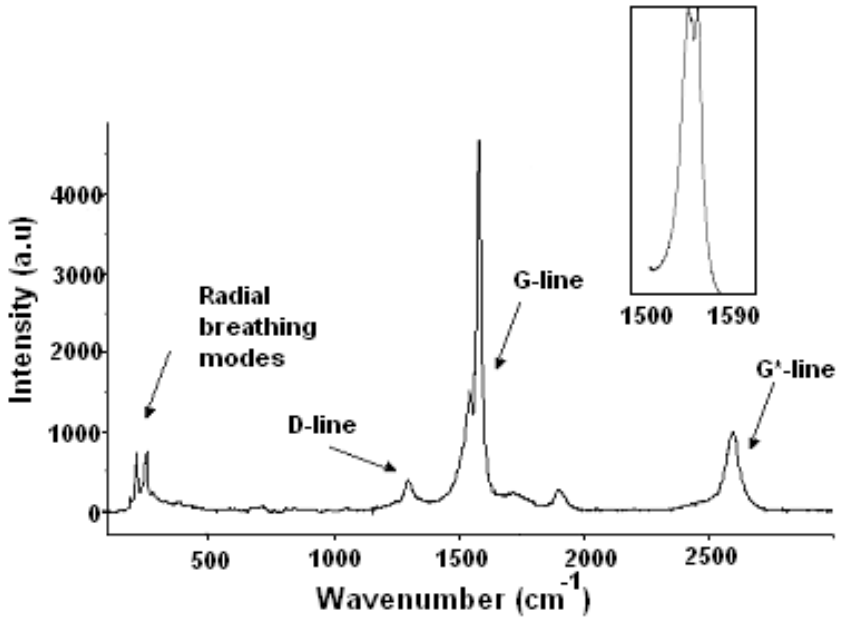

Figure 3.3: Stokes Raman spectrum of semiconducting nanotube taken at 633 nm with inset of metallic nanotube G-line shape[4]

A typical Raman spectrum as seen in figure 3.2 shows four main regions: the G-line, the D-line, the G*-line and the radial breathing modes (RBMs).

3.4.1 The G-Line

The G-line originates from the C=C stretching mode in graphene, an optical phonon mode, which consists of peaks around 1582 cm^{-1}. In single walled carbon nanotubes this peak is doubly split into higher and lower sides of the 1582 cm^{-1} line, G^+ (frequency ω_G^+) and G^- (frequency ω_G^-), due to the curvature of the graphene sheet. The lineshape that results is indicative of the electronic nature of the carbon nanotube[16].

It has been predicted from group theory and phonon frequency calculations that the two main peaks of the G-band consist of a number of modes. In particular, it consists of two A, two E_1 and two E_2 phonon modes for chiral nanotubes and of one A_{1g}, one E_{1g} and one E_{2g} mode for achiral (armchair or zigzag)[17].

A semi-conducting tube produces a G-line which is Lorentzian in shape[16][18]. The G^+-line arises from the atomic displacements along the tube axis, (longitudinal optical, LO phonon mode), and the G^--line from modes with atomic displacement along the circumferential direction, (transverse optical, TO phonon mode) as shown in figure 3.4.

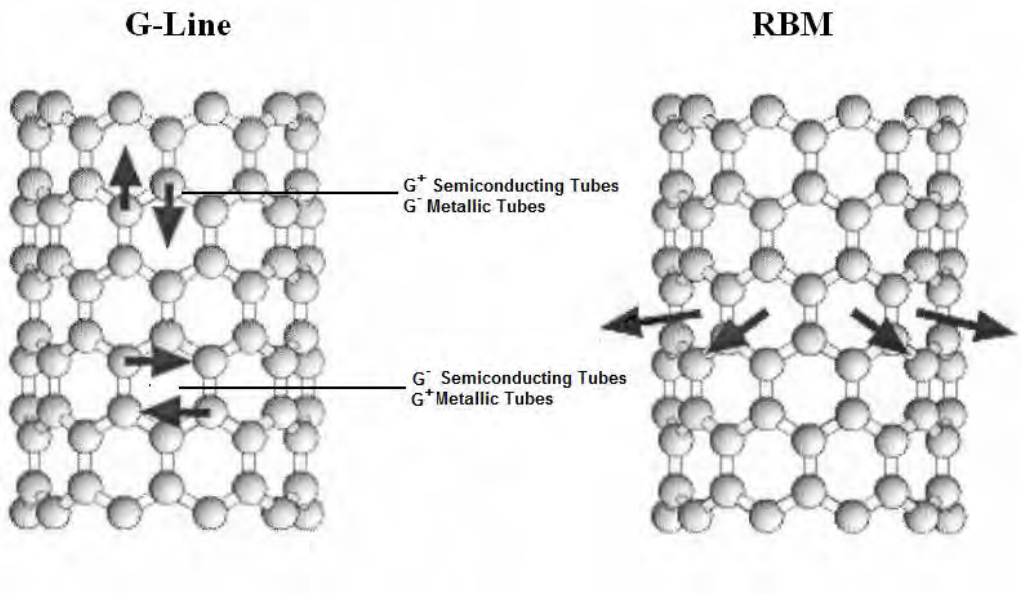

Figure 3.4: Schematic picture showing the atomic vibrations for (a) G-line and (b) RBM modes[adapted from 4]

Examination of the G-line features for isolated tubes shows that the higher component ω_G^+, is essentially independent of tube diameter and non dispersive. However the lower component ω_G^- is dependent on tube diameter[19] and decreases in frequency in accordance with

$$\omega_G^- = \omega_G^+ - \frac{C}{d_t^2} \qquad 3.16$$

where d_t is the tube diameter, and C=47.7 $cm^{-1}nm^2$ for semiconducting tubes and C=79.5 $cm^{-1}nm^2$ for metallic tubes.[18]. So in isolated tubes the value of $\Delta\omega_G = \omega_G^+ - \omega_G^-$ can be used for diameter characterisation and defines the particular tube in question. The linewidths Γ_{G+} for the G peaks from isolated semiconducting SWNTs are usually around 5 -15 cm^{-1}, and the same range of linewidths for Γ_{G-} has been found[20]. The frequency of G^+- line, ω_G^+, is sensitive to charge transfer from dopant additions to single walled carbon nanotubes. Upshifts in ω_G^+ for acceptors and downshifts for donors have been documented[21][22]. The G-line for bundles also shows the two features whose spacing depends on the mean diameter of the nanotube bundle. In semiconducting tube bundles the frequency of G^+-line is determined by bundle size, $\Delta\omega_G$ is approximately related to the maximum in the Gaussian diameter distribution of the sample, but does not reflect the diameter dependence of ω_G^-[23]. For semiconducting SWNTs in bundles, the linewidths are determined by the intertube interactions and the diameter distribution. Therefore broadening principally occurs for Γ_{G-}. It should be noted that the G-line is a first order resonance and its spectral positioning is independent of the laser energy used to obtain the spectrum.

In metallic tubes, the G^--line feature is broadened. This broadening is related to the presence of free electrons in nanotubes with metallic character. A metallic nanotube shows a Breit-Wigner-Fano (BWF) line shape that accounts for the coupling of a discrete phonon with a continuum of conduction electrons[5][24][25].

The use of density functional theory to calculate optical phonons and electron-phonon coupling (EPC) shows that in fact the frequency of the longitudinal optical phonon mode is always lower than the transverse optical phonon mode in metallic nanotubes[26]. This means that in metallic nanotubes, the G^+-line arises from atomic displacements along the circumferential direction and the G^--line from atomic displacements along the tube axis, as indicated in figure 3.4. In metallic bundles the intensity of the BWF line increases strongly with bundle size[27] which identifies the line as an excited band of intertubular plasmon-phonon modes. It has also been shown that the BWF line vanishes in isolated metallic tubes implying that it is an intrinsic feature of metallic bundles[28]. For individual metallic SWNTs, the broadening is minimal and for isolated tubes with d_t > 2 nm, Γ_{G^-} is similar to that of semiconducting SWNTs, and the line mostly looks like a normal Lorentzian, reflecting the small magnitude of the BWF effect in isolated nanotubes compared to bundles.

3.4.2 The D and G*- Lines

The intensity of the D-line was thought until recently to be a measure of the amount of carbonaceous impurities in the sample. However, more recently it is thought to be a measure of the level of defects along the tube itself. There is also some indication that the D-line resonance is effected by the electronic nature of the tubes[29] . It has also been shown that the D-line and its second harmonic, the G*-line, vary in both value and amplitude with laser excitation frequency[30][31][32]. The variation in frequency of the lines with change in excitation energy is given by equations 3.17 and 3.18.

$$\frac{\delta\omega_d}{\delta E_{laser}} = 53 cm^{-1} eV^{-1} \qquad 3.17$$

$$\frac{\delta\omega_{G^*}}{\delta E_{laser}} = 106 cm^{-1} eV^{-1} \qquad 3.18$$

Both lines are highly dispersive and are observed in both isolated tubes and bundles. However, in bundles, superimposed on the linear dependence of ω_D and ω_{G^*} on laser energy (equations 3.17 and 3.18), is an oscillatory feature due to resonance of the laser energy with specific van Hove singularities leading to a dependency on both diameter and chirality[29]. It has been further shown that this D-line dependency is different for semiconducting and metallic tubes[33][34]. However, when averaging over different chiralities, the dependence of ω_D and ω_{G^*} on diameter can be expressed in the form

$$\omega = \omega_0 - \frac{C}{d_t^n} \qquad 3.19$$

where n has a value of 1 and C has a value of -16.5 cm^{-1} for the D-line and -35.4 cm^{-1} for the G*-line[35]. Recently it has been proposed[36] that the excitation energy and diameter dependence of ω_{G^*} are separable and can be described by

$$\omega_{G^*} = \omega_{G^*}^0 + \frac{\delta\omega_{G^*}}{\delta E} xE - \frac{c}{d_t^n} \qquad 3.20$$

Here c and $\omega_{G^*}^0$ are assumed to be independent of E and d_t.

The D-line intensity is large compared to that of the G-line when the sample has a large number of defects or impurities while the G^*-line intensities are always large compared to the G-line even when there are no defects. Therefore the ratio of G/D line and G^*/D line intensities provides a good index for showing the presence of defects, increasing as they do with increasing order and purity[32][37][38]. Although the G*-line is reported to be the second order

harmonic of the D-line, its frequency is not exactly twice that of the D-line. It should also be noted that the value of the Stokes and anti-Stokes frequencies of the D and G* lines are not the same[39].

The G*-line arises from a two-phonon, intervalley, second order Raman scattering process[1][30][40]. For a high quality sample, the G*-line spectra are completely free from defect contributions and the intensity is comparable with that of the G-line. Although the G*-line appears as a single peak in most graphene materials, it sometimes appears, at the individual nanotube level, as a two- peak structure for both semiconducting and metallic tubes[41][42][43]. The presence of the two peaks from semiconducting tubes indicates resonance with two different van Hove singularities of the same nanotube, occurring independantly for both the incident E_L and scattered E_L-E_{G^*} photons when the van Hove singularities are sufficiently separated in energy (outside their respective resonance windows)[44].

3.4.3 The Radial Breathing Modes

In the lower frequency region, the spectrum is dominated by the in-phase mode known as the radial breathing mode (RBM), shown in figure 3.4. These features correspond to the vibration of C atoms in the radial direction, as if the tube was "breathing". The frequency of the RBM (ω_{RBM}) is inversely proportional to the nanotube diameter (d_t).

$$\omega_{RBM} = \frac{A}{d_t} + B \qquad 3.21$$

where the constant of proportionality, A, and the spectral shift B, are empirically determined parameters. For bundles in the diameter range d_t= 1.5 ± 0.2 nm, A

= 234 nm cm^{-1} and B = 10 cm^{-1}[45]. B is an upshift coming from intertubular interaction [43]. For isolated tubes

$$\omega'_{RBM} = \frac{A'}{d_t} \qquad 3.22$$

Here A' = 248 nm cm^{-1}[46]. For the diameter range 1< d_t < 2 nm these two sets of parameters give similar values of diameter for a given ω_{RBM}. For d_t<1 nm, equation 3.14 is not expected to hold due to nanotube lattice distortions leading to a chirality of ϖ_{RBM} [47]. For large nanotubes of d_t > 2 nm, the intensity of the RBM feature is weak and hardly observable.

The spectral shape and position of the Raman band associated with the RBM of the nanotubes present in a sample provide an estimate of the diameter distribution in the SWNT sample[45][46]. It should be noted that tubes which are most apparent in a spectrum are those which are resonantly enhanced at the wavelength employed. This is because of the one dimensional density of states bands which are sharp and narrow. Therefore, within a sample, only some tubes are resonant at a given wavelength and in order to characterise fully a given sample, it is necessary to use a range of excitation frequencies[45]. The natural linewidth (FWHM) for an isolated tube on a SiO_2 substrate is approximately 3 cm^{-1}[23].

It is useful to have a plot of resonant transition energies E_{ii} as a function of tube diameter d_t for all (n,m) single wall nanotubes. Such a plot has become known as a Kataura plot, from the name of the author of the paper in which it was first presented[5]. Such a plot is shown in figure 3.5. From this plot it can be seen

that not only are the E_{ii} values approximately inversely proportional to $d_{t,}$ as described by equation 2.11, but that each E_{ii} band has some width due to the chirality dependence of E_{ii}.

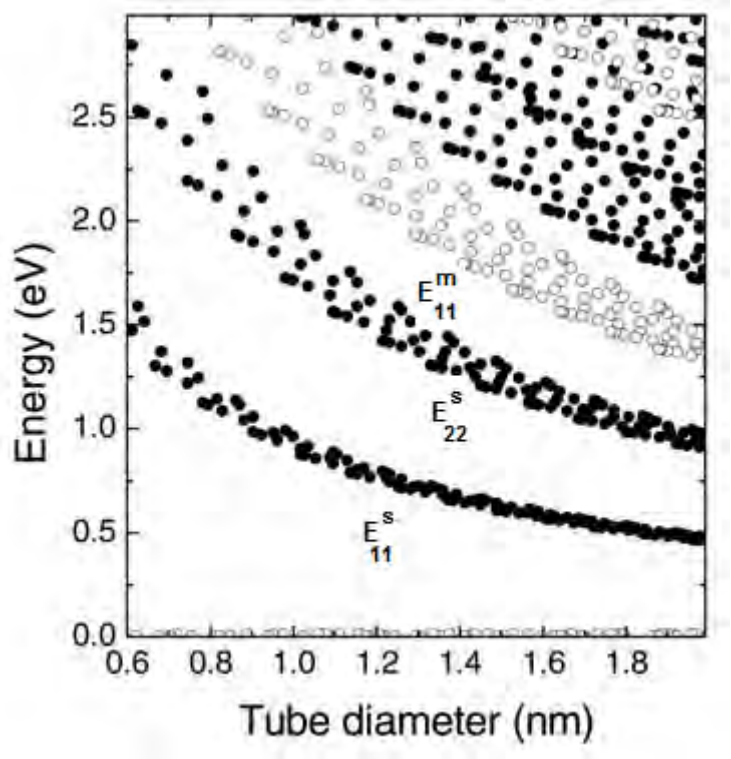

FIGURE 3.5: Plot of the Transition Energies E_{ii} of semiconducting (filled symbols) and metallic (open symbols) versus Tube Diameter d_t for all (n,m) values occurring 0.6<2.0 nm , Kataura Plot.[48]

Wang et al[49] developed a graphical method for assigning Raman peaks of radial breathing modes of single walled carbon nanotubes. The charts were constructed based on data of diameters, RBM frequencies and electronic density of states of single walled carbon nanotubes. This can be seen in figure 3.6.

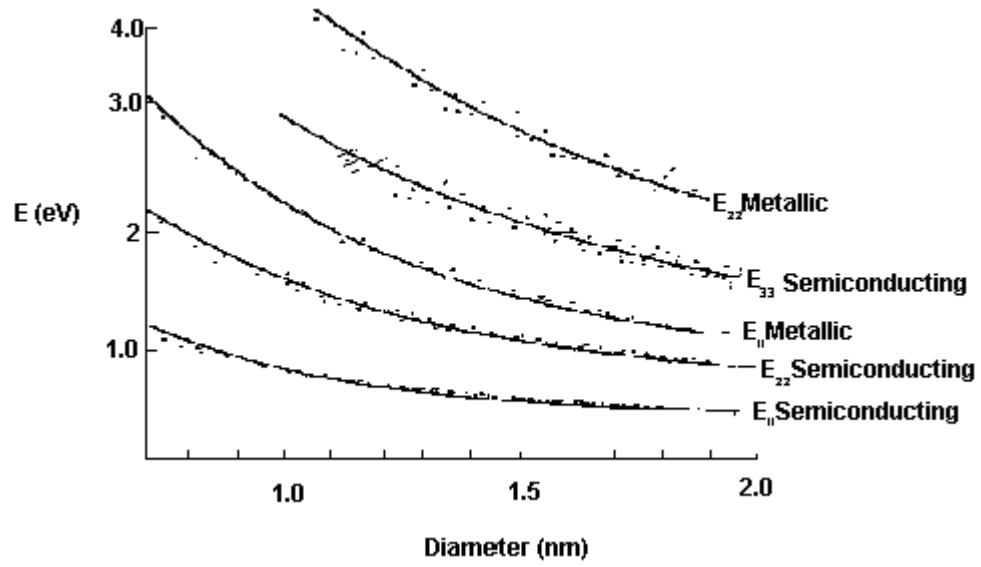

FIGURE 3.6: Wang Diagram for the Graphical Assignment of Resonance Tube Diameters with Laser Energy[Adapted from 49]

Studies which plot the intensity changes of ϖ_{RBM} as a function of E_{laser} have been carried out and show some interesting results[50]. Family patterns were observed based on the family being defined as (2n+m) = const. Furthermore different behaviour is observed for MOD1 and MOD2 semiconducting tubes. MOD 1 describes tubes where the remainder of (2n+m)/3 =1 and MOD 2 where the remainder =2. This can be seen in figure 3.7 taken, from reference 50.

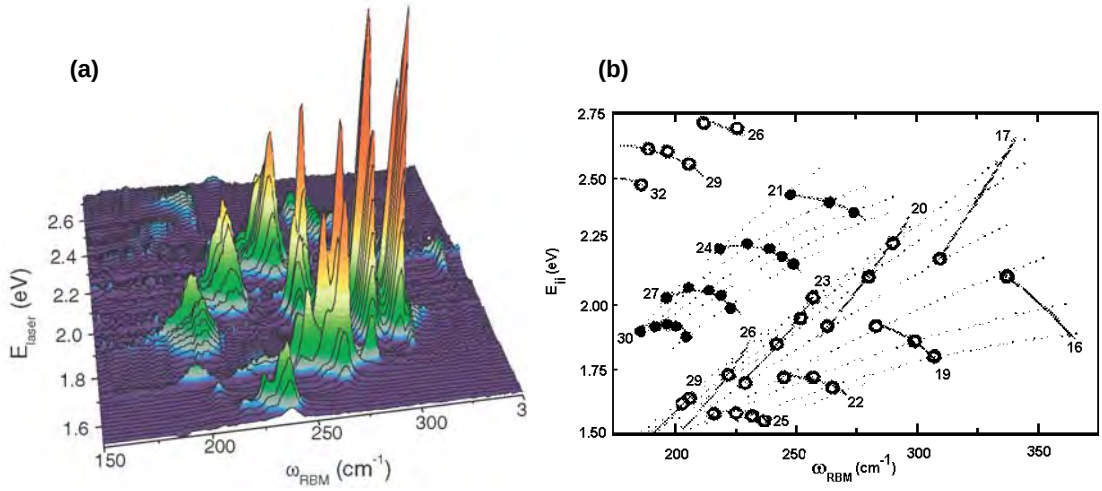

FIGURE 3.7: (a) RBM Raman Measurements of HiPco SWNT's Measured with 76 different Laser Lines E_{Laser} (b) The points denote electronic transition energies E_{ii} vs $\omega_{RBM.}$ ● and ○ denote metallic and semiconducting SWNT's, Each family is denoted by its (2n+M) = constant value, allowing family patterns to be clearly seen[50]

For samples of many isolated tubes or bundles of tubes, a single Raman measurement gives an idea of the tubes that are in resonance with the laser line but does not give a complete characterisation of the diameter distribution of the sample. This is the disadvantage of Raman spectroscopy over absorption spectroscopy where excitation with a number of different energies (sources) is necessary before the full range of diameter tubes present can be examined. Since semiconducting and metallic tubes of similar diameter do not have similar E_{ii} values, ϖ_{RBM} measurements using several laser energies can be used to characterise the ratio of metallic to semiconducting SWNTs in a given sample[51].

Studies of samples of isolated tubes using lattice dynamical predictions indicate that isolated tubes should have lower ϖ_{RBM} values than those in bundles[52]. However it has been observed that the frequencies actually upshift by

approximately 10 cm^{-1} for single tubes in solution due to a decreased energy spacing of the van Hove singularities in isolated tubes compared to the spacings in bundles thereby allowing the same laser excitation to excite different diameter tubes in the two samples[53]. The net effect of debundling is an apparent up-shift in the RBM features.

When the Stokes and anti-Stokes spectra from SWNTs are compared, they show unique characteristics when compared to other systems. Whereas for 2D and 3D sp^2 carbon materials the Stokes and anti-Stokes tangential bands at a given E_{Laser} value are almost identical, the unusual resonant Raman process for carbon nanotubes gives rise to differences in the Stokes and anti-Stokes tangential band spectra when one resonance is within the window of E_{Laser} for metallic nanotubes and the other is not. Brown et al[39] reported a systematic study of the Stokes and anti-Stokes spectra for SWNT bundles with emphasis on the G band where the laser excitation E_{Laser} was specifically chosen to show large asymmetries between the Stokes and anti-Stokes spectra. This asymmetry is due to the unique resonant enhancement phenomena arising from the one-dimensional density of states of the nanotubes. The most dramatic asymmetries were observed when metallic nanotubes in the bundle were resonant in the anti-Stokes spectrum and semiconducting tubes were resonant in the Stokes (or vice versa) spectrum at the same incident photon energy E_{Laser}. Large asymmetries were also reported for the RBM region and these were attributed to the coexistence of resonant and non-resonant Raman scattering processes for SWNTs with different diameters[39]. This means that different tubes are resonant in the Stokes and anti-Stokes spectra for a given

E_{Laser}. Comparison between the Stokes and anti-Stokes spectra show that the resonance Raman process is stronger for metallic than semiconducting tubes. A consequence of this is that if a particular ϖ_{RBM} appears in both the Stokes and anti-Stokes for a certain E_{Laser} this must mean that the corresponding tube is not resonant at that excitation frequency and therefore must be present in large amounts for the intensity to match those of resonant tubes[54]. Whereas the ratio of the intensity of the anti-Stokes to the intensity of the Stokes is commonly used to determine the temperature in materials, due to the asymmetries in the two spectra in SWNTs, this ratio, see equation 3.15, is used to determine the E_{ii} accurately and to resolve ambiguities in the (n,m) assignment between two or more candidates having similar d_t values[55].

3.4.4 Temperature Dependent Raman

A study of the temperature dependence of the Raman spectra can provide important insights into the relationship between the spectra, electronic state distribution and structure of single walled carbon nanotubes. Previous studies have found that the D and G peak positions downshift from room temperature positions with increasing temperature[56]. The origin of this shift comes from the temperature dependence of the Raman frequency shift given by[57][58]

$$\omega = \varpi_0 - \alpha_1 T - \alpha_2 T^2 \tag{3.23}$$

where ω_0 is the frequency when T is extrapolated to 0K, and α_1 and α_2 are the first and second order temperature coefficients respectively. Studies have shown that this downshift is in fact linear with temperature for temperatures well

below the Debye temperature of the graphite layer of 2500 K[59][60]. Differing temperature coefficients have been calculated for a range of different types of SWNTs but typical values for the G-line are -0.023 cm^{-1}/K, D-line -0.019 cm^{-1}/K and G*-line -0.034 cm^{-1}/K[59]. Various groups have in fact interpreted the temperature dependence as being due to the lengthening of C-C bonds due to thermal expansion[56][59][60]. The radial breathing modes have also been found to be sensitive to temperature. It has been shown in some studies that the RBM features retain their primary line shape but shift to lower frequencies linearly with increasing temperature up to 700 K[60][61][62]. However, in another study, in contrast, a significant change in line shape was found from 150 to 610 K instead of a simple downshifting in the frequency[23]. In a study by Zhang et al., it is suggested that this could be explained in terms of competing effects between the softening of the interatomic force constant due to thermal expansion of the C-C bonds and relaxation of the weak van der Waals interaction between SWNT's in bundles with increasing temperature[63]. Work on bundles and surfactant coated tubes indicated that the optical transition energies E_{ii} shifted with temperature although it was not possible to determine by how much or in which direction[58][59]. More recently, Cronin et al. calculated the temperature dependence of the optical transition energies of individual nanotubes suspended in air[64]. They found a definite decrease in E_{ii} with temperature. Theoretical modelling suggested that this was due to the dominance of electron-phonon coupling whereas the temperature dependence of optical transitions in bundles and coated tubes was dominated by the thermal expansion of the nanotube environments.

It was also found that the intensity of the spectra of these individual tubes decreased monotonically with increasing temperature. As will be discussed further in chapter 7, the temperature dependence of the Raman scattering efficiencies is dependent on the relative contributions of phonon-phonon and electron-phonon scattering efficiencies, which may be expected to differ significantly in bundles as compared to isolated nanotubes. There is thus clearly a need for further temperature dependence studies to be carried out to clearly differentiate between bundles and isolated tubes.

3.5 Conclusion

Although a lot of work has been carried out in establishing both theoretically and practically the spectroscopic characteristics of single walled carbon nanotubes, more needs to be done. Previous studies compared the spectroscopy of bundles to isolated tubes exploring the signatures and changes between the two. The properties of bundles cannot be directly applied to isolated tubes, however, and little work has been devoted to examining the changes to the fundamental properties as one goes from large bundles to smaller bundles to isolated tubes. This type of study is necessary both in terms of establishing a fundamental understanding of the differences in nanotube samples and establishing a practical characterization technique. This is the approach taken in the work described in this thesis. Organic solvents are used to debundle single walled nanotubes. The process and degree of debundling is examined using absorption spectroscopy and the highly capital and low through put techniques of TEM and AFM. Complementarily changes in the Raman spectra are

measured as one goes from a highly bundled state to a lower degree of bundling. These changes are examined and the use of previously unidentified spectral markers of the degree of debundling are identified. Finally, using Raman spectroscopy, a temperature dependent study is carried out on bundled and debundled tube samples.

Changes in both the absorption spectrum and the Raman spectrum will be characterized and compared for different SWNT samples from different production methods therefore containing different diameter ranges and bundle sizes.

3.6 References

[1] R.M.Martin, L.M.Falicov, Light Scattering in Solids I (Springer Series in Topics in Applied Physics vol 8), ed. M. Cardona (Berlin: Springer) chapter 3 pg 70 (1983)

[2] R.Saito, G.Dresselhaus, M.S.Dresselhaus, Physical Properties of Carbon Nanotubes, Imperial College Press, London (1998)

[3] J.M.Hollas Modern Spectroscopy 4th edition Wiley (2004)

[4] E. Gregan, S.M. Keogh, T.G. Hedderman, G. Chambers, H.J. Byrne, "Opto-Ireland 2002, Optics and Photonics Technologies and Applications", W.J. Blau, J.F. Donegan, A.F. Duke, B.D. MacCraith, J. A. McLaughlin, N.D. McMillan, G.M. O'Connor, E. O'Mongain and V. Toal eds., SPIE Proceedings Volume **4876**, pp.1149 (2003)

[5] H.Kataura, Y.Kumazawa, Y.Maniwa, I.Umezu, S.Suzuki, Y.Ohtsuka, Y.Achiba, Synthetic Metals, **103,** 2555(1999)

[6] S.M.Bachilo, M.S.Strano, C.Kittrell, R.H.Hauge, R.E.Smalley, R.B.Weisman, Science **298,** 2361-6 (2000)

[7] A.G.Ryabenko, T.V..Dorofeeva, G.I.Zvereva, Carbon **42,** 1523-1535 (2004)

[8] M.J.O Connell, S.M.Bachilo, C.B.Huffman, V.C.Moore, M.S.Strano, E.H.Haroz et al, Science **297,** (5581) 593-6 (2002)

[9] P.Bashir, H.J.Byrne J. Phys. Chem. C **112**, 332 (2008)

[10] S.Giordani, S.D.Bergin, V.Nicolosi, S.Lebedkin, M.M.Kappes, W.J.Blau, J.N.Coleman J.Phys.Chem B **110,** 15708-15718 (2006)

[11] C.Kittel, Introduction To Solid State Physics, 8th edition Wiley and Sons, (2005)

[12] E.Smith, G.Dent Modern Raman Spectroscopy – A Practical Approach Wiley and Sons (2005)

[13] M.F.Lin, Phys. Rev.B **62**, 13153 (2000)

[14] I.Bozović, N.Bozović, M.Damnjanović, Phys. Rev.B **62,** 6971 (2000)

[15] A.Grűnesis, R.Saito, G.G.Samsonidze, T.Kimura, M.A.Pimenta, A.Jorio, A.G.Souza Filho, G.Dresselhaus, M.S.Dresselhaus Phys.Rev B **67,** 13153 (2003)

[16] A.Jorio, G.Dresselhaus, M.S.Dresselhaus, M.Souza, M.S.S.Dantas, M.A.Pimenta, A.M.Rao, R.Saito, C.Liu and H.M.Cheng, Phys.Rev.Lett. **85,** 2617-2620 (2000)

[17] R.Saito, A.Jorio, J.H.Hafner, C.M.Lieber, M.Hunter, T.McClure, G.Dresselhaus, M.S.Dresselhaus Phys. Rev. B. **64,** 085312 (2001)

[18] A.Jorio, A.G.Souza Filho, G.Dresselhaus, M.S.Dresselhaus, A.K.Swan, M.S.Űnlű, B.B.Goldberg, M.A.Pimenta, J.H.Hafner, C.M.Lieber, R.Saito, Phys. Rev. B. **65,** 155412 (2002)

[19] A.Jorio, M.A.Pimenta, A.G.Souza Filho, G.G.Samsonidze, A.K.Swan, M.S.Űnlű, B.B.Goldberg, R.Saito, G.Dresselhaus, M.S.Dresselhaus, Phys. Rev. Lett. **90,** 107403 (2003)

[20] A.Jorio C.Fantini, M.S.S.Dantas, M.A.Pimenta, A.G.Souza Filho, G.G.Samsonidze, V.W.Brar, G. Dresselhaus, M.S.Dresselhaus, A.K.Swan, M.S.Űnlű, B.B.Goldberg, R.Saito, Phys.Rev.B **66,** 115411 (2002)

[21] M.S.Dresselhaus, G.Dresselhaus Adv.Phys.(a) **30,** 139-326 1981 (b) **50,** 1-186 (2002)

[22] T.Enoki, M.Endo, M.Suzuki Graphite Intercalation Compounds and Applications, Oxford University Press, New York 2003

[23] A.Kasuya, Y.Sasaki, I.Saito, K.Tohji, Y.Nishina Phys. Rev Letters **78,** 4434(1997)

[24] S.D.M.Brown, A.Jorio, P.Corio, M.S.Dresselhaus, G.Dresselhaus, R.Saito, K.Kneipp, Phys.Rev.B-Rapid Comm (2001)

[25] S.D.M.Brown, A.Jorio, P.Corio, M.S.Dresselhaus, G.Dresselhaus, R.Saito, K.Kneipp, Phys.Rev.B, **63**, 155414 (2001)

[26] M.Lazzeri, S.Piscanec, F.Mauri, A.C.Ferrari and J.Robertson Phys. Rev. B **73,** 155426 (2006)

[27] C.Jiang, K.Kempa, J.Zhao, U.Schlecht, U.Kolb, T.Basché, M.Burghard and A.Mews Phys. Rev. B, **66**, 161404 (2002)

[28] M.Paillet, P.Poncharai, A.Zahab, J.L.Sauvajol Phys. Rev. Lett. **95,** 237401 (2005)

[29] S.D.M.Brown, A.Jorio, M.S.Dresselhaus, G.Dresselhaus, Phys.Rev.B, **64**, 073403 (2001)

[30] M.A.Pimenta, E.B.Hanlon A.Marucci, P.Corio, S.D.M.Browne, S.A.Empedocles, M.G.Bawendi, G.Dresselhaus, M.S.Dresselhaus, Brazilian J.Phys.**30,** 423 (2000)

[31] I.Pócski, M.Hundhausen, M.Koós, L.Ley J. Non-Cryst.Solids **1083,** 227-230 (1998)

[32] M.J.Matthews, M.A.Pimenta, G.Dresselhaus, M.S.Dresselhaus, M.Endo Phys.Rev.B, **59,** R6585, (1999)

[33] M.S.Dresselhaus, G.Dresselhaus, A.Jorio, A.G.Souza Filho, R.Saito, Carbon **40,** 2043 (2002)

[34] M.A.Pimenta A.Jorio, S.D.M.Browne, R.Saito, .A.G.Souza Filho, G.Dresselhaus J.H.Hafner, C.M.Lieber, R.Saito, M.S.Dresselhaus Phys. Rev. B **64,** 041401(R) (2001)

[35] A.G.Souza Filho, A.Jorio, G.G.Samsonidze, G. Dresselhaus, M.A.Pimenta, M.S.Dresselhaus, A.K.Swan, M.S.Űnlű, B.B.Goldberg, R.Saito Phys.Rev B **67,** 35427 (2003)

[36] J.F.Cardenas Chem.Phys.Lett. **430,** 367-369 (2006)

[37] A.C.Ferrari, J.Roberston Phys.Rev.B **64,** 075414 (2001)

[38] A.C.Ferrari, J.Roberston Phys.Rev.B **61,** 14095 (2000)

[39] S.D.M.Brown, P.Corio, A.Marucci, M.S.Dresselhaus Phys.Rev.B **61,** 8 R5137 (2000)

[40] J.Kűrti, V.Zólyomi, Grűneis, H.Kuzmany, Phys.Rev.B **65,** 165433 (2002)

[41] R.Saito, A.Jorio, A.G.Souza Filho, G.Dresselhaus, M.S.Dresselhaus, M.A.Pimenta Phys.Rev.Lett. **88,** 027401 (2002)

[42] A.G.Souza Filho, A.Jorio, G.G.Samsonidze, G.Dresselhaus, M.S.Dresselhaus A.K.Swan, M.S.Űnlű, B.B.Goldberg, R.Saito, J.H.Hafner, C.M.Lieber, M.A.Pimenta, Chem. Phys. Lett.. **354,** 62-68 (2002)

[43] A.G.Souza Filho, A.Jorio, A.K.Swan, M.S.Űnlű, B.B.Goldberg, R.Saito, J.H.Hafner, C.M.Lieber, M.A.Pimenta, G.Dresselhaus, M.S.Dresselhaus Phys. Rev. B. **65,** 085417 (2002)

[44] G.G.Samsonidze, R.Saito, A.Jorio, A.G.Souza Filho, A.Grűneis, M.A.Pimento, G.Dresselhaus, M.S.Dresselhaus, Phys.Rev. Lett. **90,** 027403 (2003)

[45] M.Milnera, J.Kűrti, M.Hulman, H.Kuzmany, Phys.Rev. Lett. **84,** 1324 (2000)

[46] A.Jorio, R.Saito, J.H.Hafner, C.M.Lieber, M.Hunter, T.McClure, G.Dresselhaus, M.S.Dresselhaus, Phys.Rev.Lett. **86,** 1118 (2001)

[47] J.Kűrti, V.Zólyomi, M.Kertesz, G.Sun New J. Phys **5,** 125 (2003)

[48] S. Reich, J. Maultzsch, C. Thomsen, P. Ordejon Phys. Rev. B **66**, 035412 (2002)

[49] Y.F.Wang, X.W.Cao, S.F.Hu, Y.Y.Liu, G.X.Lan Chem.Phys.Lett **336**, 47-52 (2001)

[50] C.Fantini, A.Jorio, M.Souza, M.S.Strano, M.S.Dresselhaus, M.A.Pimenta Phys.Rev.Lett **93,** 147406 (2004)

[51] G.G.Samsonidze, S.G.Chou, A.P.Santos, V.A. Brar, G.Dresselhaus, M.S.Dresselhaus, A.Selbst A.K.Swan, M.S.Űnlű, B.B.Goldberg, D.Chattopadhyay, S.N.Kim, F.Papadimitrakopoulos Appl.Phys. Lett. **85,** 1006-1008 (2004)

[52] U.D.Venkateswaran, A.M.Rao, E.Richter, M.Menon, A.Rinzler, R.E.Smalley, P.C.Eklund Phys.Rev.B **59,** 16 10928 (1999)

[53] A.M.Rao, J.Chen, E.Richter, U.Schlecht, P.C.Eklund, R.C.Haddon, U.D.Venkateswaran, Y.K.Kwon, D.Tománek, Phys.Rev. Lett. **86,** 17 (2001)

[54] P.H.Tan, C.Y.Hu, F.Li, S.Bai, P.X.Hou, H.M.Cheng, Carbon **40,** 1131-1150 (2002)

[55] P.H.Tan, Y.Tang, C.Y. Hu, F.Li, Y.L.Wei, H.M.Cheng Phys. Rev. B. **62,** 5186 (2000)

[56] P.V.Huong, R.Cavagnat, P.M.Ajayan, O.Stephen, Phys. Rev. B **51,** 10048-51 (1995)

[57] H.Herchen and M.A.Cappelli Phys. Rev. B **43,** 1 (1991)

[58] M.Balkanski, R.F.Wallis and E.Haro Phys. Rev. B **28,** 1928 (1983)

[59] F.Huang, K.T.Yue, P.Tan, S.L.Zhang, Z.Shi, X.Zhou, Z.Gu, J.Appl.Phys. **84,** 4022-4

[60] H.D.Li, K.T.Yue, Z.L.Lian, L.X.Zhou, S.L.Zhang, Z.J.Shi, Z.N.Gu, B.B.Liu, R.S.Yang, H.B.Yang, G.T.Zou, Y.Zhang, S Iijima Appl. Phys.Lett .**76,** 2053-5 (2000)

[61] N.R.Raravikar, P.Keblinski, A.M.Rao, M.S.Dresselhaus, L.S.Schadler, P.M.Ajayan, Phys.Rev. B **66,** 235424 (2002)

[62] L.Ci, Z.Zhou, S.Li, X.Yan, D.Liu, H.Yan, Y.Gao, J.Wang, L.Liu, w.Zhou, G.Wang, S.Xie Appl.Phys.Lett **82,** 3098-100 (2003)

[63] Q.Zhang, D.J.Yang, S.G.Wang, S.F.Yoon, J.Ahn Smart Materials and Structures **15,** S1-S4 (2006)

[64] S.B.Cronin, Y.Yin, A.Walsh, B.Capaz, A.Stolyarov, P.Tangney, M.L.Cohen, S.G.Louie, A.K.Swan, M.S.Űnlű, B.B.Goldberg, M.Tinkham Phys.Rev.Lett **96,** 127403 (2006)

CHAPTER 4

RAMAN SPECTROSCOPY OF SINGLE WALLED CARBON NANOTUBE BUNDLES

4.1 Introduction

From the outset, Raman spectroscopy has been recognised as a very useful tool in the study of carbon nanotubes. The details of the characteristic Raman spectrum have been outlined and discussed in chapter 3. Here in chapter 4, a detailed study of the Raman spectra of two different nanotube samples taken at room temperature is discussed. In both samples the as prepared tubes, according to the manufacturers and as characterised by TEM and AFM, are in the bundled state[1][2][3][4].

It is important to characterise bundles since this is the state in which SWNT are produced and understanding their properties is the starting point in understanding the behaviour of isolated tubes. Bundles show the characteristic spectrum of isolated nanotubes, figure 4.1.

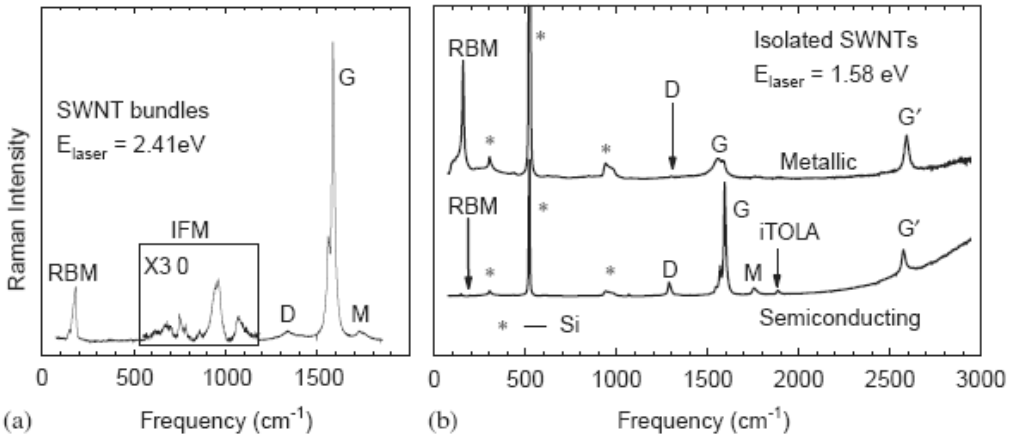

FIGURE 4.1: Raman spectrum taken for (a) bundles (b) isolated tubes[5]

However as previously discussed in chapter 3, bundling interactions minimally perturb the vibrational characteristics of the nanotubes leading to inhomogeneous broadening of the Raman spectra due to the presence of many tubes with differing chiral structures. This can be seen as broadening of $\Delta\omega_G$,

increased full width half max (FWHM) of the D and G* lineshapes, larger G-line resolved linewidths, the presence of Breit-Wigner-Fano lineshape of metallic spectra and contraction of the RBM spectrum.

The first sample was HiPco tubes purchased from Carbon Nanotechnologies Incorporated, batch number P0288. The diameter range of HiPco tubes has been shown to be 0.8 nm -1.2 nm[6][7]. The second sample was arc-discharge tubes purchased from Sigma-Aldrich, batch number 05224EC. According to the manufacturer's accompanying literature, the diameter range of these tubes was 1.2 nm to 1.6 nm[1]. It has previously been shown[8], using AFM, that the bundle size for both the HiPco and arc discharge as produced tubes dispersed in toluene was approximately 30 nm diameter. This chapter analyses Raman spectra taken from the two samples. The material is examined as supplied and in later chapters these spectra will be compared to spectra taken from debundled samples.

4.2 Experimental

Raman measurements were taken using an Instruments S.A. (Jobin Yvon) Labram 1B shown in figure 4.2. The Labram system is a confocal Raman imaging microscope system. Both a Helium-Neon laser (633 nm) and an external Argon ion (514.5 nm and 488 nm) laser were used as sources. Both lasers are polarised. The light is imaged to a diffraction limited spot (typically 1 μm) via the objective of an Olympus BX40 microscope. The scattered light is collected by the objective in a backscattering geometry and is dispersed onto a

Peltier cooled CCD array by one of two interchangeable gratings, 600 lines/mm or 1800 lines/nm, allowing a range of 150 cm^{-1} to 4000 cm^{-1} to be covered in a single image, or with greater resolution in a combination of images. With the latter, a spectral dispersion of ~1 cm^{-1} per pixel is achievable. The confocal, microscopic system allows measurement of powdered samples with no further sample preparation. Spectral X-Y mapping may be performed with a precision of 0.1 μm, although the laser spot size is of the order of 1 μm diameter.

FIGURE 4.2: Instruments S.A. (Jobin Yvon) Labram 1B Raman Spectrometer

Raw powder of each of the samples was placed on a glass side which had previously been cleaned with ethanol and acetone. The powder was spread smoothly over the slide. A series of Stokes/anti-Stokes Raman spectra were taken at different points along the slides. Although there was some point to point variation there was a consistency in the spectral shape and frequencies. Multipoint averages, typically ten, were taken of both spectral frequencies and intensity ratios. This study was carried out at three excitation wavelengths – 488 nm (2.5 eV), 514.5 nm (2.4 eV) and 633 nm (1.92 eV).

4.3. Results - Room Temperature Raman of HiPco Samples

Each of the characteristic parts of the Raman Spectra as discussed in 3.4 were analysed separately. A typical metallic and semiconductor spectrum can be found in figure 3.2.

Figure 4.3 shows the Stokes G-line for the HiPco nanotube samples.

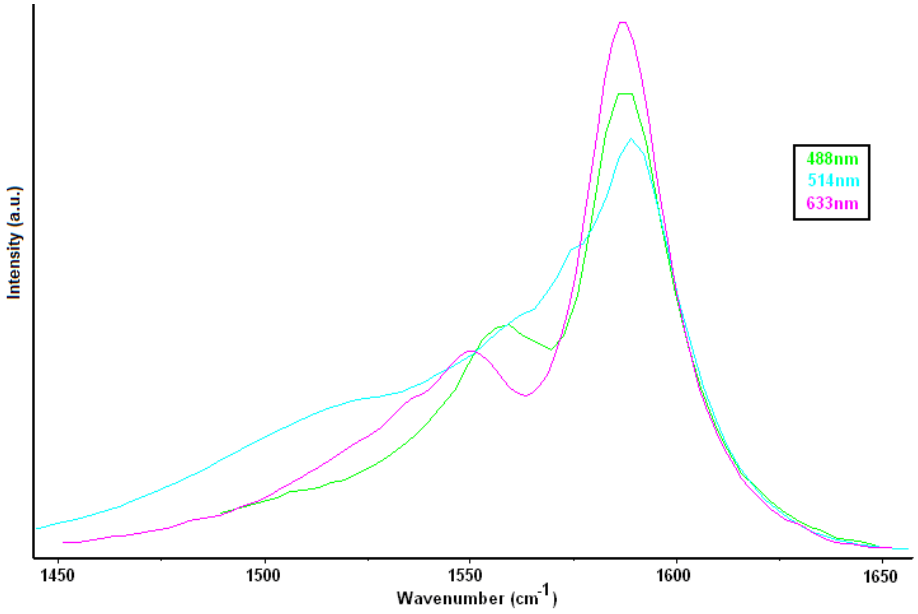

FIGURE 4.3: Stokes Raman G-line for HiPco Samples

The G-line for the HiPco samples is clearly semiconducting, (Lorentzian), in nature when using 488 nm and 633 nm are used as sources. The G^+ position is 1586 cm^{-1} for both spectra confirms the expected excitation independence as mentioned in chapter 3. The G^- is however different, being positioned at 1557 cm^{-1} for 488 nm and 1549 cm^{-1} for 633 nm, indicative of the different tubes resonant at these excitations as expected from the Kataura plot[9], figure 3.5. $\Delta\omega_G$ is 29 cm^{-1} for 488 nm and 39 cm^{-1} for 633 nm. At 514.5 nm there is a metallic character to the spectrum indicated by the broader Breit-Wigner-Fano line shape of the G^- feature. The G^+ position has upshifted by 3 cm^{-1} to 1589 cm^-

[1]. The 488 nm and 633 nm G-lines were fitted with 3 Lorentzian line shapes and the 514 nm G-line with 2 Lorentzian and 1 Briet-Wigner-Fano line shapes. The FWHM of the fitted G-line peaks is shown in table 4.1 below.

LASER LINE	Peak 1	Peak 2	Peak 3
488 nm	40.42 cm^{-1}	25.29 cm^{-1}	23.97 cm^{-1}
514.5 nm	62.92 cm^{-1}	40.25 cm^{-1}	23.02 cm^{-1}
633 nm	40.24 cm^{-1}	21.98 cm^{-1}	22.21 cm^{-1}

TABLE 4.1: Summary of fitted G-line peaks for raw HiPco samples. Peak 1- 514.5 nm is Breit-Wigner-Fano lineshape

According to Browne et al[10], resonance of metallic nanotubes occurs for $E_{Laser} = E_{11}^{M} - E_{ph}$ in the anti-Stokes and $E_{Laser} = E_{11}^{M} + E_{ph}$ in the Stokes spectrum where E_{ph} is the phonon energy for the tangential band and has a value of 0.2eV. Using equation 2.11, the laser lines at which Raman scattering is resonant for metallic tubes can be determined. Within the diameter range of 0.8nm to 1.6nm there are a total of 37 metallic tubes. The laser lines at which resonance occurs for these tubes can be found in appendix 1. For HiPco tubes with diameters in the range 0.8 nm to 1.2 nm, metallic tubes are predicted to be resonant at 514.5 nm (1.4 eV) in the Stokes and anti-Stokes spectrum and in the anti-Stokes at 633 nm (1.92 eV).

The anti-Stokes G-lines for the HiPco powder are shown in figure 4.4.

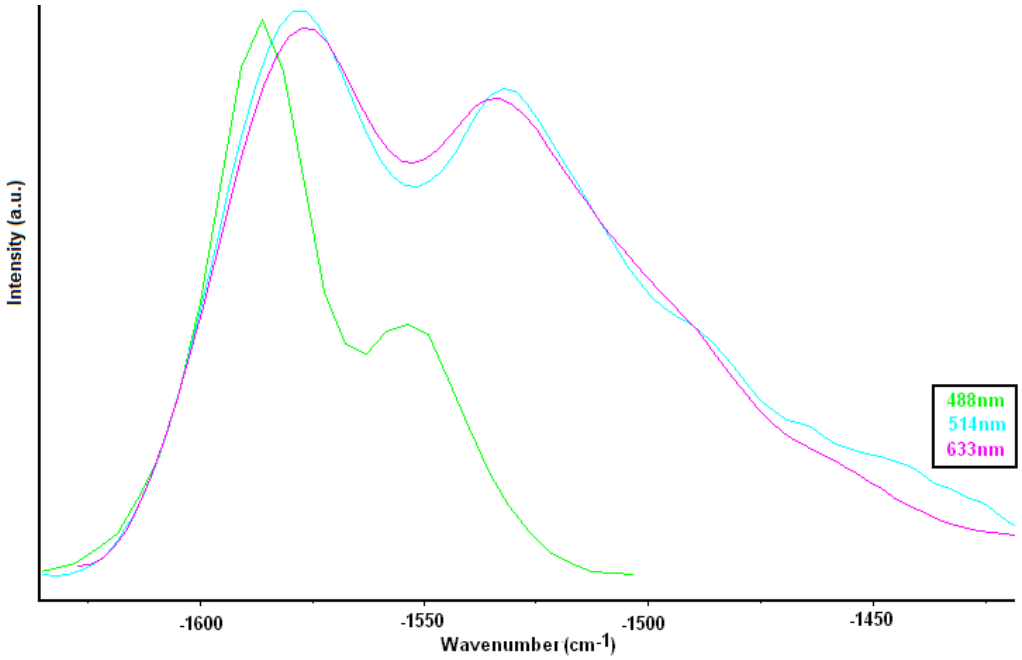

FIGURE 4.4: Anti-Stokes Raman G-line for HiPco tubes

The first thing to note is that the anti-Stokes at 633 nm (1.92 eV) is metallic in character whereas the corresponding Stokes line is semiconducting. The 514.5 nm spectrum also shows a lineshape characteristic of a metallic resonance in the anti-Stokes spectrum. Both can be predicted from appendix 1. For the semiconducting 488 nm anti-Stokes spectrum, $\Delta\omega_G$ is 32 cm^{-1} compared with 29 cm^{-1} in the Stokes. Using equation 3.16, the mean diameter of resonant tubes in both spectra is calculated. This turns out to be 1.18 nm for the anti-Stokes spectrum and 1.28 nm for the Stokes spectrum. This is indicative of the fact that although both spectra appear semiconducting, different tubes are in resonance in each spectrum.

The D-line spectra are shown in figure 4.5. There is an upshift of wavenumber with increasing laser energy of ~50 cm^{-1}/eV. It should be noted that unlike the G-line and G*-line, there was a notable variation in D-line intensity values taken

at different points along the slide. One explanation for this could be that since the nanotube powder was untreated, it still contained some impurities and amorphous carbon, the amounts of which differed from point to point along the slide. Large D-line values result from such impurities, as described in section 3.4.2.

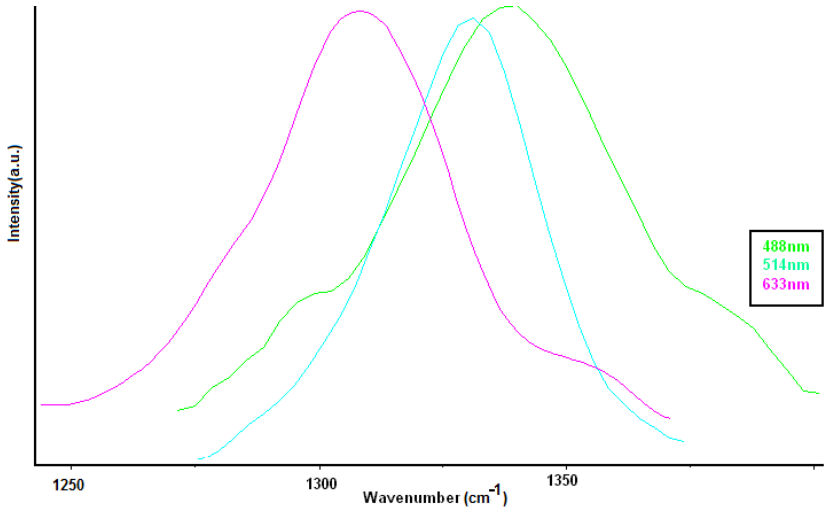

FIGURE 4.5: Stokes D-line for HiPco tubes

When the G* spectra, shown in figure 4.6 are examined, again there is an upshift of wavenumber with laser energy, of 109 cm^{-1}/eV.

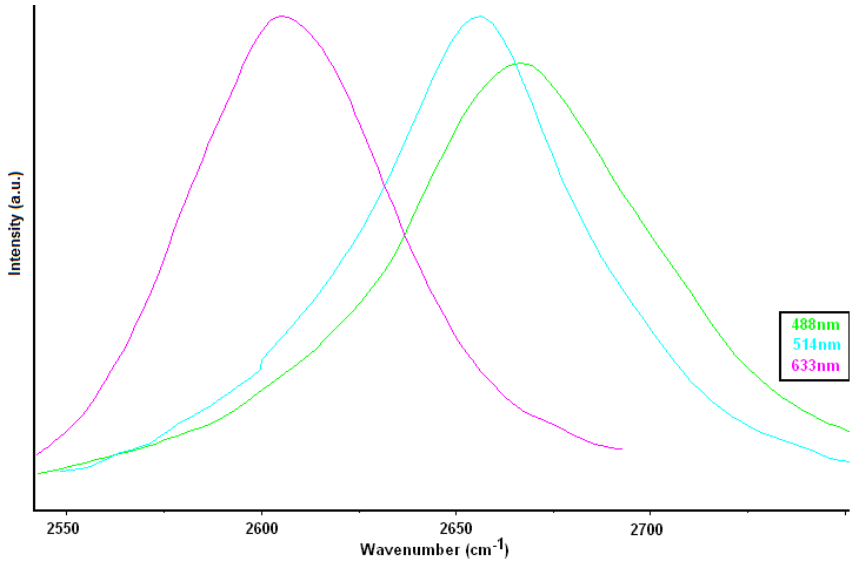

FIGURE 4.6: Stokes G*-line for HiPco tubes

The positions and the full width half maximum (FWHM) of the characteristic Stokes lines of raw HiPco tubes for each laser line are shown in table 4.2.

LASER LINE	D-Line cm^{-1}	FWHM D-Line cm^{-1}	G^+-Line cm^{-1}	G^-- Line cm^{-1}	$\Delta\omega_G$ cm^{-1}	G*-Line cm^{-1}	FWHM G^*-Line cm^{-1}
488 nm	1336	48	1586	1557	29	2666	76
514.5 nm	1331	30	1589	-	-	2656	62
633 nm	1308	45	1586	1549	39	2605	60

TABLE 4.2: Summary of characteristic lines for raw HiPco samples

The ratios of the relative intensities of some of the characteristic lines in the Stokes Raman spectra were calculated and are shown in table 4.3.

LASER LINE	G^+/G^-	G^+/G^*	G^-/G^*	G^+/D	G^-/D	G^*/D
488 nm	2.02±0.2	4.53±0.4	2.26±0.2	24.00±3.0	11.93±2.0	5.26±1.3
514.5 nm	2.82±0.2	1.97±0.5	0.7±0.2	17.39±4.0	6.17±1.5	9.16±1.2
633 nm	2.7±0.3	5.59±0.5	2.06±0.15	18.84±4.0	6.97±2.0	3.38±1.2

TABLE 4.3: Intensities ratios for HiPco sample spectra. Red indicates metallic spectra

The main thing to note at this stage is the effect of a large G*-line in the metallic 514.5 nm spectrum. In the metallic-like spectra, any of the ratios involving G* are very different from the non metallic 488 nm and 633 nm spectra. Although not commonly used as a characteristic parameter, it is apparent that G^+/G^* or G^-/G^* could be used as an indicator of metallicity in bundles.

The Stokes and anti-Stokes RBMs for each laser line are shown in figure 4.7. The first thing to note is that the RBMs are different for each wavelength in the Stokes and the anti-Stokes. This of course arises from the fact that different tubes are resonant in each region. Also it can be seen that as expected different tubes are resonant for each different excitation energy.

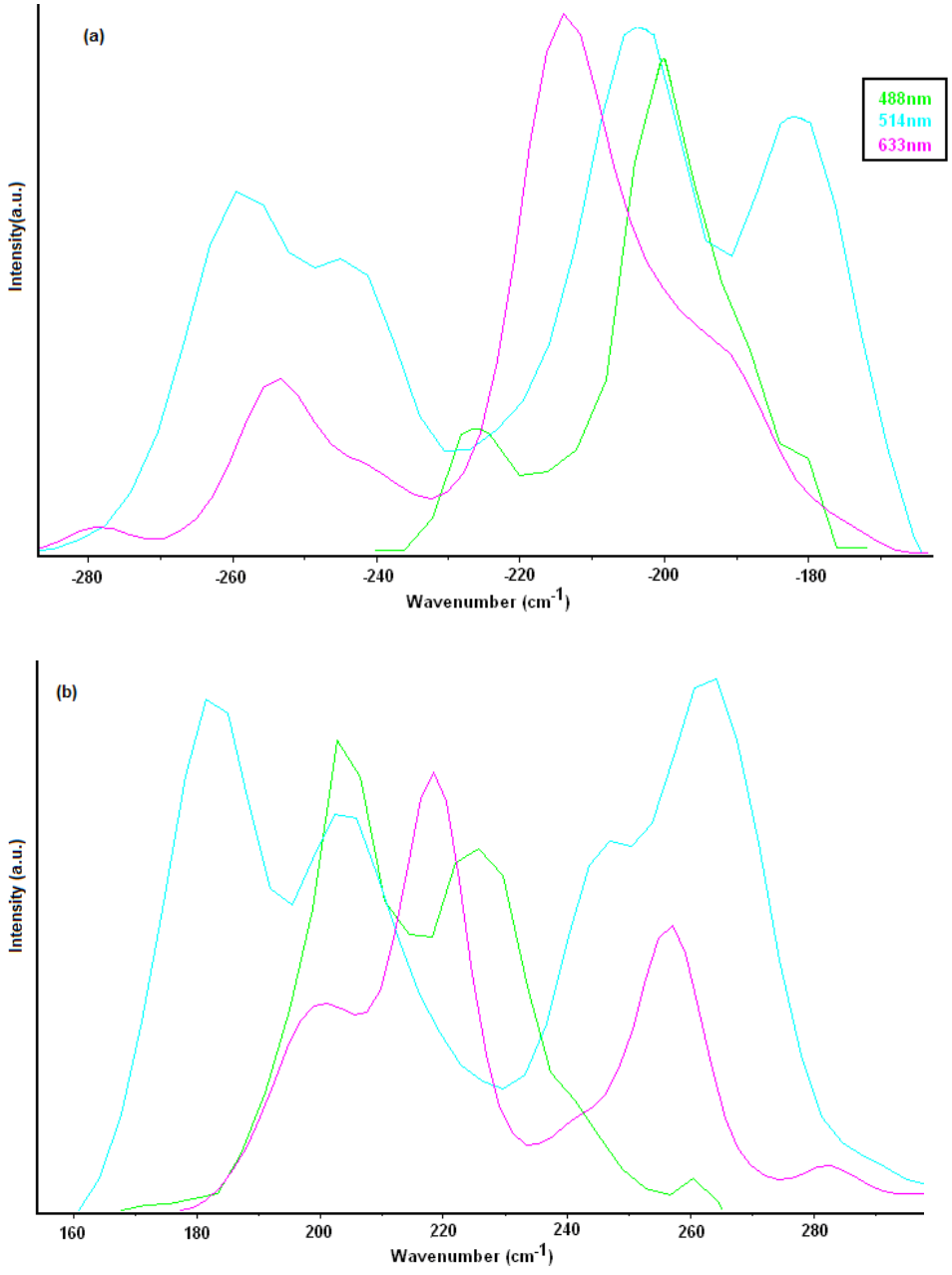

FIGURE 4.7: RBMs anti-Stokes(a) and Stokes (b) for HiPco tubes

Each RBM spectrum was fitted with a Lorentzian band. An example of the fitted Stokes 633 nm spectrum is shown in figure 4.8.

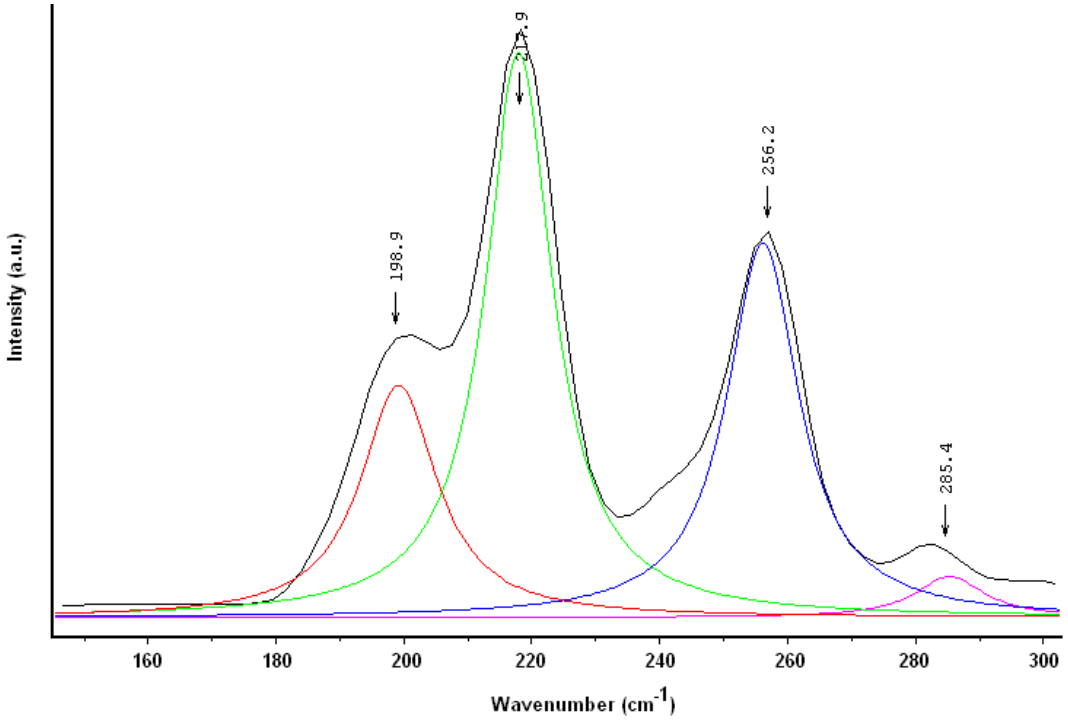

FIGURE 4.8: Fitted Stokes 633nm RBM spectrum for HiPco tubes

Using equation 3.14, which describes the relationship between RBM frequency and diameter for bundles and equation 2.2 which relates diameter to the chiral indices, the fitted peaks were assigned and the results are shown in table 4.4. Only tubes resonant according to the Kataura plot were considered as it is expected that these will dominate.

Metallic signatures are evident only in the 514.5 nm Stokes and anti-Stokes and 633 nm anti-Stokes spectra. This correlates well with the fact that a metallic G -line was found in the Stokes spectrum at 514.5 nm and in the anti-Stokes spectra at 514.5 nm and 633 nm. Most of these metallic tubes are slightly off

resonance. The (15,0) however is in resonance in the anti-Stokes at 633 nm, see appendix 1.

LASER LINE	STOKES	ANTI-STOKES
488 nm	203.6 cm^{-1}-1.21nm(15,1)(11,9)	-190.5 cm^{-1}-1.30nm(12,7)
	222.7 cm^{-1}-1.10nm(14,0)(10,6)(13,2)	-200.7 cm^{-1}-1.23nm(14,3)(11,7)
	225.4 cm^{-1}-1.09nm(9,7)	-226.4 cm^{-1}-1.08nm(9,7)
	242.7 cm^{-1}-1.01nm(13,0)(8,7)	
514.5 nm	181.8 cm^{-1}-1.36nm (10,10)*	-181.4cm^{-1}=1.37nm(12,8)(17,1)
	204.1 cm^{-1}-1.21nm(13,4)*	-204.4cm^{-1}=1.21nm(13,4)*
	245.6 cm^{-1}-0.98nm(10,4)*	-244.2cm^{-1}=1.00nm(11.3)
	263.4 cm^{-1}-0.90nm(10,3)	-259.4cm^{-1}=0.94nm(12,0)*
633 nm	198.9cm^{-1} – 1.23nm(14,3)	-193.6cm^{-1}-1.28nm(10,9)
	217.9 cm^{-1}-1.13nm(12,4)	-209.2cm^{-1}-1.18nm(15,0)**
	256.2 cm^{-1}-0.95nm(8,6)	-216.1cm^{-1}-1.14nm(14,1)
	285.4cm^{-1}-0.87nm(10,2)	-257.4cm^{-1}-0.95nm(8,6)(11,2)
		-280.1cm^{-1}- 0.87nm (10,2)

TABLE 4.4: Fitted Stokes and anti-Stokes peaks from 514.5 nm and 633 nm spectra for HiPco tubes with corresponding tube diameters and assignments. Asterix indicates metallic tubes.

In summary, for HiPco samples, examination of the G-line shows the presence of both semiconducting (488 nm and 633 nm) and metallic (514.5 nm) tubes. Different tubes are resonant in the Stokes and anti-Stokes spectra at a given excitation energy. This is seen in both the G-line and the RBMs. The mean diameter of resonant tubes varies for different excitation energies. The shift in the D-line and G*-line is 50 cm^{-1}/eV and 109 cm^{-1}/eV respectively. The ratios of the intensity of the characteristic lines are similar when the spectra are semiconducting in nature but quite different when the spectrum is metallic. The typical bundled induced Briet-Wigner Fano metallic peak is seen in the G-line at

514.5 nm. FWHM values of fitted G-line peaks, D and G* lines are typical for bundles[11][12][13].

4.4 Results - Room Temperature Raman of Arc-Discharge Samples

Looking at the metallic tube resonances, appendix 1, for the diameter range of arc discharge nanotube samples, 1.2 nm to 1.6 nm, the metallic tubes are only resonant at 633 nm in the Stokes spectrum. Figure 4.9 shows the Stokes G-line for the arc-discharge tubes.

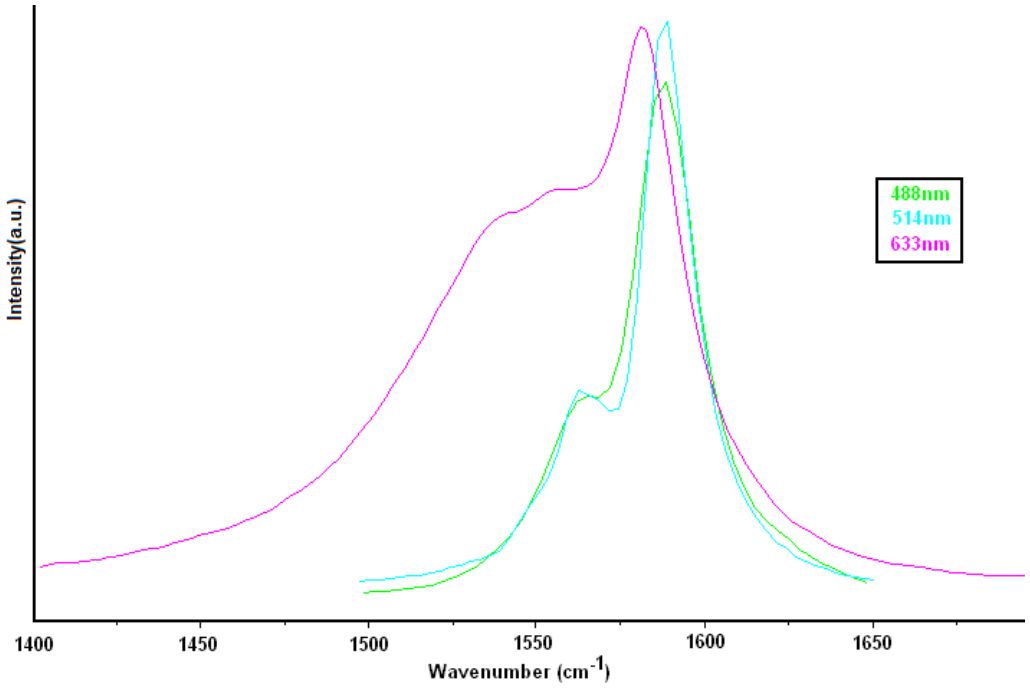

FIGURE 4.9: Stokes Raman G-line for arc-discharge samples

The profile of the spectrum of the arc-discharge samples is semiconducting in nature at 488 nm and 514.5 nm as expected. The G^+ position is 1589 cm^{-1} for both spectra confirming the expected excitation independence as mentioned in chapter 3. The G^- again is different, being situated at 1565 cm^{-1} for 488 nm and 1556 cm^{-1} for 514.5 nm, giving a $\Delta\omega_G$ value of 24 cm^{-1} at 488 nm and 33 cm^{-1} at

514.5 nm indicating that different tubes are resonant in each spectra as expected. At 633 nm there is a strong metallic influence in the spectra, as expected. The G^+ position this time has downshifted by 7 cm^{-1} to 1582 cm^{-1}. The G^- feature has a Breit-Wigner-Fano line shape spanning a wide wavenumber region. Figure 4.10 shows the anti-Stokes G line whereby all spectra appear semiconducting.

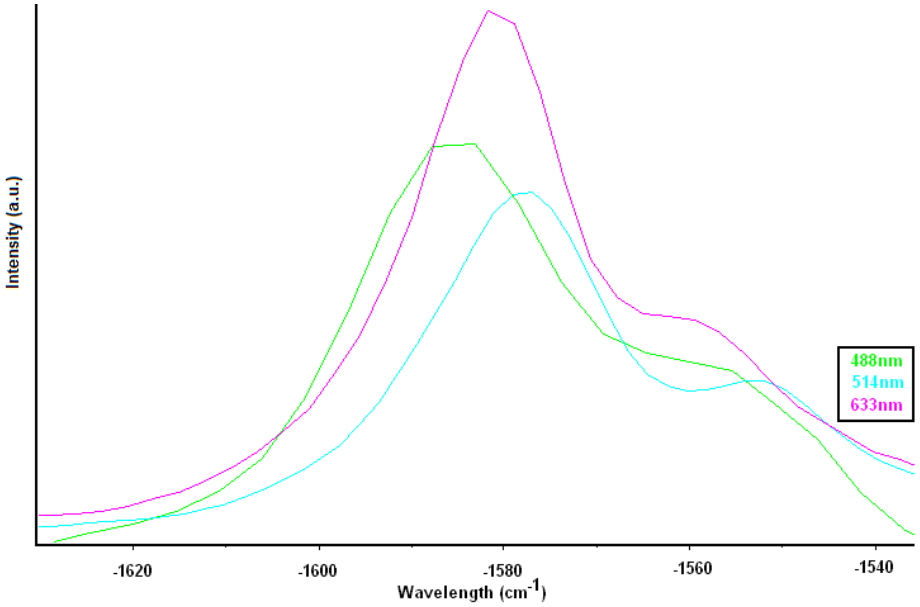

FIGURE 4.10:Anti-Stokes Raman G-line for arc-discharge samples

The 488 nm and 514.5 nm G-lines were fitted with 3 Lorentzian linshapes and the 633 nm G-line with 2 Lorentzian lineshapes and 1 Breit-Wigner-Fano lineshape. The FWHM of the fitted G-line peaks is shown in table 4.5 below.

LASER LINE	Peak 1	Peak 2	Peak 3
488 nm	13.48	11.67	23.23
514 nm	13.14	12.88	22.83
633 nm	58.27	36.38	24.83

TABLE 4.5: Summary of fitted G-line peaks for raw arc-discharge samples. Peak 1- 633 nm is Breit-Wigner-Fano lineshape

The D-line of the Stokes spectrum can be seen in figure 4.11. There is an upshift of wavenumber with increasing laser energy of 55 $cm^{-1}eV$.

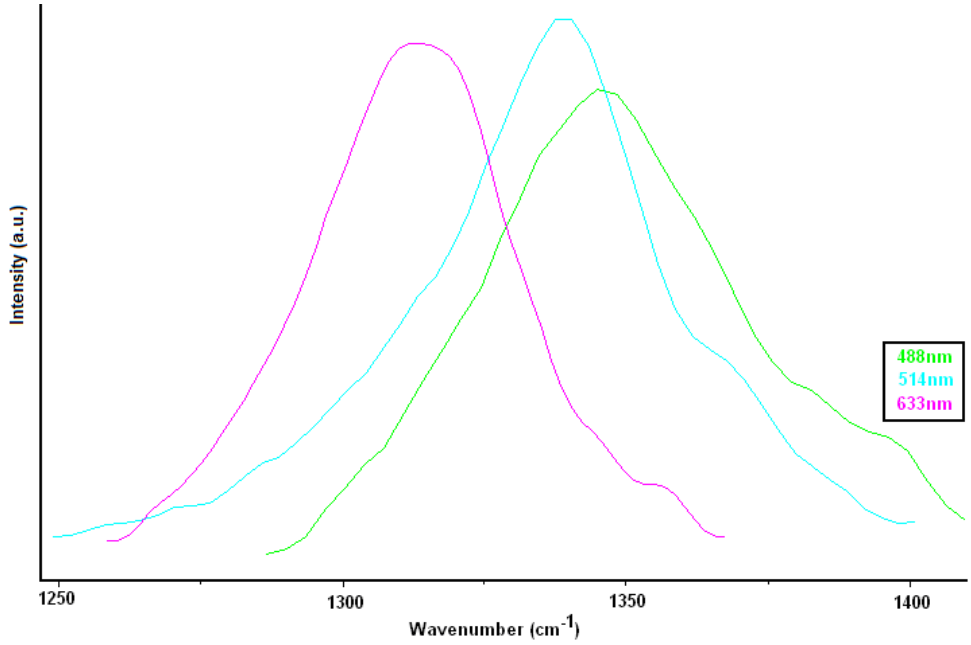

FIGURE 4.11: Stokes Raman D-line for arc-discharge samples

When the G* spectra, shown in figure 4.12, are examined, it can be seen that again there is an upshift of wavenumber with laser energy of 117 cm^{-1}/eV.

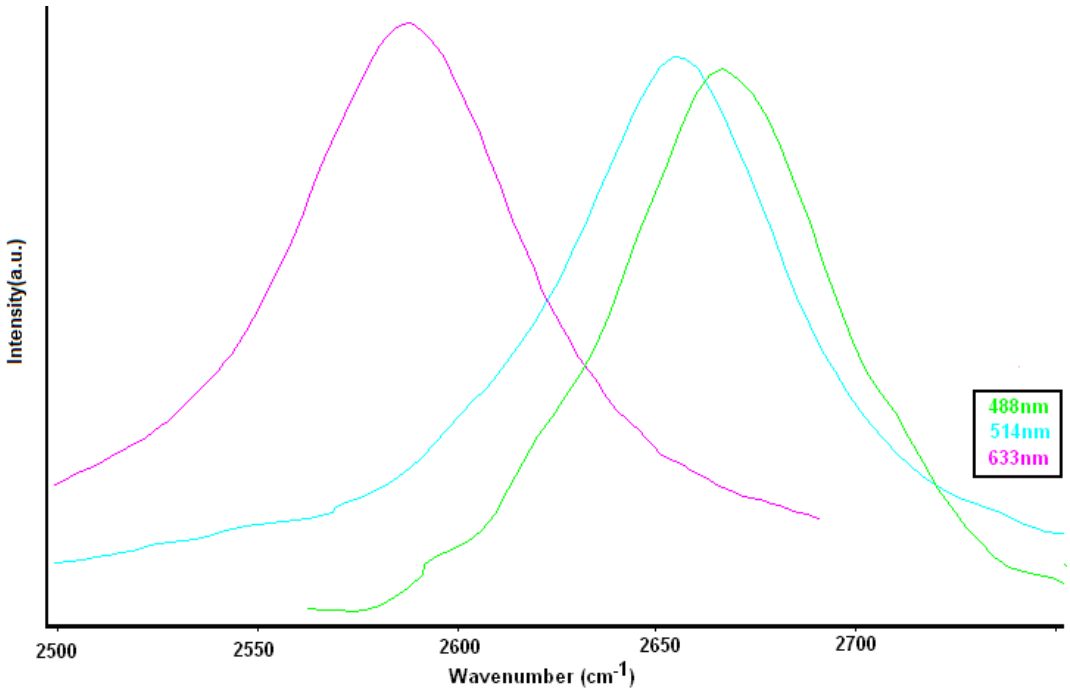

FIGURE 4.12: Stokes Raman G*-line for arc-discharge samples

The positions of the characteristic Stokes lines of raw arc discharge tubes for each laser line are shown in table 4.6.

LASER LINE	D-Line cm^{-1}	FWHM D-Line cm^{-1}	G^+-Line cm^{-1}	G^-- Line cm^{-1}	$\Delta\omega_G$ cm^{-1}	G*-Line cm^{-1}	FWHM G^*-Line cm^{-1}
488 nm	1336	45	1588	1565	23	2680	58
514.5 nm	1331	43	1589	1556	33	2671	55
633 nm	1307	36	1582	-	-	2615	54

TABLE 4.6: Summary of characteristic lines for raw arc-discharge samples

The ratios of the relative intensities of the characteristic lines in the Raman spectra were calculated and are shown in table 4.7 below.

LASER LINE	G^+/G^-	G^+/G^*	G^-/G^*	G^+/D	G^-/D	G^*/D
488 nm	2.65±0.15	5.76±0.35	2.17±0.15	17.81±2.5	6.72±2.5	3.09±1.5
514.5 nm	3.00±0.2	8.24±1.0	2.75±0.5	20.27±2.5	6.76±1.5	2.46±1.5
633 nm	1.43±0.5	2.45±0.5	1.71±0.20	24.92±6.0	17.37±2.5	10.17±1.5

TABLE 4.7: Intensities ratios for arc discharge sample spectra. Red indicates metallic spectra

As in the case of the HiPco tubes, the principal observation here is the effect of a large G*-line in the metallic 633 nm spectrum. These ratios are very different in all cases from the non metallic 488 nm and 514.5 nm spectra.

The Stokes and anti-Stokes RBMs are shown in figure 4.13. The first thing to note is that the RBMs are different for each wavelength in the Stokes and the anti-Stokes. This of course arises from the fact that different tubes are resonant in each. Table 4.8 shows the fitted RBMs for the Stokes and anti-Stokes

spectra. It can be seen that it is only in the Stokes spectrum at 633 nm that any metallic tubes are found. The characteristics of the G line spectra in figures 4.9 and 4.10 confirms this.

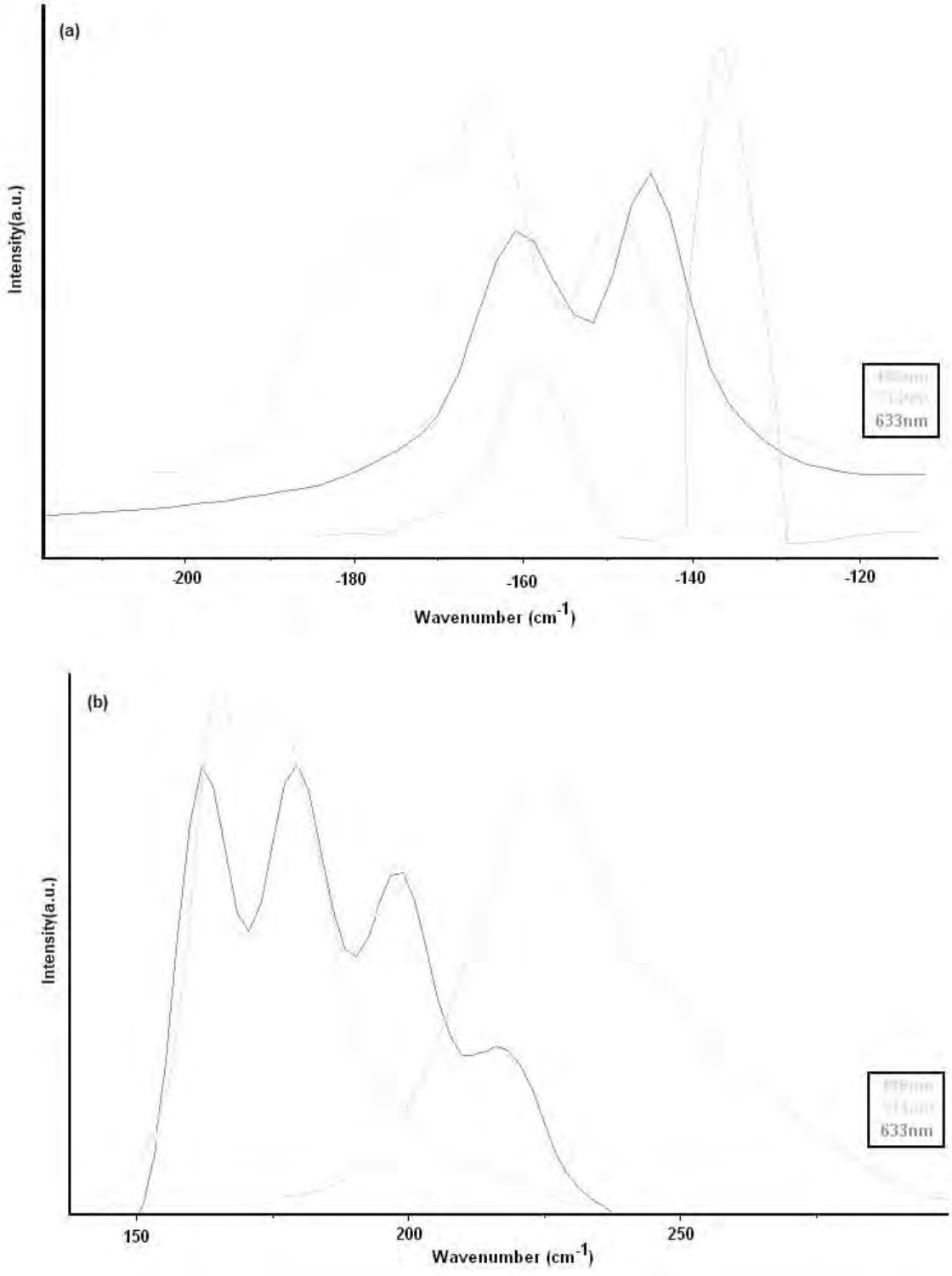

FIGURE 4.13: RBMs (a) anti-Stokes above and (b)Stokes below for arc-discharge samples

LASER LINE	STOKES	ANTI-STOKES
514.5 nm	155.8 cm^{-1}-1.60 nm (20,1)	-148.3 cm^{-1}=1.69 nm(20,3)
	162.2 cm^{-1}-1.53 nm(7,15)	-166.2 cm^{-1}=1.50 nm(13,9)
	168.0 cm^{-1}-1.48 nm(16,5)	-179.4 cm^{-1}=1.38 nm(8,13)
	178.5 cm^{-1}-1.39 nm(16,3)	-183.2 cm^{-1}=1.35 nm(16,2)
633 nm	161.1 cm^{-1} – 1.56 nm(12,11)	-161.1 cm^{-1}-1.56 nm(12,11)
	179.5 cm^{-1}-1.38 nm(16,3)	-144.6 cm^{-1}-1.18 nm(15,1)
	198.6 cm^{-1}-1.24 nm(12,6)*	
	219.1 cm^{-1}-1.12 nm(12,4)	
	237.3 cm^{-1}-1.02 nm(9,6)*	

TABLE 4.8: Fitted Stokes and anti-Stokes peaks from 514.5 nm and 633 nm spectra for arc discharge samples with corresponding tube diameters. Asterix indicates metallic tubes.

Interesting behaviour is seen in the 633 nm spectra where the anti-Stokes RBMs are much more intense than the Stokes, as shown in figure 4.14. The anti-Stokes G-line is also significantly more intense than would be expected. From the Kataura plot[9] and the Wang diagram[14], previously discussed in section 3.4.3, it can be seen that the E_{33} transition of the (12,11) tube is exactly in resonance at 633 nm giving rise to this very large peak.

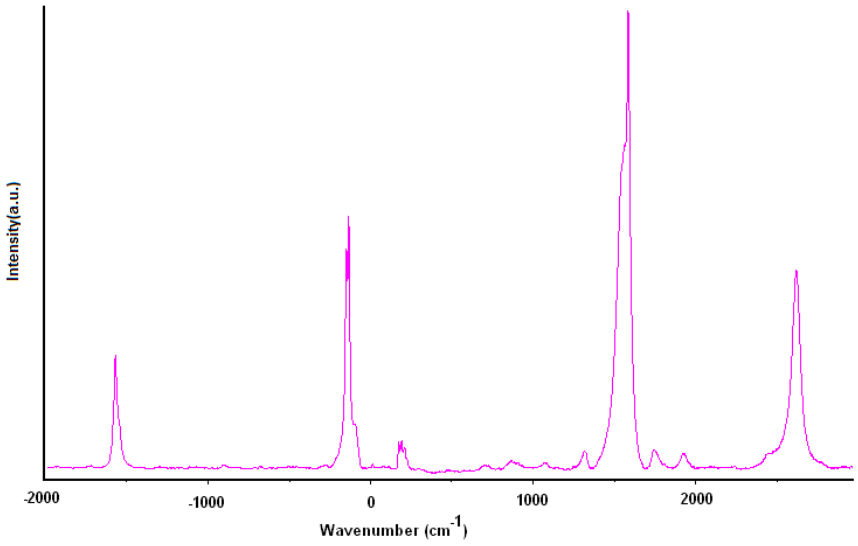

FIGURE 4.14: Stokes anti-Stokes Raman for arc-discharge samples at 633 nm

In summary, as for HiPco samples, examination of the G-line for arc discharge samples shows the presence of both semiconducting and metallic tubes. However, in this case the spectra are semiconducting at 488 nm and 514.5 nm and metallic at 633 nm. Again different tubes are resonant in the Stokes and anti-Stokes spectra at a given excitation energy. This is seen in both the G-line and the RBMs. The mean diameter of resonant tubes again varies for different excitation energies. The shift in the D-line and G*-line is 55 cm^{-1}/eV and 117 cm^{-1}/eV. As with the HiPco tubes the ratios of the intensity of the characteristic lines are similar when the spectra are semiconducting in nature but quite different when the spectrum is metallic. Values of FWHM values of D-line G*-line and fitted G-line peaks are consistent with bundles.

4.5 Conclusion

The analysis of both samples is consistent with the fact that the nanotubes in both samples are in bundles. Since the electronic signature for both samples of tubes is semiconducting at 488 nm, the values calculated of mean diameter at this wavelength can be used to compare the tube diameters. This was done using equation 3.9 and indicates that the arc-discharge tubes (1.44 nm) on average are larger in diameter than the HiPco tubes(1.28 nm). This is further confirmed by the larger FWHM values of the D and G*-lines for the arc discharge tubes. It should be noted that larger tubes were found from the RBM data also.

In this study most of the interesting changes are observed between the 514.5 nm and 633 nm spectra. All future work will be carried out using these laser lines.

What is clear from this study of bundled tube samples is that although the samples are bundled, the characteristics of individual tubes can still be seen. This indicates that even though bundling perturbs the Raman spectra by inhomogeneous broadening, within the samples contibutions of specific tubes can be determined. Specifically this can be observed in the deconvolution of the RBMs and the shape and size of the G-line. It is expected that the FWHM values of the D and G*-lines are broadened due to the bundled state of the sample. This will be further explored in chapter 6.

4.6 References

[1] http://www.sigmaaldrich.com/catalog/search/ProductDetail/ALDRICH/519308 (accessed 8th August 2006)

[2] H.J.Dai, A.G.Rinzler, P.Nikolaev, A.Thess, D.T.Colbert, R.E.Smalley, Chem. Phys. Lett, **260,** 471(1996)

[3] I.W.Chiang, B.E.Brinson, A.Y.Huang, P.A.Willis, M.J.Bronikowski, R.E.Smalley, J.L.Margrave, R.H.Hauge, J. Phys. B **105**, 8297-8301 (2001)

[4] P.Nikolaev, M.Bronikowski, R.K.Bradley, F.Rohmund, D.Colbert, K.A.Smith, R.E.Smalley: Chem. Phys. Lett. **313,** 91-97 (1999)

[5] M.S.Dresselhaus, G.Dresselhaus, R.Saito, A.Jorio Physics Reports **409,** 47-99 (2005)

[6] S.M.Keogh, T.Hedderman, E.Gregan, G.Farrell, G.Chambers, H.J.Byrne, Phys. Chem. B **108,** 6233-6241(2004)

[7] E. Gregan, S.M. Keogh, T.G. Hedderman, G. Chambers, H.J. Byrne, "Opto-Ireland 2002, Optics and Photonics Technologies and Applications", W.J. Blau, J.F. Donegan, A.F. Duke, B.D. MacCraith, J. A. McLaughlin, N.D. McMillan, G.M. O'Connor, E. O'Mongain and V. Toal eds., SPIE Proceedings Volume **4876**, pp.1149 (2003)

[8] T.Hedderman, Ph.d Thesis DIT 2006

[9] H.Kataura, Y.Kumazawa, Y.Maniwa, I.Umezu, S.Suzuki, Y.Ohtsuka ,Y.Achiba Synthetic Metals, **103,** 2555(1999)

[10] S.D.M.Brown, P.Corio, A.Marucci, M.S.Dresselhaus, M.A.Pimenta, K.Kneipp, Phys.Rev.B, **61**, R5137 (2000)

[11] S.D.M.Brown, A.Jorio, G.Dresselhaus, M.S.Dresselhaus, Phys. Rev. B **64,** 73403 (2001)

[12] M.A.Pimenta A.Jorio, S.D.M.Browne, R.Saito, .A.G.Souza Filho, G.Dresselhaus J.H.Hafner, C.M.Lieber, R.Saito, M.S.Dresselhaus Phys. Rev. B **64,** 41401 (2001)

[13] J.F.Cardenas Chem.Phys.Lett. **430,** 367-369 (2006)

[14] Y.F.Wang, X.W.Cao, S.F.Hu, Y.Y.Liu, G.X.Lan Chem.Phys.Lett **336**, 47-52 (2001)

CHAPTER 5

DEBUNDLING OF SINGLE WALLED CARBON NANOTUBE SAMPLES USING ORGANIC SOLVENTS

5.1 Introduction

The previous chapter presented the characterisation by Raman spectroscopy of as prepared SWNT samples, known to be in a bundled or aggregated state. Although the signatures of individual carbon nanotubes are discernable, the true characteristics and underlying physics of the SWNTs and their dependence on structure and state can only be determined in their debundled state.

As discussed in section 1.3, many methods have been reported to successfully debundle single wall carbon nanotubes. The focus of many of these methods has been to disperse the batches of tubes down to the level of single tubes in liquid phase systems. In this study 1,2,dichloroethane (DCE), N,N-dimethylformamide (DMF) and toluene were used as solvents for dispersing single walled carbon nanotubes. Some success with DMF and DCE has previously been reported[1][2]. Both are non-polar solvents and on the basis of like dissolves like should be suitable for dissolving nanotubes. In addition, from the consensus of previous studies as discussed in chapter 1, both should be good candidates as they exhibit high electron pair donicity due to the lone pair on the nitrogen bond in the case of DMF and the fact that DCE is a chlorinated solvent. Toluene was chosen as an example of a solvent with a poor ability to solubilise nanotubes as shown by its use in polymer/nanotube and short chained oligomer/nanotube composite studies[3,4,5].

It was decided to initially characterize these nanotube dispersions using absorption spectroscopy. The reason for this is that, as outlined in section 3.3, all types of nanotubes are active in the UV-Vis-NIR region. This will allow an

examination of the effects of each of the solvents on all tubes in the samples to be made regardless of the diameter or the chirality of the tube. It will also allow comparison of the effects of bundling on different types of tubes to be measured.

5.2 Experimental

Dispersions of single walled carbon nanotubes in the selected organic solvents were made by adding 3 mg of tubes to 20 mls of the solvent. As in chapter 4, two different types of tubes were used in this study. The first type was HiPco tubes, batch number P0288 purchased from Carbon Nanotechnologies. The second was arc- discharge tubes purchased from Sigma-Aldrich batch no. 05224EC. The three solvents chosen for this study were also purchased from Sigma-Aldrich. The DMF used was 99.9% HPLC grade and the 1,2,dichloroethane and toluene were 99.8% HPLC grade. For each solvent and each type of tube, a range of concentrations was made by serial dilution by a factor of two. Each of the dispersions were sonicated using a sonic tip (ultrasonic processor VCX, 750 W) of frequency 300 Hz for 10 minutes and left to stand for 24 hours. This sample preparation protocol was designed based on the experience of others working in the area of nanotube solutions in organic solvents[3][4][5].

UV/Vis/NIR absorption spectra were firstly taken of the solvents and then each solution using a Perkin Elmer UV/Vis/NIR Absorption Spectrometer (Model Lambda 900). This is a double beam, direct ratioing photometric measuring

system using a dynode feedback method. It has a photometric range of ±6 in absorbance with an accuracy of ±0.003 A at 1 A. The instrument has a wavelength range of 185 nm to 3300 nm, with an accuracy of ±0.08 nm. The spectra were obtained using two arrangements of the spectrometer.

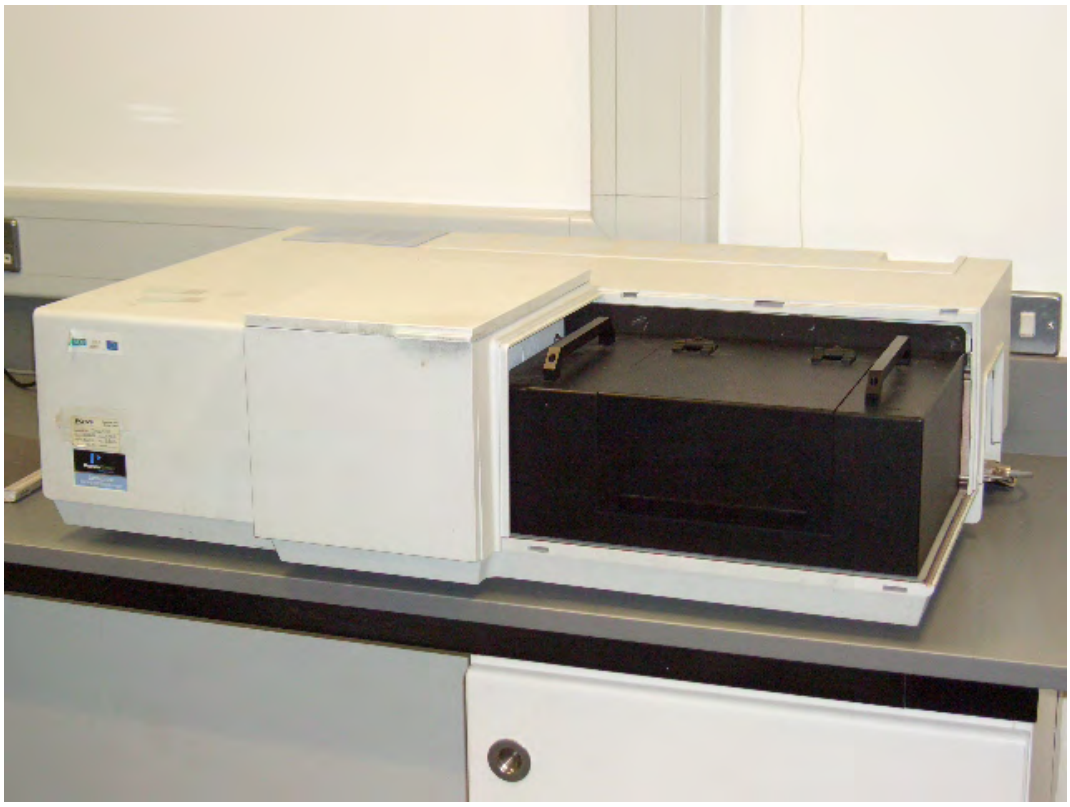

FIGURE 5.1: Perkin Elmer UV/Vis/NIR absorption spectrometer (Model Lambda 900)

The first, the standard experimental arrangement, has the sample to the front of the spectrometer and the reference beam to the back, as shown in figure 5.2. The transmitted light through the sample is measured by the detector and compared to the reference beam. The ratio of the two beams is used to calculate the absorbance according to the Beer Lambert Law, see chapter 3 section 3.3. However this does not take into account the fact that some of the light passing through the sample may have been lost due to scattering of the light rather than absorption of the light.

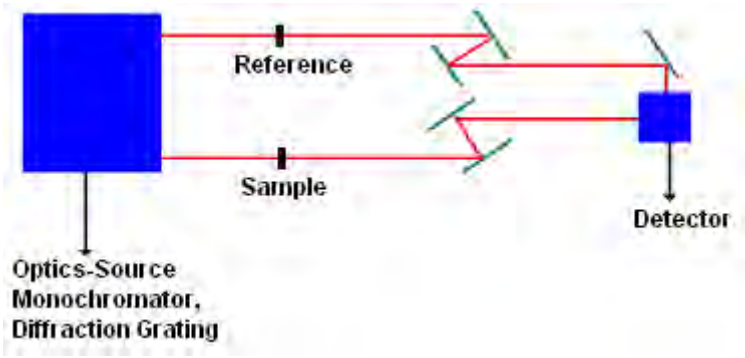

FIGURE 5.2: Standard absorption spectrometer experimental arrangement

The second arrangement used an integrating sphere, the function of which was to reduce loss of light due to scattering and give a more accurate estimate of the absorption of light by the sample material. Here the reference beam was to the front and the sample was placed right up against the entrance to the integrating sphere, as shown in figure 5.3. The switch of the sample and reference configuration is simply because the integrating sphere has a cuvette holder on the rear entrance. The sphere acted to direct all the scattered light into the detector. The ratio of the sample and reference beams was again calculated but this time since there was no reduction in the light lost through the sample due to scattering, the values displayed were a more accurate value of the loss due to absorption by the sample. The difference in the loss in transmission as measured by the two methods gives a direct measure of the scattering losses of the sample.

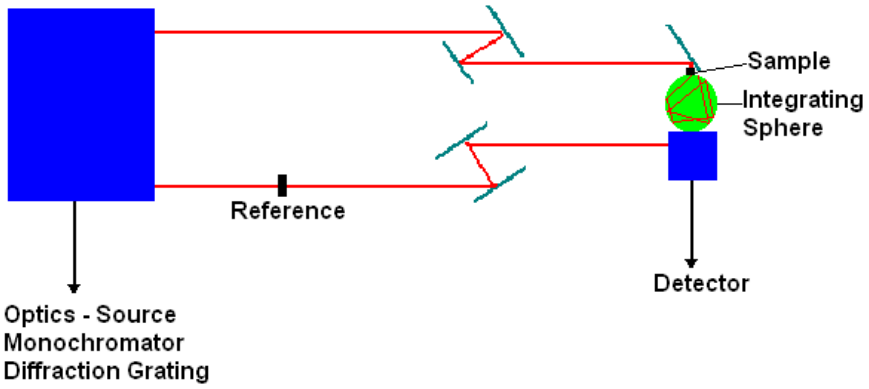

FIGURE 5.3: Absorption spectrometer experimental arrangement using integrating sphere

As the sample is a significant distance from the detector, the absorbance measured from the standard experimental arrangement, A_s, contains contributions from scattering and/or absorption. Equation 3.2 can therefore be rewritten as

$$A_s = (\alpha_{abs} + \alpha_{scatter})lc \qquad 5.1$$

Here α_{abs} is defined as the absorption coefficient, $\alpha_{scatter}$ is defined as the scatter coefficient, which when summed with α_{abs}, represents the total extinction coefficient α_{total}. Utilising the integrating sphere, the scattered light is collected and detected and therefore the absorbance measured is a more accurate assessment of the true optical absorption

$$A_{IS} = \alpha_{abs} lc \qquad 5.2$$

Independent assessment of the contributions of absorption and scattering can therefore be made from the slope of the linear fitting of the absorption in the standard arrangement and in the integrating sphere and the comparison of the

two methods provides an estimate of both the scattering contributions, which are related to bundle size, and the intrinsic absorption of the nanotubes, which may be influenced by the aggregation state.

5.3 Results

Figure 5.4 shows the absorption spectra from the standard arrangement for the three solvents used in this study from 290 nm to 2000 nm.

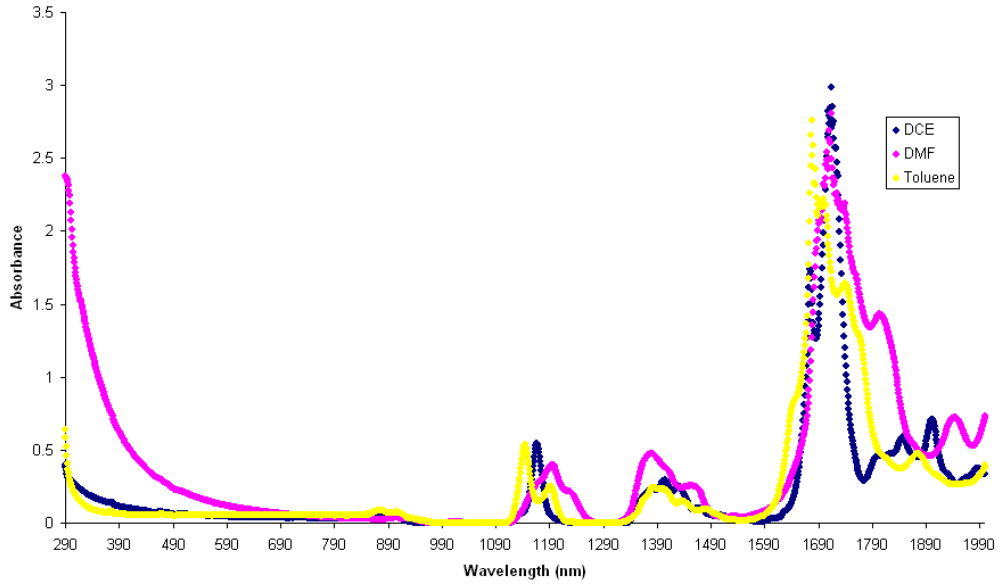

FIGURE 5.4: Solvent absorption spectra

In chapter 3 section 3.2 it was noted that the E_{11}^{M} transitions are around 700 nm and the E_{11}^{S} and E_{22}^{S} transitions are around 1700 nm and 1000 nm[6]. The tubes used to calculate these values were larger in diameter than HiPco tubes. Absorption studies previously carried out on HiPco tubes showed that these values could be reduced by about 100nm across the spectrum[7]. In fact the E_{11}^{M} and E_{22}^{S} regions were found to overlap, E_{22}^{S} 550 – 900 nm and E_{11}^{M} 400-600 nm[7]. So, given the large solvent peaks around 1700 nm 1400 nm and 1200

nm, it was decided that information about all nanotubes in the sample could only be obtained by acquiring spectra between 290 nm and 1100 nm, avoiding the regions of the large solvent peaks.

Absorption spectra were taken for seven concentrations between 1.5 x 10^{-4} kg/L and 2.23 x 10^{-6} kg/L. Figure 5.5 shows the absorption spectrum taken for a 3.75 x 10^{-5} kg/L DCE dispersion in the standard configuration, without the integrating sphere, and therefore is representative of both the SWNT absorption and scattering. The spectrum, which is typical of all spectra obtained, consists of a broad background, which is attributable to plasmon resonance and scattering, on which lie, the features due to the individual nanotube absorptions. These features can be found between 500 nm and 900 nm. In all spectra obtained, there was a discontinuity around 900 nm, which was found to be an instrumental artefact due to the change in the detectors.

Absorbance values were taken at 700 nm and at 1000 nm for all spectra and the variation in these values as a function of concentration was examined to see if the Beer Lambert Law as defined in 3.2 applied.

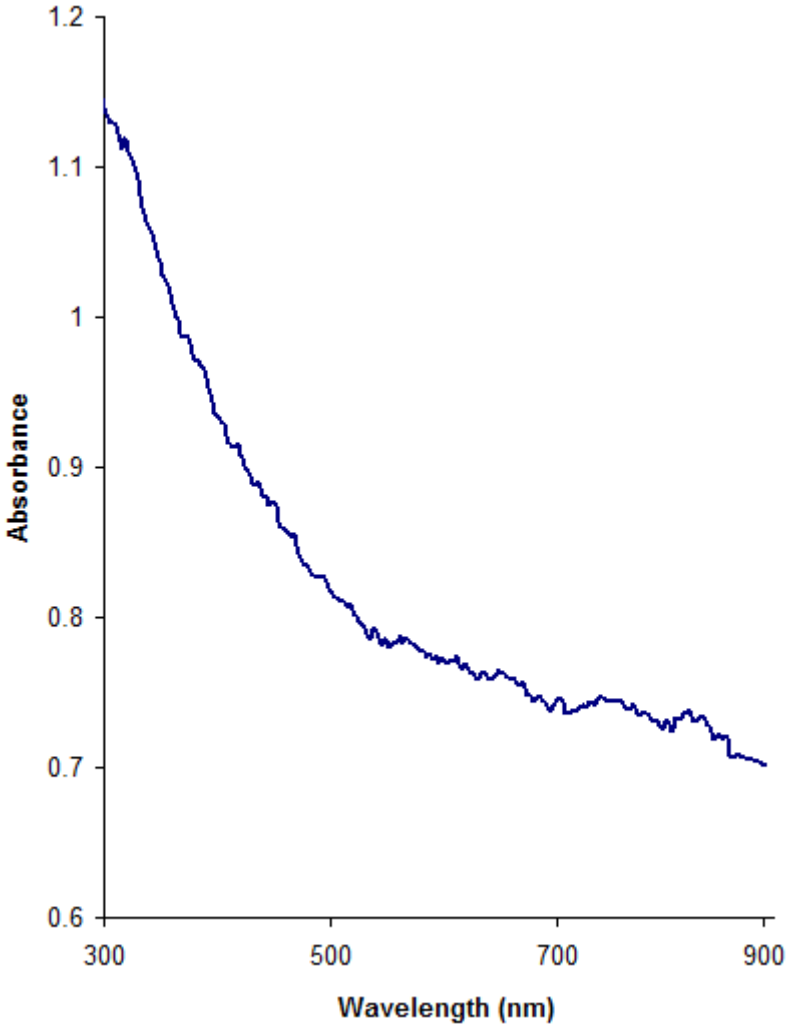

FIGURE 5.5: Absorption spectrum taken for 3.57 x10^{-5} kg/L DCE dispersion (without integrating sphere)

There is considerable deviation from the Beer Lambert law at higher concentrations as shown in figure 5.6. Such a deviation is common in organic molecular materials and is attributable to a reduction of the intrinsic material absorption due to aggregation[8]. In the case of carbon nanotubes, such a deviation is not unexpected as, at higher concentration, in addition to any effects of intermolecular interactions, the dispersions do not consist of single tubes or even ropes but aggregated masses of ropes and maybe even impurity particles. The scatter from these would be large and contribute to this deviation.

Extrapolating to the lowest concentrations, a more linear behaviour, in accordance with the Beer Lambert law, can be seen, indicating that aggregation and scattering effects are reduced and a better dispersion is achieved as the concentration is decreased. Error margins include uncertainty in baseline and absorbance maximum. The solid line as a guide to the eye indicates that a linear behaviour of the absorbance at both wavelengths persists from concentrations of approximately 2 x 10^{-5} kg/L to infinite dilution.

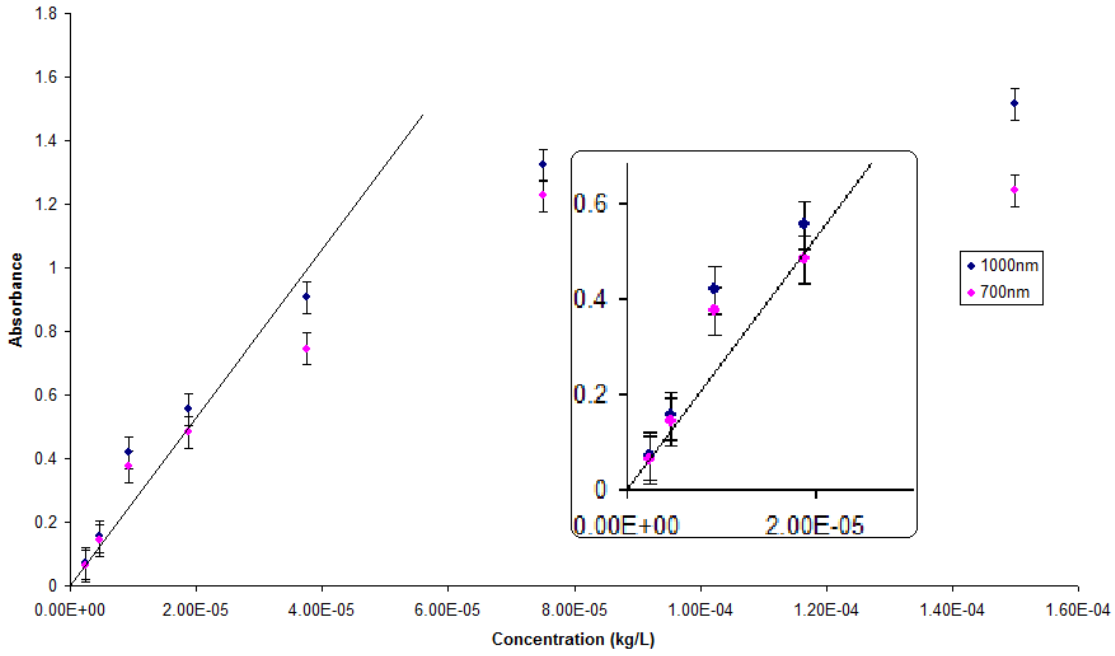

FIGURE 5.6: Absorbance values at 700 nm and 1000 nm for DCE HiPCo nanotube dispersions (The solid line is a guide to the eye). Inset is the linear region

This discontinuity from Beer Lambert behaviour to non Beer Lambert behaviour with increasing concentration has been previously observed[9][10]and used to define the debundling point. The debundling point is taken as the concentration at which the discontinuity is observed. Based on these studies the concentration dependence of the absorption as measured using the standard spectrometer geometry indicates that there is some degree of debundling at low

concentrations. Even at low concentration, however, there may be scatter due to small bundles and even the length of any isolated tubes. Examination of the absorbance spectra from the same solutions using the integrating sphere shows some interesting results. For a given concentration there is quite a difference between the absorption spectra taken with and without the integrating sphere. Figure 5.7 shows this for the concentration, 7.5×10^{-5} kg/L of HiPco in DCE.

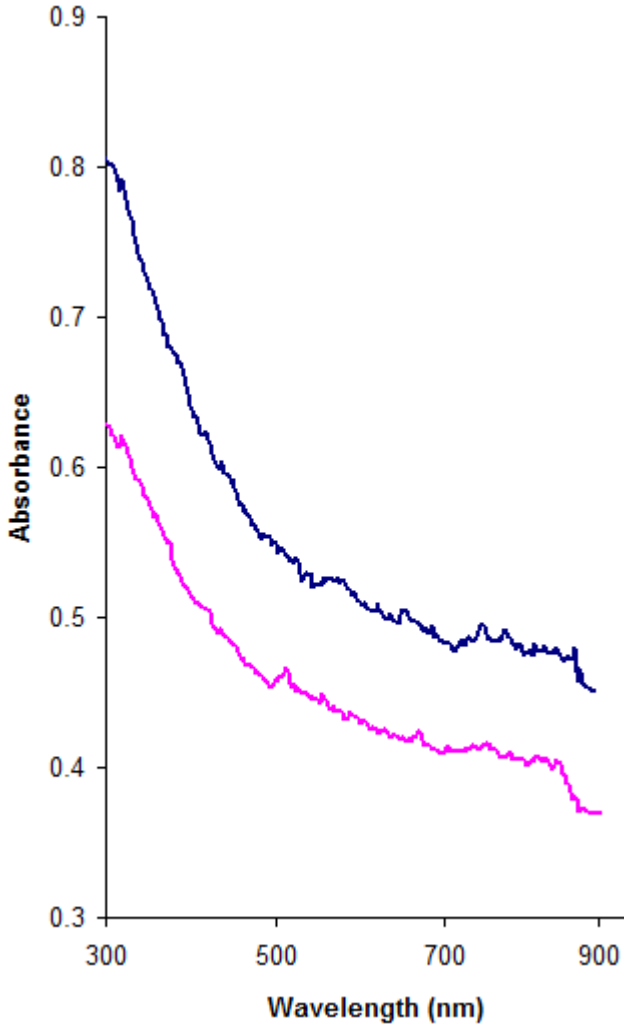

FIGURE 5.7: Spectra taken with and without Integrating sphere for concentration 7.5×10^{-5} kg/L

The magnitude of the absorbance values are reduced across the spectrum. This reduction is attributed to the removal of contributions due to scatter which appears to be largely spectrally independent. The source of scattering is, in

general, Rayleigh scattering when the size of the scattering particle is less than the wavelength or Mie scattering when the particle size is bigger than the wavelength[11]. In length, carbon nanotubes are micron in size and so would be expected to exhibit Mie-type scattering[11]. In width however their size is much less than the wavelength whether one is dealing with individual tubes or bundles (even large bundles are only 100 nm in width). The relative spectral independence of the scattering as observed in figure 5.7 suggests that it has predominant origins in Mie-type scattering although it has been shown that the intensity of Rayleigh scattering is reduced with decreasing bundle size[12]. Notably, figure 5.7 demonstrates that the use of the integrating sphere can significantly reduce the contributions of the scattering allowing a more accurate measurement of the absorption spectrum.

The second observation is that, using the integrating sphere, the features associated with the van Hove singularities are downshifted and better defined at lower concentrations as illustrated in figure 5.8. As discussed in chapter 3, this would be indicative of smaller bundles or indeed individual tubes. It should be noted however that this improved resolution is not as well defined as in the case of debundling using surfactant systems[9].

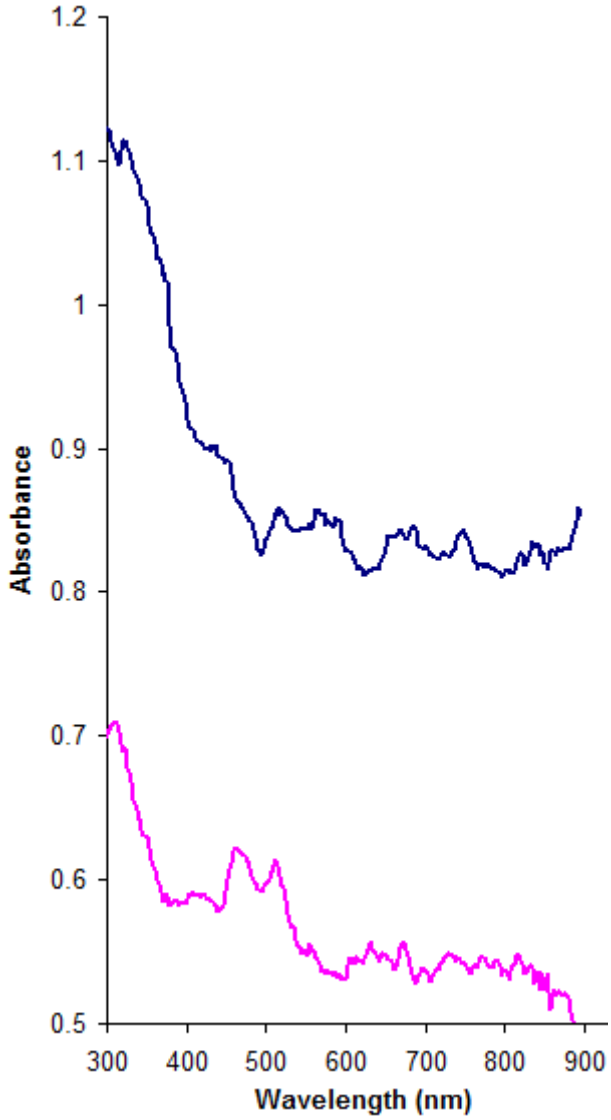

FIGURE 5.8: Spectra taken for DCE/nanotube dispersions at two different concentrations using the integrating sphere

Applying the Beer Lambert Law to the data from spectra obtained using the integrating sphere shows roughly the same linear behaviour as before at lower concentrations with a marked deviation at higher concentrations, as shown in figure 5.9. Without the integrating sphere this linearity was observed up to a concentration of 1 $x10^{-5}$ kg/L, while with the integrating sphere the linearity was observed to a concentration of 2 $x10^{-5}$ kg/L. The deviation from linearity may not just be due to scattering but also due to a loss of oscillator strength due to

aggregation, as commonly observed in organic dyes[8] and therefore, as previously mentioned, can be used as an indicator of debundling levels[9][10].

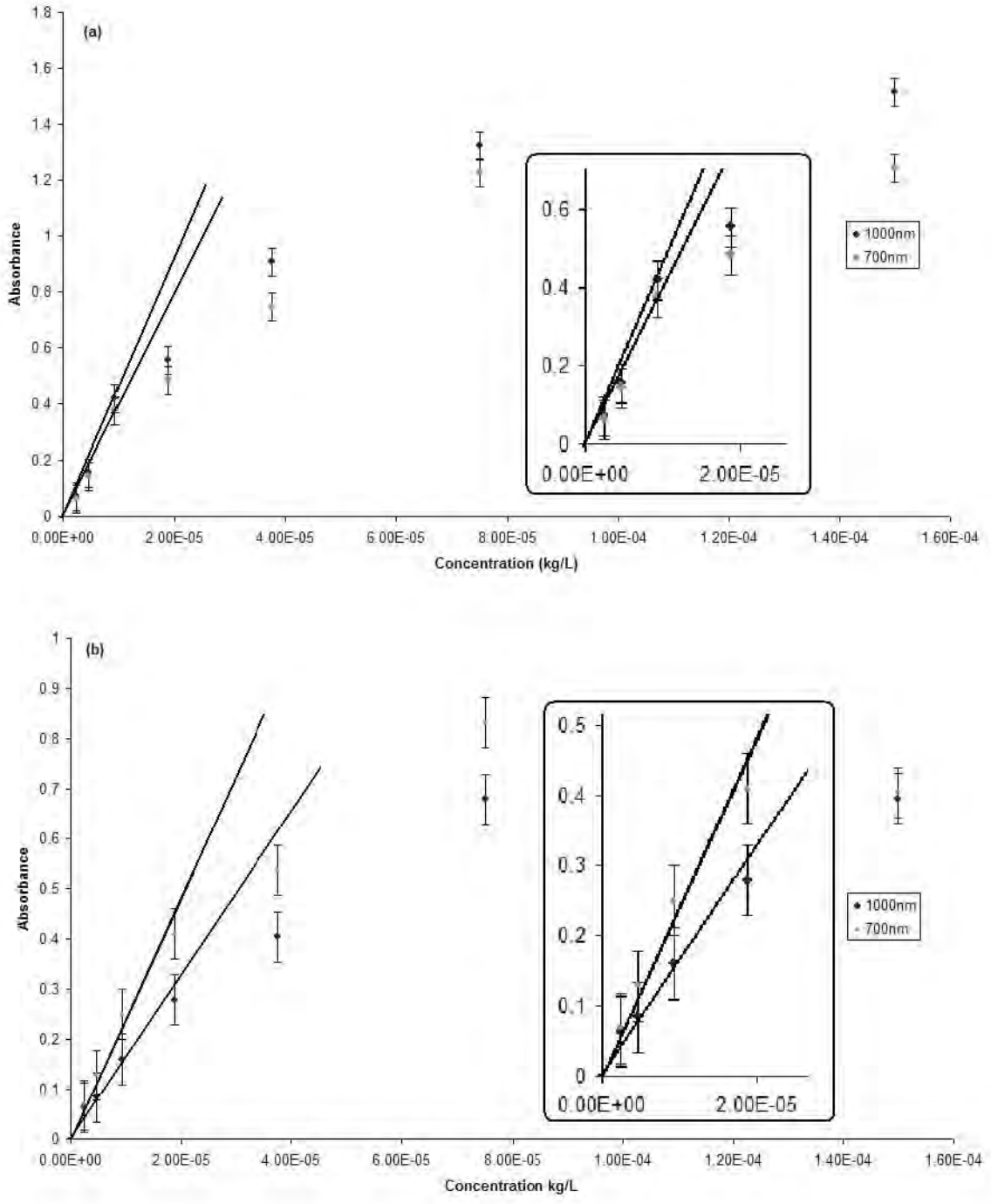

FIGURE 5.9: Absorbance values at 700 nm and 1000 nm for DCE HiPco nanotube dispersions measured using (a) standard arrangement (b) the integrating sphere (the solid line is a guide to eye). Insets of linear regions

The data from DMF and toluene dispersions show similar patterns to that obtained from the DCE dispersions. However, there are some marked differences. This can be seen more clearly by examining a set of graphs (one for each solvent) of the absorbance (using the integrated sphere) and scatter as a function of concentration. As mentioned earlier the scatter can be measured by subtracting the absorption spectra obtained using the integrating sphere from those obtained with the standard arrangement. The graphs shown below in figure 5.10 are taken for absorbance at 700 nm. A similar pattern can be seen for values taken at 1000 nm.

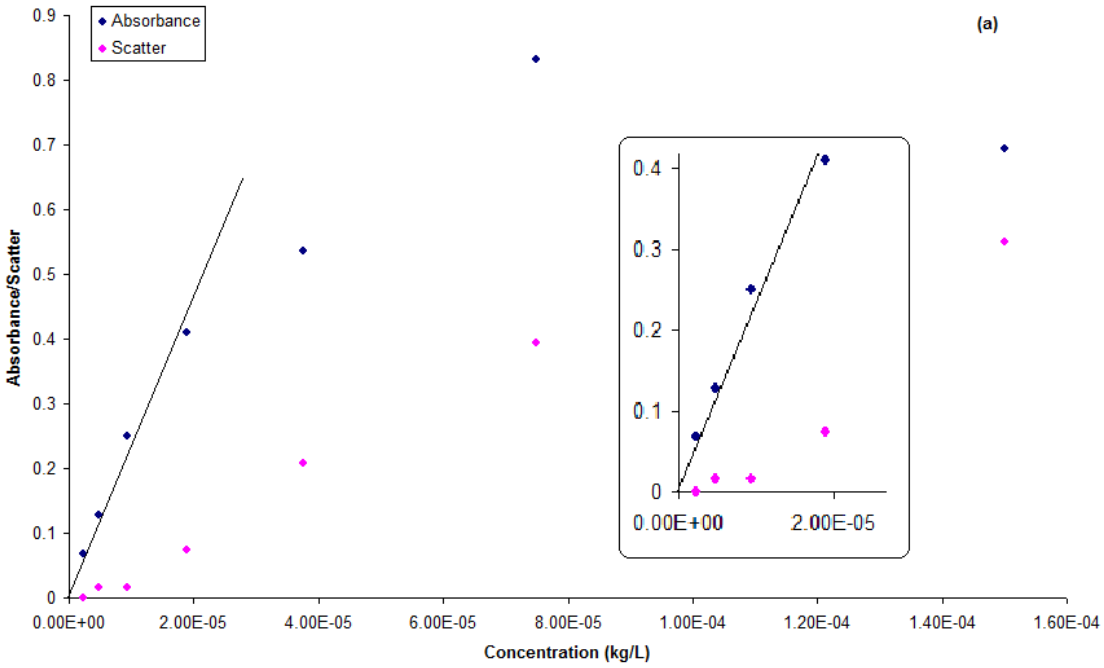

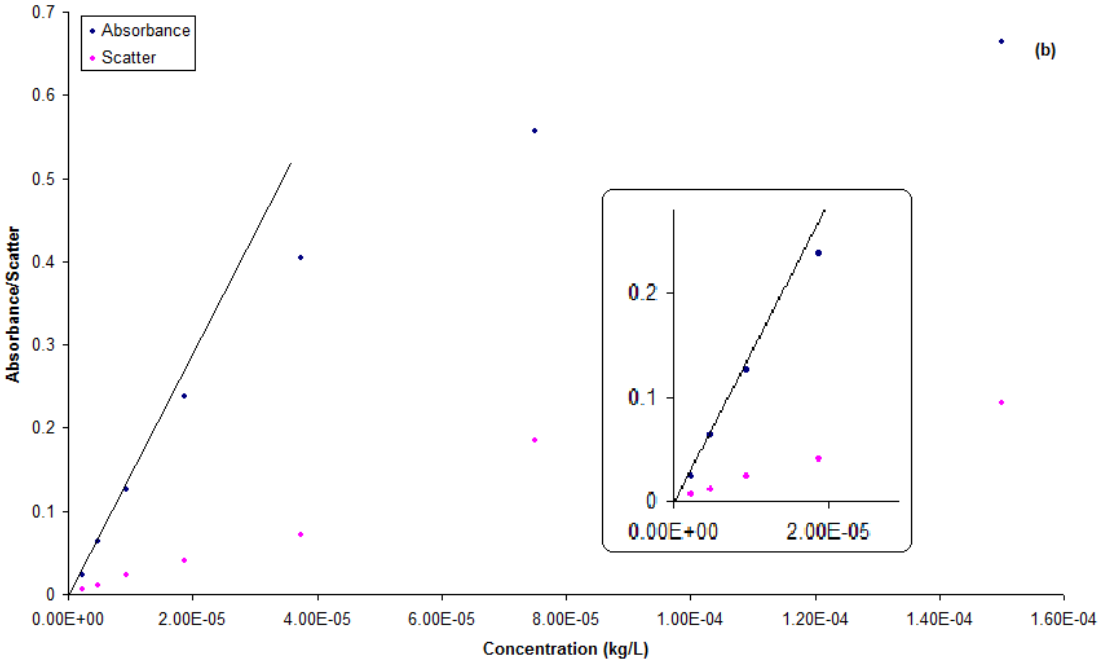

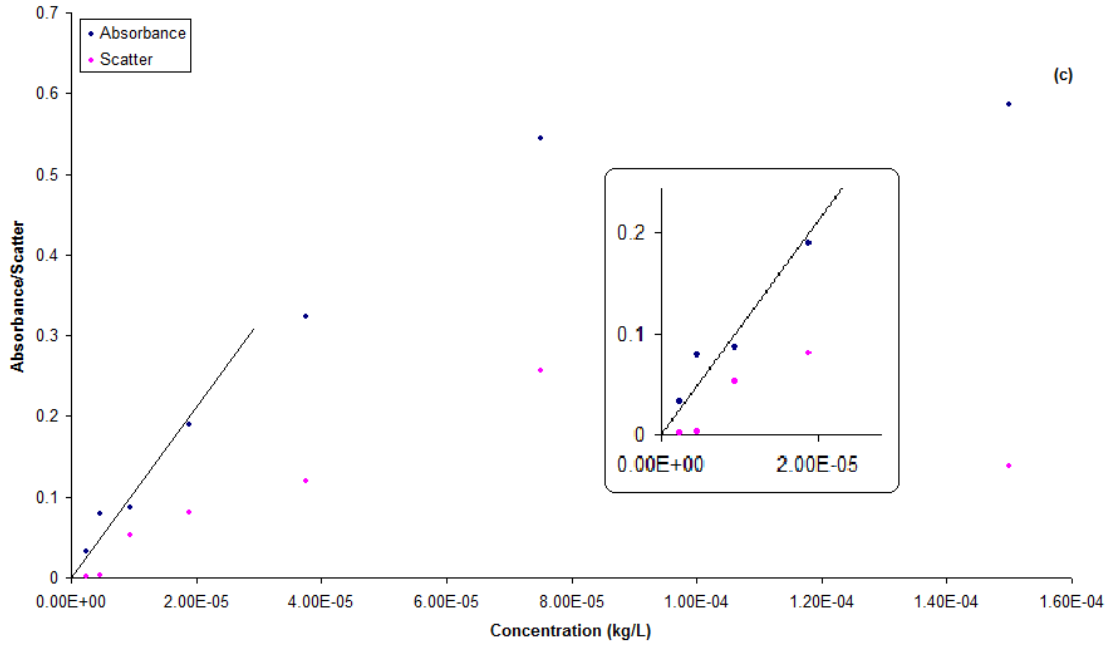

FIGURE 5.10: Absorbance/scatter (a) DCE (b) DMF (c) toluene/ HiPco dispersions taken at 700 nm((The solid line is a guide to eye) . Insets of linear regions

The extinction coefficients as measured using the integrating sphere, $\alpha_{abs,}$ calculated from the slopes of the graphs at low concentrations for each of the solvents and tube type are shown in table 5.1 below. The experiment was duplicated so the values are average values. It should be noted that these values differ for tube type as well as solvent and since there are no reports of a strong solvatochromism in nanotubes it is concluded that these differences are a measure of solubility.

	α_{DCE} ($x10^3$ $Lkg^{-1}m^{-1}$)	α_{DMF} ($x10^3$ $Lkg^{-1}m^{-1}$)	$\alpha_{Toluene}$ ($x10^3$ $Lkg^{-1}m^{-1}$)
HiPco	2627 ± 39	1316 ± 33	1050 ± 19
AD	2201 ± 92	2220 ± 194	1199 ± 61

TABLE 5.1: Extinction coefficients for DCE, DMF and toluene measured at 700 nm

Extinction coefficient values have been previously calculated for other HiPco/ solvent solutions. For example: chloroform[1][13] 1424 $x10^3$ $Lkg^{-1}m^{-1}$, MCB[14] 1196 $x10^3$ $Lkg^{-1}m^{-1}$, o-DCB[14] 1650 $x10^3$ $Lkg^{-1}m^{-1}$, m-DCB[14] 1313 $x10^3$ $Lkg^{-1}m^{-1}$ and TCB[14] 1658 $x10^3$ $Lkg^{-1}m^{-1}$.

From table 5.1 it can be seen that DCE is roughly the same for both types of tube. Its extinction value is larger than any of the other solvents listed above. DMF is similar to DCE for arc discharge tubes but much lower for HiPco tubes. It has been shown[15] that the binding energy of tubes in bundles decrease with increasing tube diameter. It therefore seems that the non polar DMF has greater difficulty in dispersing the larger diametered arc discharge tubes. From visual observation, in all 3 solvents the arc-discharge tubes went more easily

into solution than the HiPco tubes. The impurity content of the arc-discharge tubes is greater than the HiPco tubes and this may reduce the bundle packing density and aid the dissolution process[9]. The extinction coefficient values for toluene are clearly less than either DCE or DMF for both tube types.

The on-set of a linear relationship between absorbance and concentration with decreasing concentration was not observed to occur at the same point for all three solvents. This concentration, $\mathbf{C_c}$, referred to as the dispersion limit in other studies[10,16], is the concentration at which the suspensions are monodisperse, as determined using atomic force microscopy (AFM). For this study it is taken as the point of discontinuity in the absorbance spectra.

Solution	**Dispersion Limit X10^{-5} kg/L**
DCE	HiPco-2.00 ± 0.5 Arc-Discharge-2.00 ± 0.5
DMF	HiPco-2.00 ± 0.5 Arc-Discharge -2.00 ± 0.5
Toluene	HiPco-0.50 ±0.5 Arc-Discharge -0.50 ±0.5
NMP[12]	2(HiPco)
Surfactants[11]	7(HiPco)

TABLE 5.2: Measured dispersion limits for DCE, DMF and Toluene plus solvents from other studies

All three solvents have dispersion limits similar to other solvents such as NMP and surfactants. It should be noted that the dispersion limit for toluene however is significantly lower. Note that the values measured are the same for both types of tubes.

In each case, at low concentrations the scatter is removed but not fully. In DCE and toluene, the scatter is abruptly reduced at the debundling point. In DMF there is no abrupt reduction in scatter at the debundling point but rather a steady reduction in the scatter with decreasing concentration. From figure 5.10 the scatter values measured for HiPco and arc-discharge tubes at a concentration of $1x10^{-5}$ kg/L can be determined and these are shown in table 5.3. Note that this concentration is below the dispersion limit for DCE and DMF.

Tube Type	DCE	DMF	Toluene
HiPco	.02	.03	.01
Arc-Discharge	.02	.03	.04

TABLE 5.3: Scatter measured at $1x10^{-5}$ kg/L

The amount of scatter is related to the size of the scattering particle but it is also related to the amount of scattering sites available. For the arc-discharge tubes it is clear that the size and/or number of the scattering particles is bigger for the toluene dispersions as the value of the scatter is bigger. The value of the scatter in the HiPco toluene dispersions at first seems smaller than say the DCE solutions. However, considering that the amount of tubes present, as given by the extinction coefficient, is a factor of 2.5 times smaller, the toluene must have larger bundles of tubes. DCE has smaller scatter values than DMF indicating that the size of the scattering particles is smaller in DCE.

In summary, from the absorption study it is clear that all three solvents disperse nanotubes to some extent at the dispersion limit but indications are that DCE and DMF are much better than toluene, which even at low concentrations

doesn't seem to disperse the tubes. At this point microscopy is required to verify these findings.

5.4 Microscopy of Solutions

The absorption study of these nanotube solutions indicates changes in the bundle size at specific concentrations. Clearly at 4 $x10^{-5}$ kg/L for all solvents, the absorption studies indicate that the tubes are still bundled while at 1 $x10^{-5}$ kg/L they are debundled for DCE and DMF but are still partially bundled for toluene. To confirm this it is necessary to examine the aggregation state of these tube dispersions as a function of concentration using high resolution microscopy. Both Transmission Electron Microscopy (TEM) and Atomic Force Microscopy (AFM) were used in this study.

For the TEM study a Jeol 100 CX transmission electron microscope was used with an applied voltage of 100kV. Normally TEM is done by drop casting the solution on copper grids that have been covered with an electron transparent polymer, 3% formvar resin in 1,2,dichloroethane. However the organic solvents used in this study dissolved the substrate so an alternative method had to be found. Holey carbon grids, 5147-4, were obtained from Agar Scientific and the nanotube solutions were drop cast onto them. The grids were left for 24 hours and the solvents were allowed to evaporate off.

Figure 5.11 shows some TEM images of HiPco tubes dispersed in DCE. At this magnification a large area of the sample can be seen. The first thing to note is

that the HiPco tubes, although smaller in diameter than arc-discharge tubes are very entangled. The second thing to note is that it can clearly be seen that the nanotubes in the 1 x 10^{-5} kg/L sample are more dispersed.

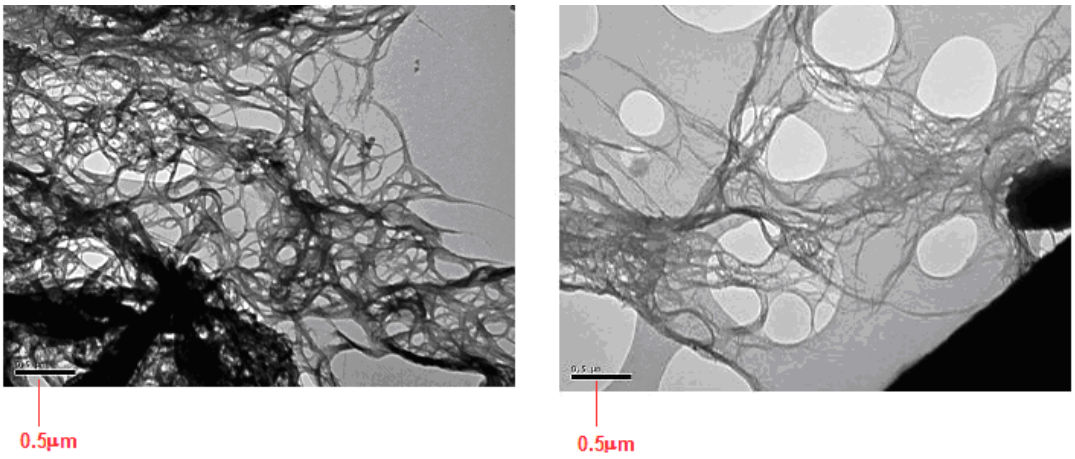

FIGURE 5.11: TEM image of HiPco tubes dispersed in DCE. On the left concentration 4 x 10^{-5} kg/L on the right concentration 1 x 10^{-5} kg/L. The magnification factor is 40,000.

Noting that at this magnification the analysis software was limited to determining sizes of 10nm, the average size of the HiPco nanotubes features in DCE was calculated for the larger concentration to be 28 nm and the lower concentration to be 13 nm. Remembering that the original bundle size was approximately 30 nm the lower concentration shows some level of debundling. TEM images of DMF and Toluene samples at a concentration of 1 x 10^{-5} kg/L are shown in figure 5.12 and give average values of the physical features of 15 nm and 23 nm respectively.

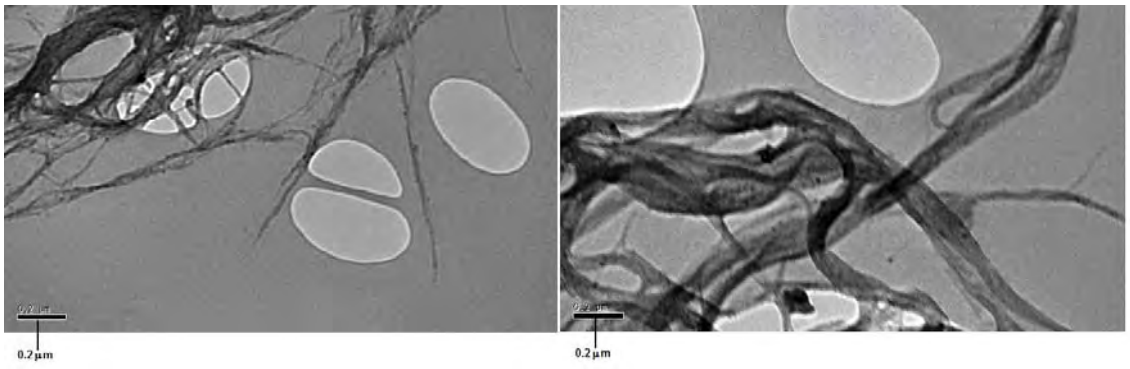

FIGURE 5.12: TEM image of HiPco tubes deposited from a concentration of 1 x 10^{-5} kg/L in DMF (left) and toluene (right). The magnification factor is 80,000.

This indicates that DCE and DMF have similar abilities to debundle HiPco tubes and that they are much better than toluene. Similar results were obtained for the arc discharge tubes. This is consistent with the results of the absorption study. Of course it should be noted that there is no guarantee that re-bundling of the nanotubes has not taken place once they are out of solution and as such the values of bundle thickness measured with the TEM are not an accurate estimate of the bundle size in solution. Due to difficulties in acquiring good TEM images of the dispersions and difficulties in accurately measuring the tube diameter with the TEM it was decided to perform AFM on the samples. Furthermore it was decided to concentrate on DCE as all indications are that it is a better solvent for all tube types.

Although the TEM study indicates that DCE and DMF samples are similar, the scatter data indicates that in DCE samples below the dispersion limit the particle size is smaller than in DMF samples. Therefore it was decided to carry out an AFM study just on DCE samples to verify that full debundling is happening.

Tapping mode atomic force microscopy (AFM) was carried out on some DCE samples, using a Digital Instruments Multimode Nanoscope IIIA. Point-probe silicon nitride cantilevers (force constant = 42 N m^{-1}, resonant frequency = 330 kHz) were used for all measurements. The tip size was 10nm and there were 512 lines per scan. The resolution was 0.5 nm. Due to the shape of AFM tips in general the image in the X-Y plane is broadened and accurate measurements are hard to make. However this broadening does not occur in the z direction so measurements of height can be made from AFM images with a good degree of accuracy. The samples were prepared by drop casting the nanotube solutions on to silicon substrates which had previously been cleaned in boiling isopropanol for half an hour and then bath sonicated in acetone. The drop cast samples were then dried in a vacuum oven, providing fast evaporation to avoid re-bundling of the nanotubes.

AFM from a sample of 1 x 10^{-5} kg/L, just below the dispersion limit, can be seen in figure 5.13.

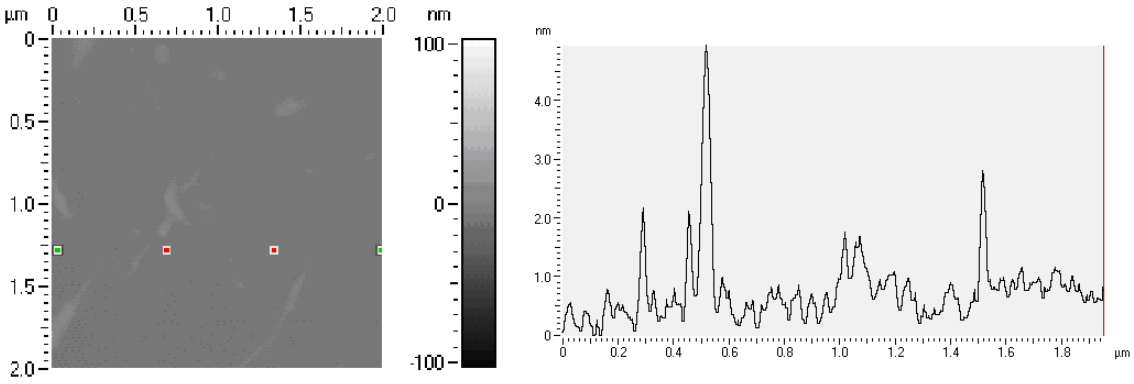

FIGURE 5.13: AFM of HiPco nanotubes in DCE at a concentration of 1 x 10^{-5} kg/L

On the left is the AFM image showing a number of features. On the right is a 2D profile taken across the sample along the line indicated on the image. The y axis of the profile is the height of the feature. Many images were taken at different places across the sample. Multiple profiles were taken for each image. A histogram was constructed of measurements made of the heights from all the images. This can be seen in figure 5.14.

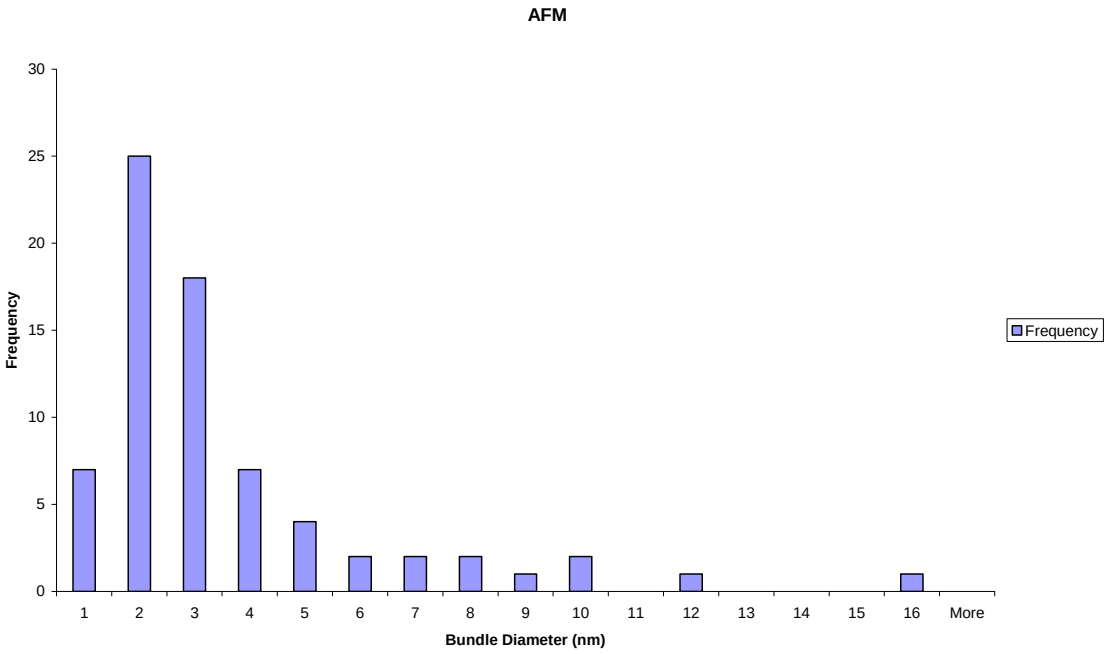

FIGURE 5.14: Histogram of AFM height measurements of HiPco nanotubes in DCE at a concentration of 1 x 10^{-5} kg/L

It can be seen that the large bundles have been significantly debundled and that the average bundle size is less than 2-3 nm. This verifies the indications from the absorption data that at this concentration a large degree of debundling has occurred. Absorption and scatter curves for DCE dispersions indicate that they are debundled below 2 x 10^{-5} kg/L and this is confirmed by AFM.

5.4 Conclusion

DCE, DMF and toluene can be used to disperse single wall nanotubes to varying degrees of effectiveness. Different tube types are best dispersed with different solvents. While absorption spectroscopy is a valuable tool to monitor the characteristics of a SWNT sample use of the integrating sphere can be used to differentiate scatter from the suspensions and to yield a more accurate absorption spectrum. Monitoring the concentration dependence of the scatter and absorption can be used to identify the critical debundling point and to semiquantitatively compare the degree of dispersion and relative bundle sizes in different solvents. Debundling certainly occurs with all 3 solvents, the DCE and DMF being equally effective with arc-discharge tubes but the DCE is much better for HiPco tubes. TEM and AFM verify that debundling has occurred in DCE.

Chapter 6 investigates the Raman spectroscopy of debundled tubes. Based on the above results DCE will be used to debundle single walled carbon nanotube samples for this Raman study. The results obtained will be compared and contrasted with those for raw sample presented in chapter 4.

5.5 References

[1] J.L.Bahr, E.T.Mickelson, M.J.Bronikowski, R.E.Smalley, J.M.Tour, Chem. Com. 193-194 (2001)

[2] K.K.Kim, D.J.Bae, C.M.Yang, K.H.An, J.Y.Lee, Y.H.Lee, Nanoscience and Nanotechnology **5,** 1055-1059 (2005)

[3] E.Gregan, S.M.Keogh, A.Maguire, T.K.Hedderman, L.O Neil, G.Chambers, H.J.Byrne Carbon **42,** 1031 (2004)

[4] S.M.Keogh, T.K.Hedderman, E.Gregan, G.Farrell, G.Chambers, H.J.Byrne J.Phys.Chem **108,** 6233-6241 (2004)

[5] T.K.Hedderman, S.M.Keogh, G.Chambers, H.J.Byrne J.Phys.Chem.**110,** 3895 (2006)

[6] Kataura, Kumazawa, Maniwa, Umezu, Suzuki, Ohtsuka ,Achiba Synthetic Metals, **103,** 2555(1999)

[7] O Connell, Bachillo, Huffman, Moore, Strano, Haroz, Rialon, Boul, Noon, Kittrell, Ma, Hauge, Weisman, Smalley Science **297,** 593-596 (2002)

[8] A.Mahfound, A.Sarangan, T.Nelson, E.Blubaugh J. of Luminescence **118,** 123 (2006)

[9] P.Bashir, H.J.Byrne J.Phys.Chem.C **112**, 332 (2008)

[10] S.Giordani, S.D.Bergin, V.Nicolosi, S.Lebedkin, M.M.Kappes, W.J.Blau, J.N.Coleman J.Phys.Chem B **110,** 15708-15718 (2006)

[11] R.C. Haddon, J. Sippel, A.G. Rinzler, and F. Papadimitrakopoulos MRS The Materials Gateway **29,** 4 (2004)

[12] M.Wilson, K.Kannangara, G.Smith, M.Simmons, B.Raguse, *Nanotechnology:Basic Science and Emerging Technologies* Chapman and Hall (2002)

[13] S.Debnath, Q.Cheng, T.Hedderman, H.J.Byrne, J.Phys.Chem. C **112**, 10418 (2008)

[14] Q.Cheng, S.Debnath, E.Gregan, and H.J. Byrne J.Phys.Chem. C in press

[15] J.Wang, Z.Jin, J.Cheng and Y.Li J.Phys.Chem C **113,** 8132 (2009)

[16] B.J.Landi, H.J.Ruf, J.J.Worman, R.P.Raffaelle J.Phys.Chem B **108,** 17089 (2004)

CHAPTER 6

ROOM TEMPERATURE RAMAN STUDY OF DEBUNDLED SINGLE WALLED CARBON NANOTUBES

6.1 Introduction

In chapter 5 it was shown that the organic solvents 1,2 dichloroethane (DCE) and N,N-dimethylformamide (DMF) can be used to debundle single walled carbon nanotubes. It was found that debundling occurred for dispersions below $2.00\pm0.5 \times 10^{-5}$ kg/L. TEM and AFM were used to visualise the debundling indicated by the discontinuities in the concentration dependence of the absorption spectroscopic response. Chapter 6 examines the use of Raman spectroscopy in the detection and characterisation of the level of debundling in single walled carbon nanotubes. Studies are limited to DCE, as it showed efficient debundling. As discussed in chapter 1, currently used techniques, such as AFM and TEM, are laborious, time consuming and capitally expensive and required trained personnel to operate. A simple technique using Raman which could estimate debundling levels would be of great universal advantage in the processing of bulk produced nanotube materials. In this chapter Raman spectra of samples dispersed at different concentrations in DCE and deposited on solid substrates are examined. Changes in the spectra in comparison to those of the raw samples presented in chapter 4 are determined and quantified in terms of shifts in phonon frequencies, linewidths of the characteristic lines, RBM profile and the size of the Breit-Wigner-Fano lineshape. From these changes in the spectra, the changes in the Raman spectrum characteristic of debundling can be determined. It is proposed that this technique would be more suitable for the high throughput applications required in industrial situations.

6.2 Initial Experimental

Raman measurements were again taken using an Instruments S.A. Labram 1B spectroscopic microscope. The details of this instrument have been outlined in chapter 4 section 4.2. Following the detailed analysis of Raman spectra of as produced samples in chapter 4, spectra were taken at 514.5 nm and 633 nm as it had was concluded that by using these two excitation lines the most information could be gleaned from the spectra. As before, two types of tubes were used in the study, HiPco tubes purchased from Carbon Nanotechnologies Incorporated, batch number P0288 and arc discharge tubes purchased from Sigma-Aldrich, batch number 05224EC. Dispersions of both were produced according to the procedure outlined in chapter 5 section 5.2.

The first question that arose was whether the Raman study, like the absorption study, could be carried out on the dispersions of organic solvents and single walled nanotubes prepared according to the description outlined in chapter 5 section 5.2. Previous reports of Raman dispersions were conducted in water based dispersions[1]. Water is known to be an extremely weak Raman scatter and is thus an ideal medium for measuring Raman of solutions/dispersions. However such a study sheds no light on the efficiency of organic solvents to disperse SWNTs. Dispersion measurements would be optimal as a bulk average of the state of the nanotubes in the solvent as a function of concentration could be made[1]. It was decided to use a very concentrated dispersion at first to establish the detectability of SWNTs in the solvent. If the Raman signature of a high concentration of tubes could not be obtained then there would be no point in looking at the lower concentrations, where it is known from the absorption studies that debundling takes place. Initially 2 mg of HiPco

tubes were added to 10 mls of solvent. The dispersion was sonicated for 10 minutes and left to stand for 24 hours. After this time it was noted that most of the tubes had fallen out, as expected. What was left was a saturated dispersion of solvent and tubes. Raman spectra were taken of solvent, raw tubes and solvent/tube dispersion at 514.5 nm. The resulting spectra can be seen in figure 6.1.

Initial examination of the DCE spectrum shows that it has peaks in the frequency region corresponding to the RBM region of the tubes. This makes it unlikely that any RBMs will be seen in the dispersion spectrum. However there are no peaks around 1590 cm^{-1} which is the position of the G-line in nanotubes indicating that it may be possible to see the G-lines of the tubes. Also the G*-line in the region of 2600 cm^{-1} is clean. However, when the spectrum of the nanotube dispersion is examined there is no sign of the G-line or the G*-line in the spectrum. It is clearly dominated by the solvent spectrum.

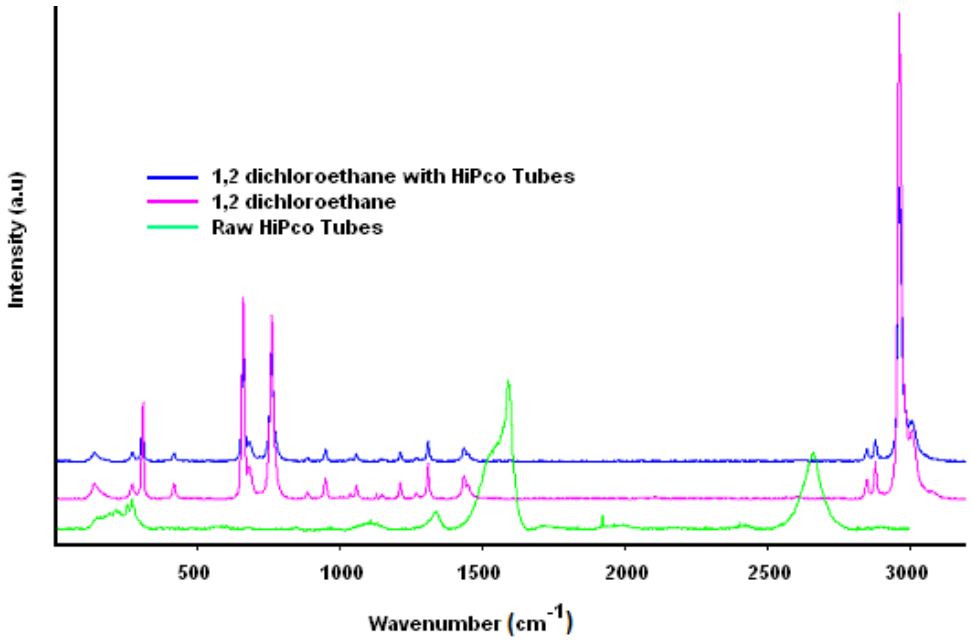

FIGURE 6.1: Stokes Raman spectra at 514.5 nm for raw HiPco tubes, DCE and DCE nanotube solution of concentration 2 x 10^{-3} kg/L

This study was also carried out at 633 nm and for arc discharge dispersions at both excitation wavelengths. The results were similar to the above. As a result it was concluded that Raman spectroscopy could not be carried out in solution and would have to be carried out in the solid state by drop casting from each solution onto glass slides and allowing the solvent to completely dry off.

There was, however, a possibility that although the solvent may debundle the tubes in solution, samples prepared by simple drop casting may in fact re-aggregate on the slides. The actual effects on the Raman spectrum due to the debundling by the solvents would not therefore be measured. Simple observation of the drop cast samples in fact showed large clumps of nanotubes indicating that they had re-aggregated. The Raman spectra of these samples showed very little difference from that of the raw tubes. It was decided to test to see if the use of activated slides would in fact immobilize the nanotubes on the substrate as they are coming out of solution and keep them in the same debundled state as they had been in the dispersions.

The slides were activated using 1,1,1 tri-ethoxy (aminopropyl) silane (APS solution)[2]. This process involved making up a 1% v/v solution of APS in de-ionised water. Some of this solution was then drop cast onto clean microscope glass cover slides. The slides were then allowed to sit for ten minutes. This time was kept constant for all slides as the thickness of the film created by the APS solution is directly proportional to the amount of time the solution sits on the slide[2]. After ten minutes the slides were rinsed with de-ionised water and allowed to air dry. The nanotube solutions were then drop cast onto the

activated slides. No obvious re-aggregation of the tubes was observed microscopically.

Samples of all concentrations of HiPco tubes in DCE were drop cast onto non-activated and activated slides and spectra taken at 633 nm. These were then compared to that of a raw HiPco tube sample. Figure 6.2 shows the effects of slide activation for the concentration 1.5 x 10^{-5} kg/L. Both the activated and non-activated slides show some shifting of the spectra indicating a change in the bundle size[3]. In chapter 5 it was shown that at this concentration the nanotubes are significantly dispersed in the solvent. This shifting of the spectral features is most clearly seen in the expanded RBM region, figure 6.2(b). The shifting is greatest for the activated slide indicating that some rebundling has occurred on the non-activated slide.

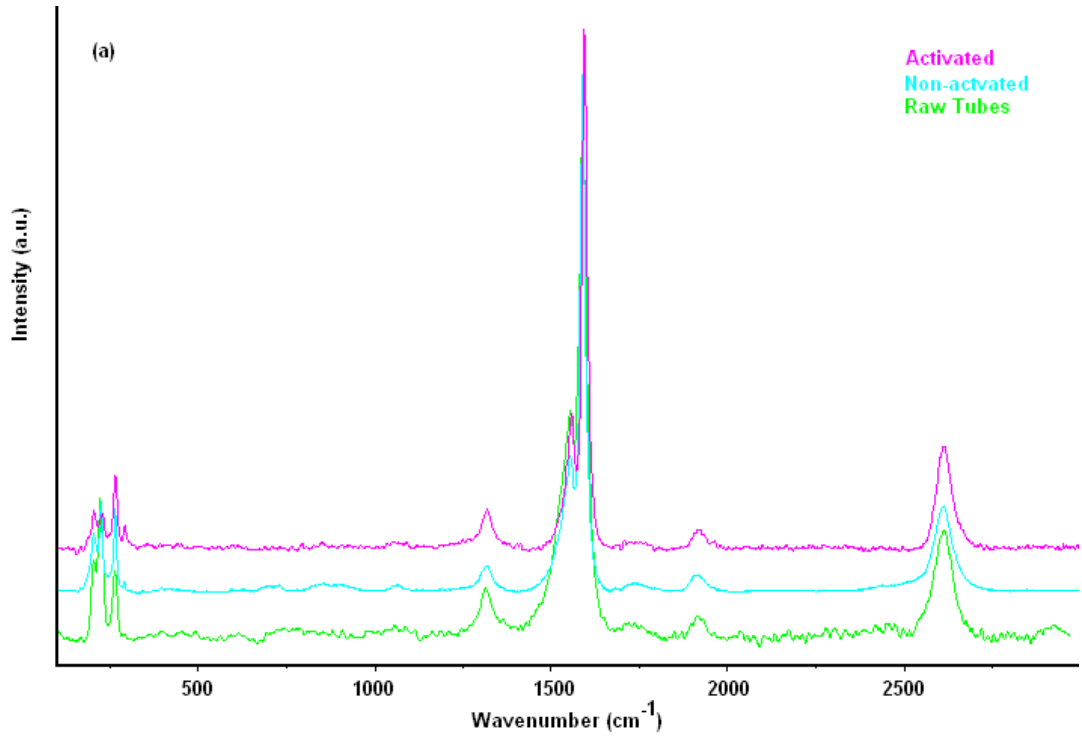

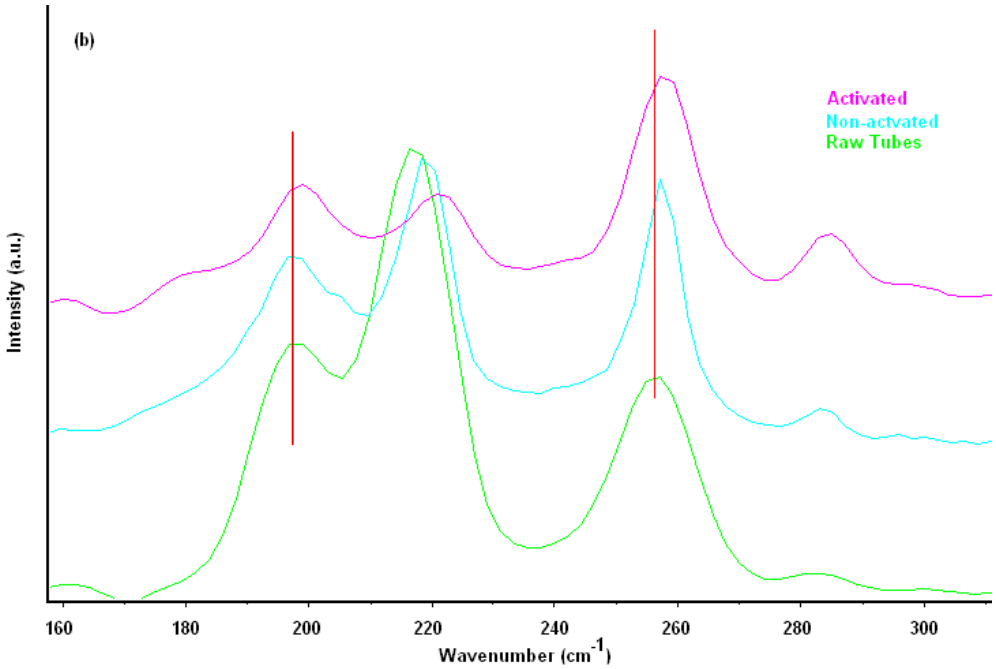

FIGURE 6.2: Effects of Slide Activation on 1.5 x 10^{-5} kg/L HiPco/ DCE solution at 633 nm (a)Stokes Spectra (b) RBM region

A difference between the activated and non-activated slides was found at all concentrations. The conclusion was that activation of the slides does to some extent keep the tubes debundled when the solvent has dried off. It should however be noted that some rebundling may take place.

6.3 Raman Spectroscopy Using Activated Slides of HiPco Tubes

Dispersions of single walled carbon nanotubes in DCE were made by adding 2 mg of tubes to 20 mls of the solvent as described in chapter 5. Again two different types of tubes were used in this study, HiPco and arc discharge. A series of activated slides were prepared in the manner described in section 6.2. Samples were then drop cast from each of the dispersions. A series of Raman spectra were taken at different points along the slides. Although there was some point to point variation there was a consistency in the spectral shape and

frequencies. Multipoint averages, typically ten, were taken of both spectral frequencies and intensity ratios. As the activation of the slides minimises re-aggregation it is expected that the aggregation state of the nanotubes on the slides is representative of that in the dispersion. In the following discussion concentration is used to refer to that of the initial dispersion, in line with common practice in the literature[4][5][6]. Following the analysis of chapter 4, the positions of the characteristic G^+, G^-, D and G^*-lines and RBMs were noted and ratios of the intensities of the lines to each other were calculated. Following the observations of chapter 5, in which discontinuities in the rate of change of both the absorption co-efficient and scattering with concentration were observed, the data are analysed in terms of discontinuities as a function of concentration at similar points.

As discussed in chapter 3, and described by equation 3.21 and 3.22, debundling of single walled nanotubes causes upshifting of the RBMs. Figure 6.3 shows the anti-Stokes and Stokes RBM spectra for raw HiPco nanotubes and the 6.25 x 10^{-6} kg/L dispersion, at which concentration the tubes are debundled.

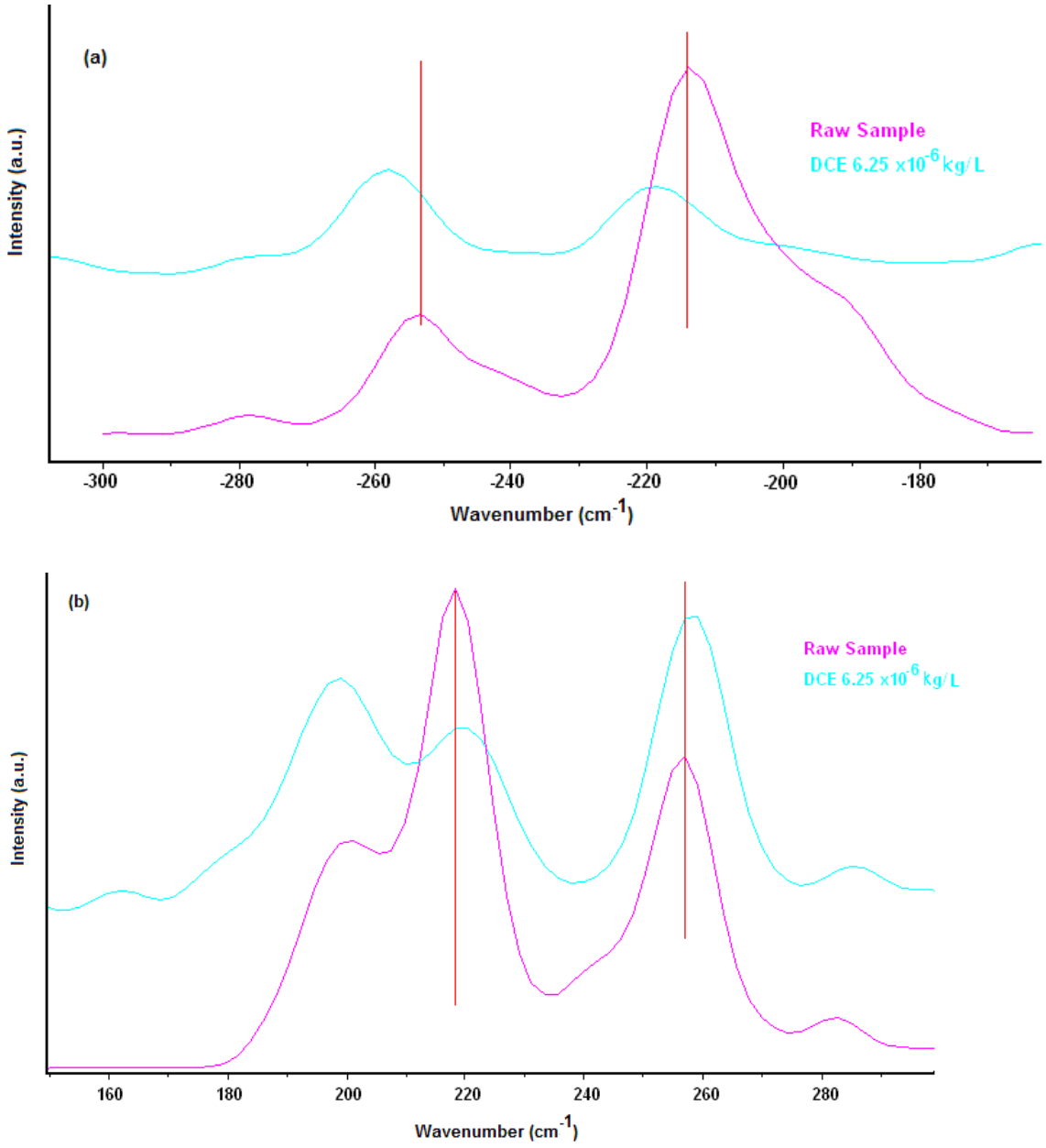

FIGURE 6.3: (a) anti-Stokes (b) Stokes RBM 633nm spectra for raw tubes and 6.25 x 10^{-6} kg/L dispersion

Both spectra show an upshift in the RBM spectra for the dispersion. Phonon frequencies are proportional to $(k/m)^{1/2}$[7], where k is the spring constant (or bond strength) and m is the effective mass of the molecule in question. Therefore an upshift in all characteristic lines would be expected if debundling has occurred since the effective mass of individual tubes is smaller than that of

bundles giving rise to higher line frequencies. Comparing the fitted Stokes RBM spectra at this concentration, figure 6.4, with that of the raw sample, chapter 4 figure 4.6, it is observed that the peaks are up shifted on average by 2 cm^{-1}, in all but one case, confirming the debundling observed in chapter 5[8][9].

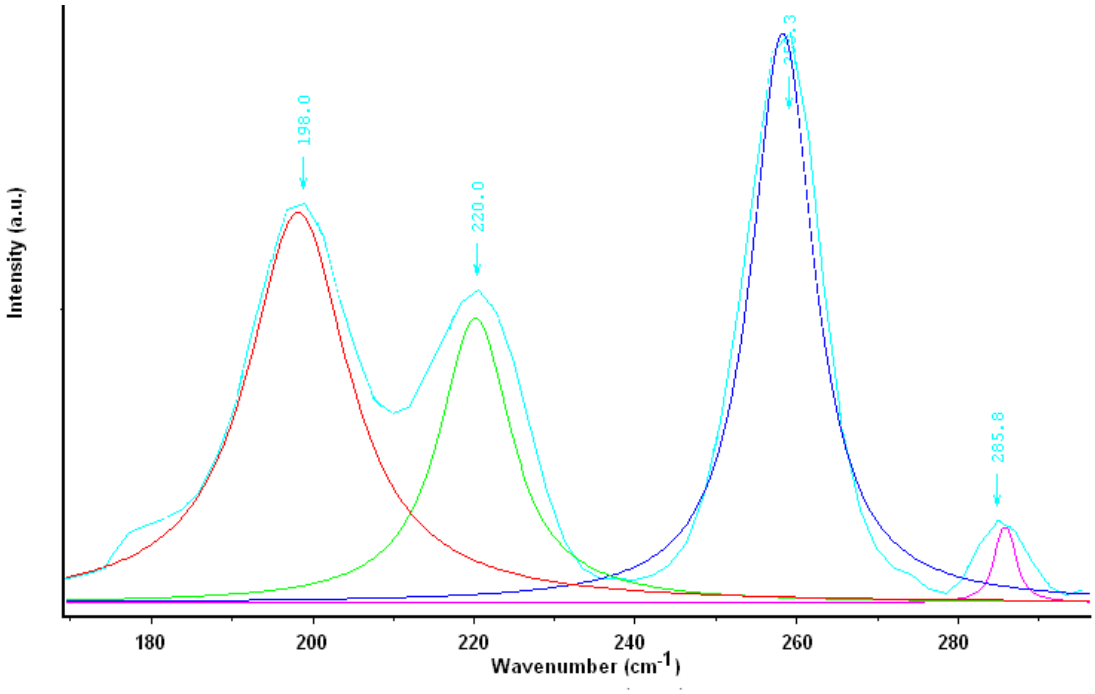

FIGURE 6.4: Fitted Stokes RBM spectra at 633nm for 6.25 x 10^{-6} kg/L DCE/HiPco dispersion

The four main characteristic peaks were fitted for each concentration. Figure 6.5 shows the fitted G^+ and G^- peaks as a function of concentration. The red box indicates those concentrations below the dispersion limit.

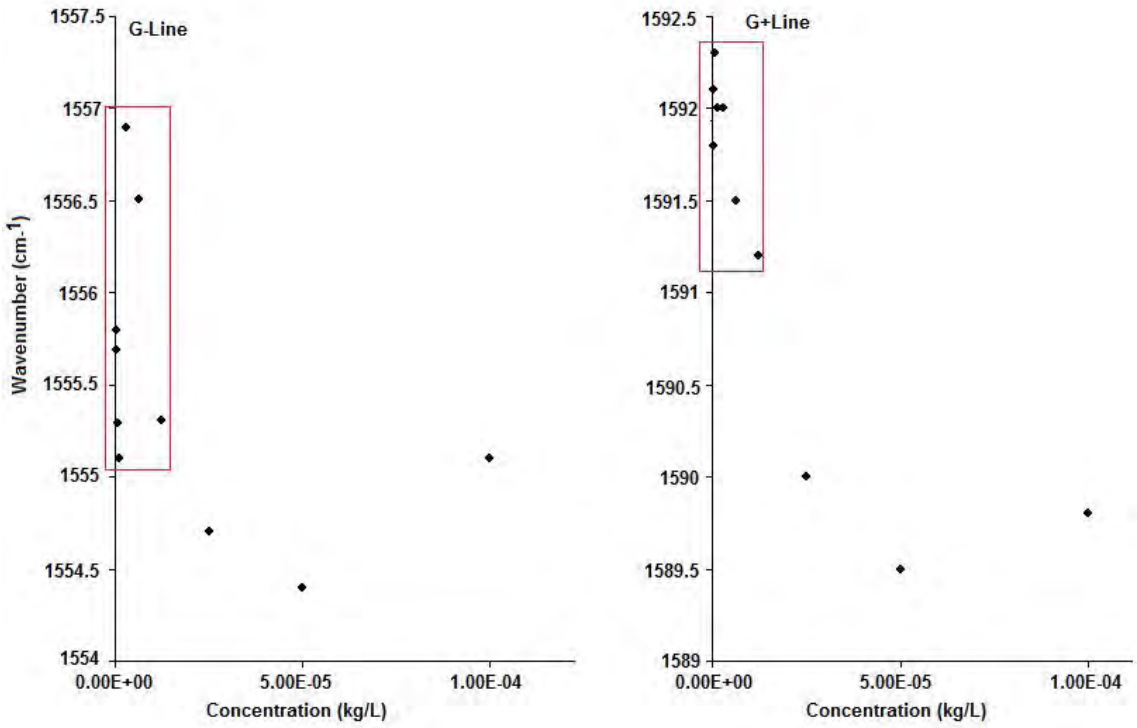

FIGURE 6.5: Characteristic G^- and G^+ lines respectively for HiPco tubes in DCE as a function of concentration at 633 nm

Recalling from chapter 4 that the position of the G^- and G^+- lines for HiPco tubes at 633 nm were 1549 cm^{-1} and 1586 cm^{-1}, it can be seen that for all concentrations there is an upshift for both lines. This is not unexpected below the dispersion limit as upshifting of characteristic lines can be accounted for by the change in the effective mass between that of bundled and debundled tubes. However what is unexpected is that this upshift is also observed at higher concentration. This upshifting can be interpreted as a change in the local environment possibly due to interaction with the substrate. The slow variation of the spectral positioning of both lines above the dispersion limit is reminiscent of the slowly varying absorption co-efficient in the same region, reproduced in figure 6.6 for comparison.

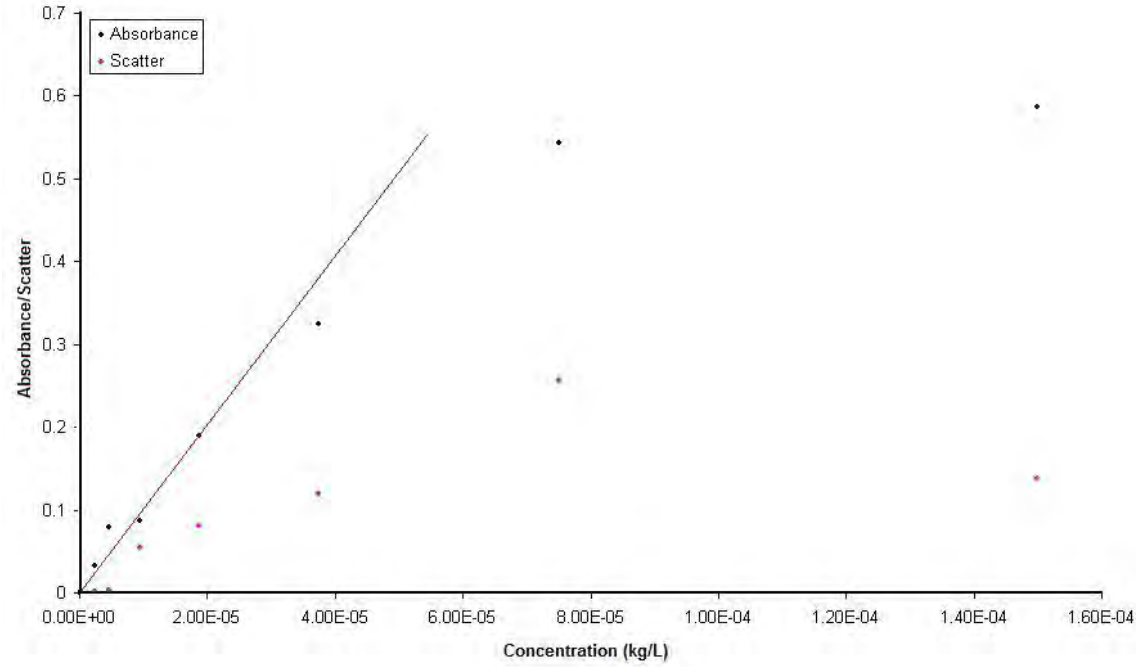

FIGURE 6.6: Absorbance/scatter DCE / HiPco dispersions taken at 700nm

In figure 6.5, most noticeably, there is a clear discontinuity at the dispersion limit. The spectral positioning of both lines significantly shifts to a lower wavenumber, by up 2.5 cm^{-1} for the G^--line and 2 cm^{-1} for the G^+-line. The behaviour in this region appears complex, however, as at the lowest concentrations the peaks reverse shift, a response which is not understood. The abrupt shifting in the region of the dispersion limit, however, can be designated a signature of the debundling process. The average value of $\Delta\omega_G$ is 36 cm^{-1} for debundled tubes compared with 39 cm^{-1} for raw samples indicating a reduction in bundle size.

Figure 6.7 shows the concentration dependence of the D and G*-lines.

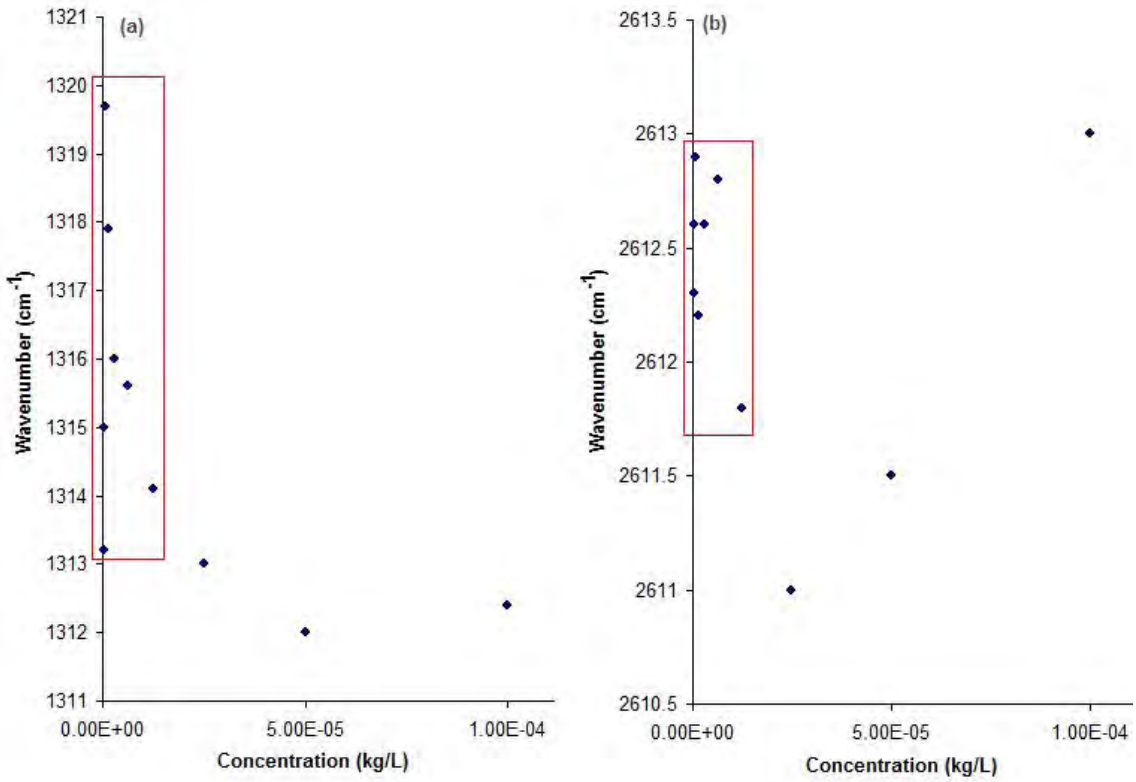

FIGURE 6.7: Characteristic (a) D line (b) G* line for HiPco tubes in DCE as a function of concentration at 633 nm

The D and G*-lines of raw HiPco tubes at 633 nm as measured in chapter 4 were found to be 1308 cm^{-1} and 2605 cm^{-1} respectively. As with the G-lines there is an upshift in both the D and G*-lines at all concentrations. Again a slow variation of the spectral positioning of both lines to lower wavenumbers, is observed above the dispersion limit. Again anomalous behaviour is observed at high and low concentrations. The spectral positioning of both lines significantly shifts by up to 7 cm^{-1} for the D-line and 2 cm^{-1} for the G^{*}-line. The D-line seems more sensitive to change at low concentrations.

The FWHM value of the D-line was measured as 33 cm^{-1} for debundled tubes compared with 45 cm^{-1} for raw samples. This reduction in FWHM values was

also observed for the G*-line which measured 48 cm^{-1} for debundled tubes compared with 60 cm^{-1} for raw samples. Narrowing of the D and G*-lines is indicative of debundling, as previously mentioned in chapters 3 and 4.

In summary, examination of the concentration dependence of all the characteristic lines shows an upshift in their value for all concentrations. There is a transition in behaviour below the dispersion limit demonstrating that this transition in behaviour may be used as a signature of substantial debundling and single tube behaviour. The values of $\Delta\omega_G$ and the FWHM values for the D and G*-lines are smaller in value than in the case of bundled tubes. This is indicative of debundling.

The ratios of the relative intensities of the characteristic lines at 633nm for HiPco tubes were also measured. Figures 6.8 and 6.9 show some of these ratios. Again values of the ratios below the dispersion limit of 2.00±0.5 x 10^{-5} kg/L are shown in the red boxes. For comparison purposes the values for the raw tubes are shown in table 6.1.

	G^+/G^-	G^+/G^*	G^-/G^*	G^+/D	G^-/D	G^*/D
Raw	2.7 ± 0.3	5.59± 0.5	2.06 ± 0.15	18.84 ± 4.0	6.97 ± 2.0	3.38 ± 1.2

TABLE 6.1: The intensity ratios at 633 nm for raw samples

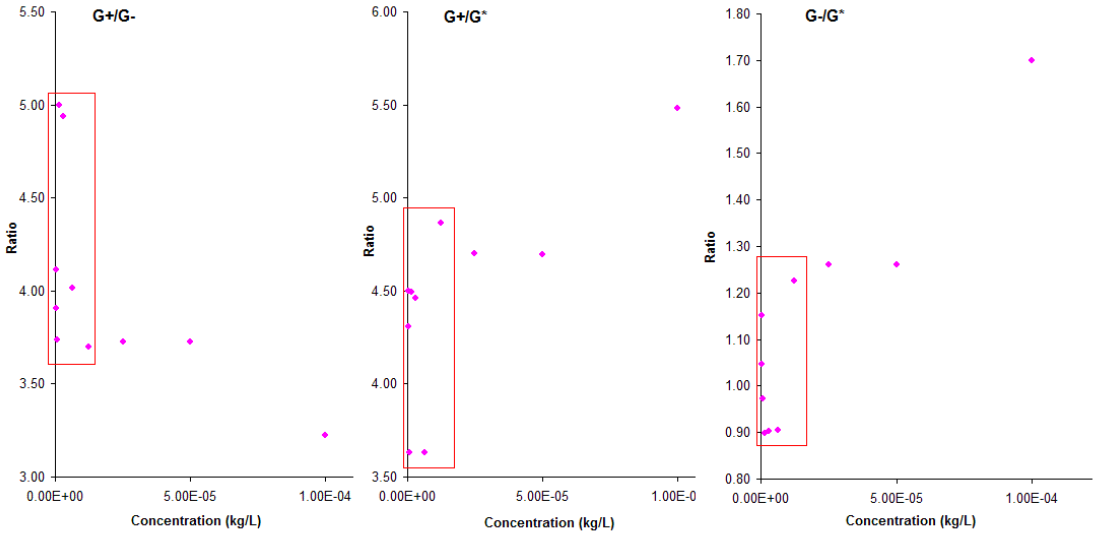

FIGURE 6.8: Ratios of G^+/G^-,G^+/G^* and G^-/G^* as a function of concentration for HiPco DCE dispersion at 633 nm

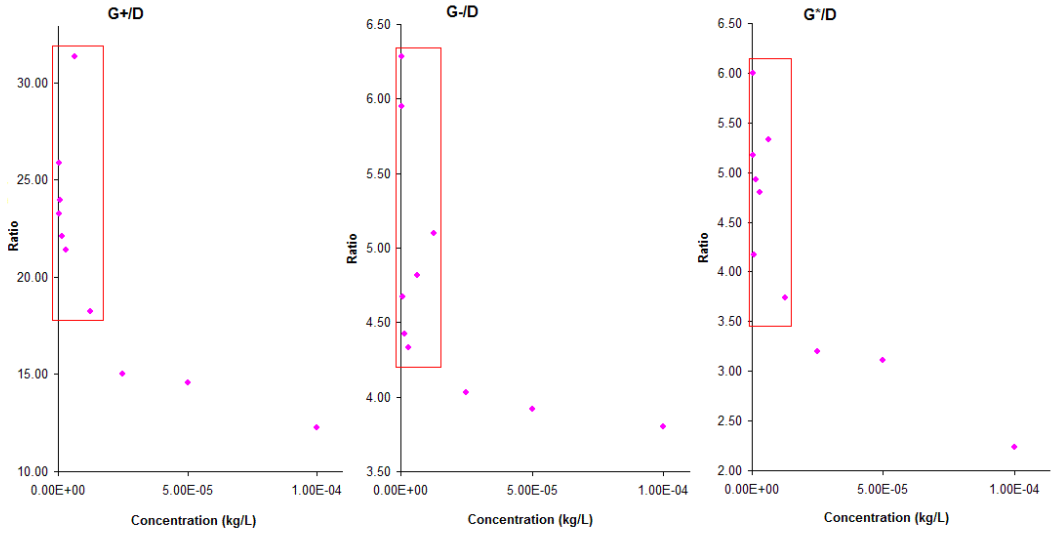

FIGURE 6.9: Ratios of G^+/D,G^-/D and G^*/D as a function of concentration for HiPco DCE dispersions at 633 nm

From figure 6.8 it can be seen that there are discontinuities at the dispersion limit for all three ratios. The other thing to notice is that at high concentrations the ratios approach those of the raw samples (table 6.1) The absolute value of the G^+/G^- ratio increases with decreasing concentration whereas the values of the G^+/G^* and G^-/G^* decrease. This would indicate that the relative intensity of

the G^--line is reduced with debundling. In the case of the ratios involving the D-line intensity values, figure 6.9, the picture is not as clear. Although all three ratios again show discontinuities at the dispersion limit, there is a significant difference between the high concentration values and those observed for the raw samples. All three ratios increase in value with decreasing concentration due to a relative decrease in the D-line intensity values. This reduction occurs for all concentrations.

Raman spectroscopy of the same samples taken at 514.5 nm shows similar results. The RBM spectra again show upshifting of the spectra indicating debundling as seen in figure 6.10.

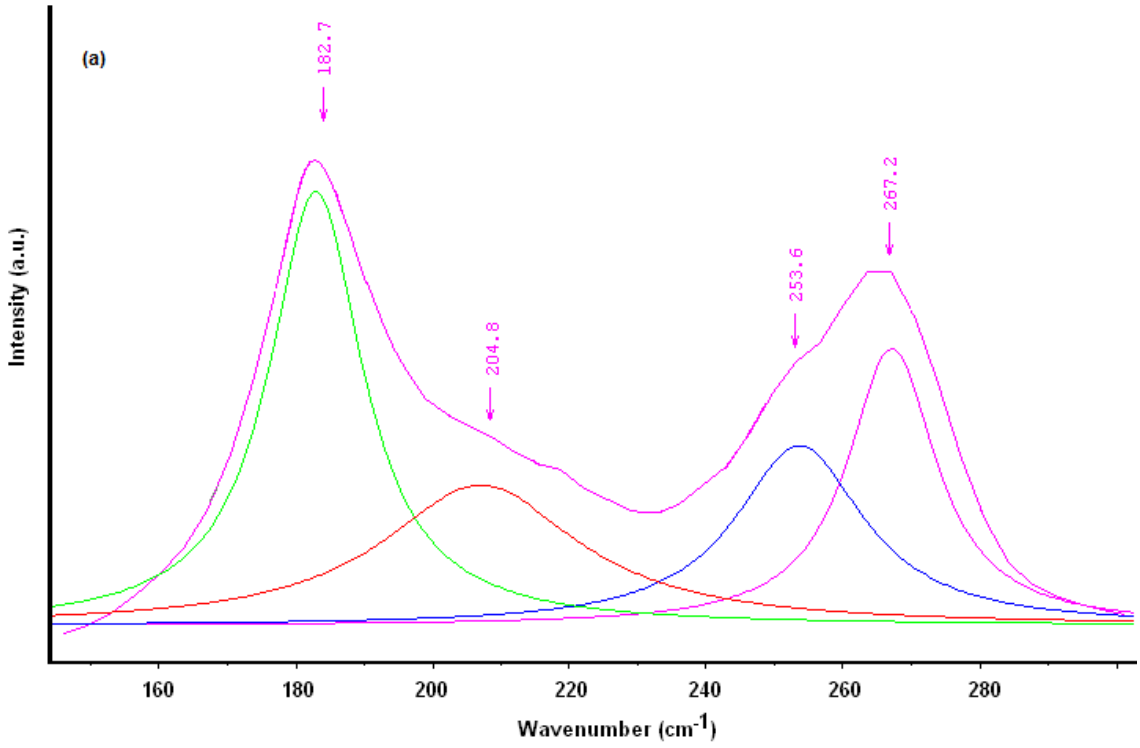

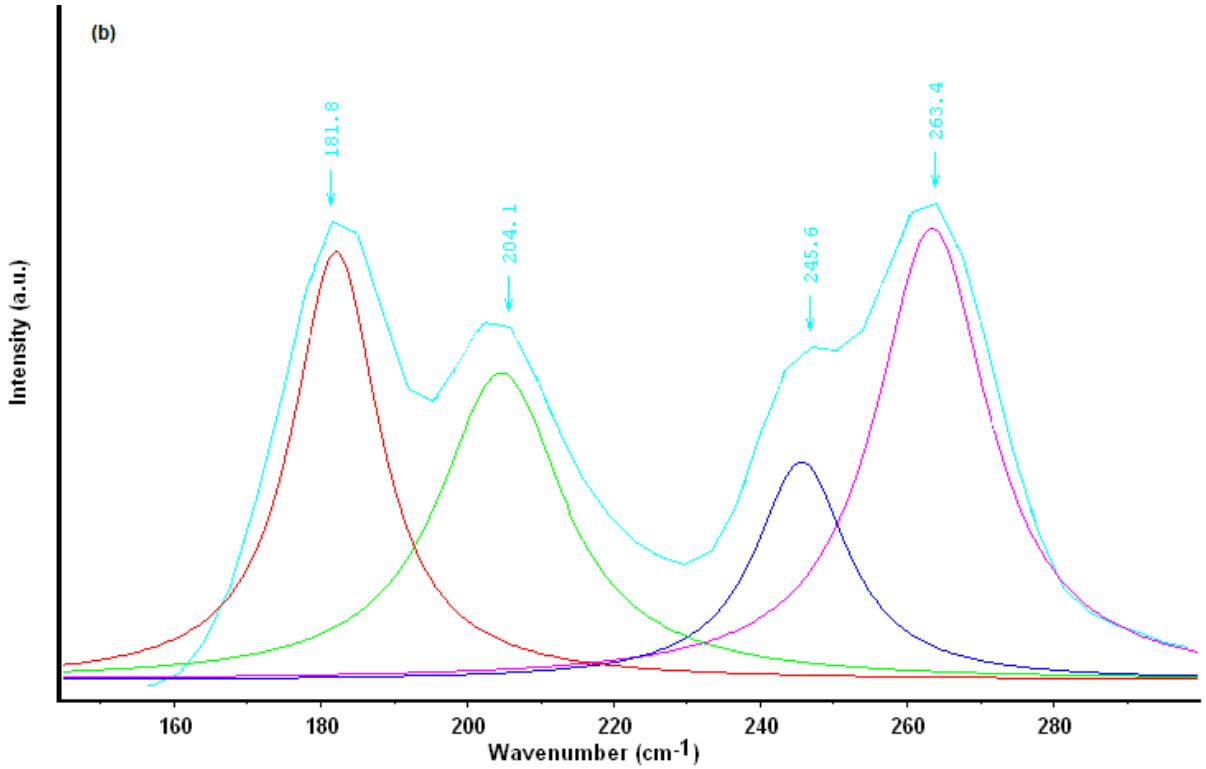

FIGURE 6.10: Fitted Stokes RBM Spectra at 514.5 nm for (a) 6.25 x 10^{-6} kg/L DCE/HiPco dispersion (b) raw sample

The resolved spectra for raw tubes and concentration 6.25 x 10^{-6} kg/L show upshifts of between 1 cm^{-1} and 4 cm^{-1}. In chapter 4 it was shown that the RBMs at 181.8 cm^{-1}, 204.1 cm^{-1} and 245.6 cm^{-1} correspond to the (10,10), (13,4) and (10,4) metallic tubes, calculated using equation 3.14 for bundles. Using equation 3.22 for isolated tubes, the upshifted peaks at 182.7 cm^{-1}, 204.8 cm^{-1} and 253.6 cm^{-1}, can be shown also to be the (10,10), (13,4) and (10,4) metallic tubes. This means that the same metallic tubes are still present but are now in a debundled state.

All the characteristic lines upshift as in the case of the 633nm laser line. The G^{+}-line shifts from 1589 cm^{-1} for raw tubes to 1591 cm^{-1} at a concentration of 5.00 x 10^{-5} kg/L to 1595 cm^{-1} at 6.25 x 10^{-6} kg/L. This shift pattern is mirrored for the

G*-lines although the shifts are slightly bigger going from 2656 cm^{-1} for raw tubes to 2665 cm^{-1} for a concentration of 6.25 x 10^{-6} kg/L. The D-line shifts by 4 cm^{-1} when the tubes have been debundled. As shown in chapter 4 the 514.5 nm spectrum for these tubes is in fact of metallic character.

From figure 11 it can be seen that there is a decrease in the intensity and the width of the G^--line.

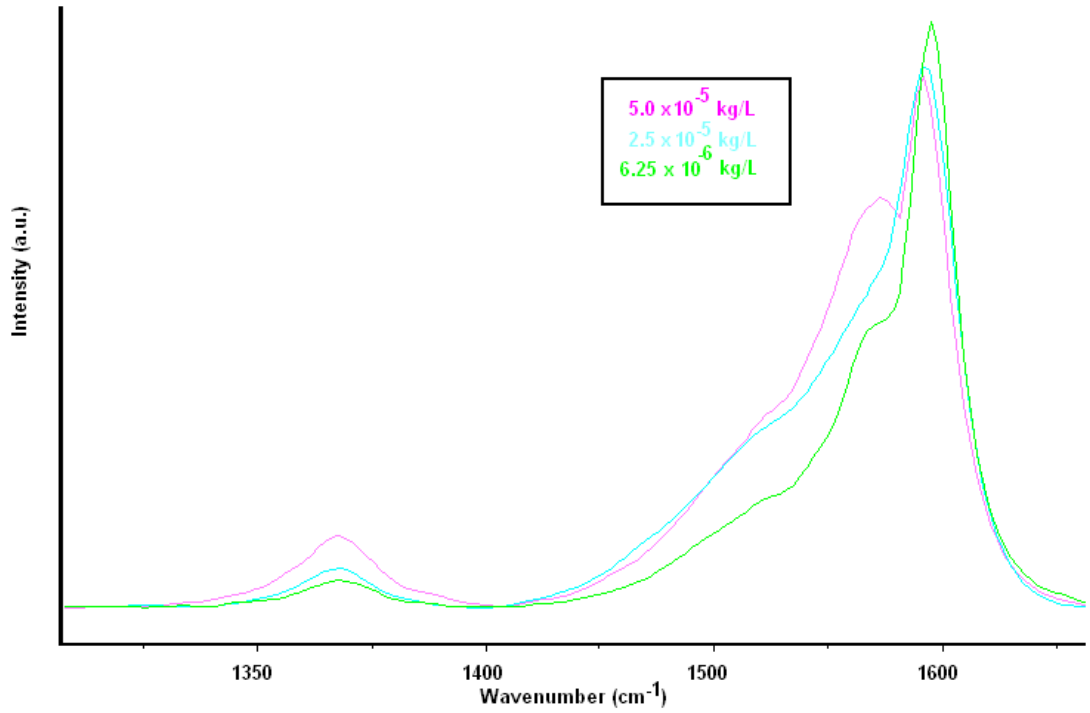

FIGURE 6.11: D and G-Lines for three HiPco/DCE solutions at 514.5 nm

This, as discussed in chapter 3, is to be expected as the intensity and width gets smaller for a decrease in bundle size[10] due to loss of electron-phonon coupling[10]. For the 6.25x10^{-6} kg/L, the G^--line has lost its characteristic metallic shape and resembles more closely that of a semiconducting character. However from the RBM discussion above it is clear that the metallic tubes are still there. This is confirmation that the loss of metallic character in the G-line is in fact due to reduced bundle size and not to the loss of metallic tubes. This

would be consistent with the notion, as discussed in chapter 3, that the characteristic Breit-Wigner-Fano lineshape is in fact only associated with metallic bundles and disappears when the tubes are debundled[11] . So clearly narrowing of the G^--line and loss of the Breit-Wigner-Fano lineshape is indicative of debundling of metallic tubes.

Again the intensity ratios of the characteristic lines were calculated and the values are shown in figure 6.12. The ratios involving the G^--line are omitted as the broad G^- is difficult to measure in metallic line shapes.

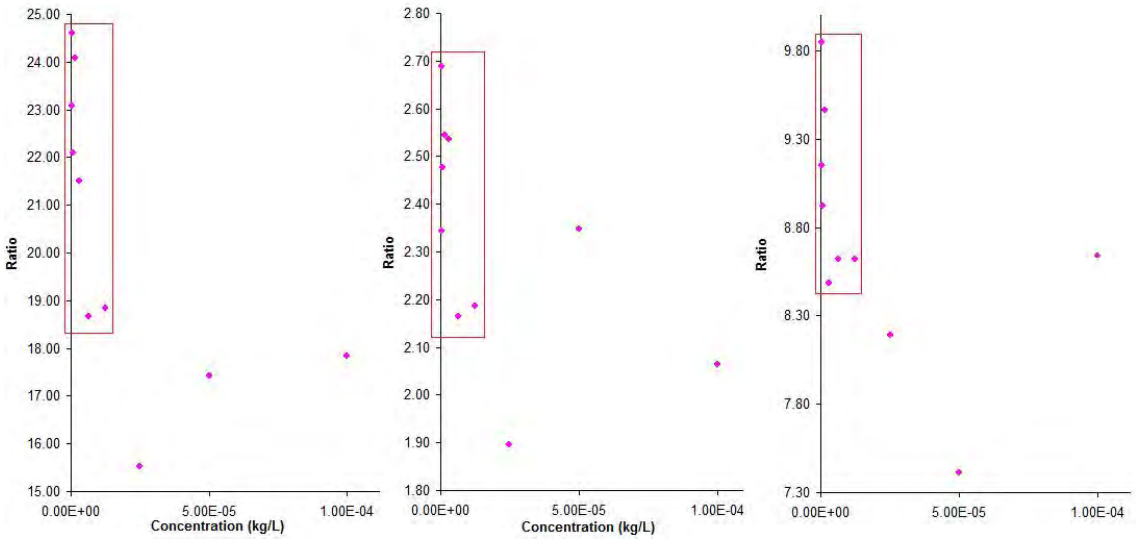

FIGURE 6.12: Ratios of G^+/D, G^+/G^* and G^*/D as a function of concentration for HiPco DCE dispersions at 514.5 nm

As at 633 nm there is an increase in the G^+/D ratio with decreased bundle size. The values of this ratio at 514.5 nm would appear to be similar to the 633 nm values indicating a decrease in the relative intensity of the D-line with debundling. The G^+/G^* values are smaller at 514.5 nm due to the large G* line observed for metallic spectra. Upon further investigation, by normalizing the G^+-lines, it was discovered that the relative size of the large G* decreases with

debundling at 514.5 nm, figure 6.13. This does not happen at 633 nm where the relative size of the G*-line remains unchanged. This indicates that there is an element of electron-phonon coupling associated with the G*-line, the intensity of which decreases with bundle size.

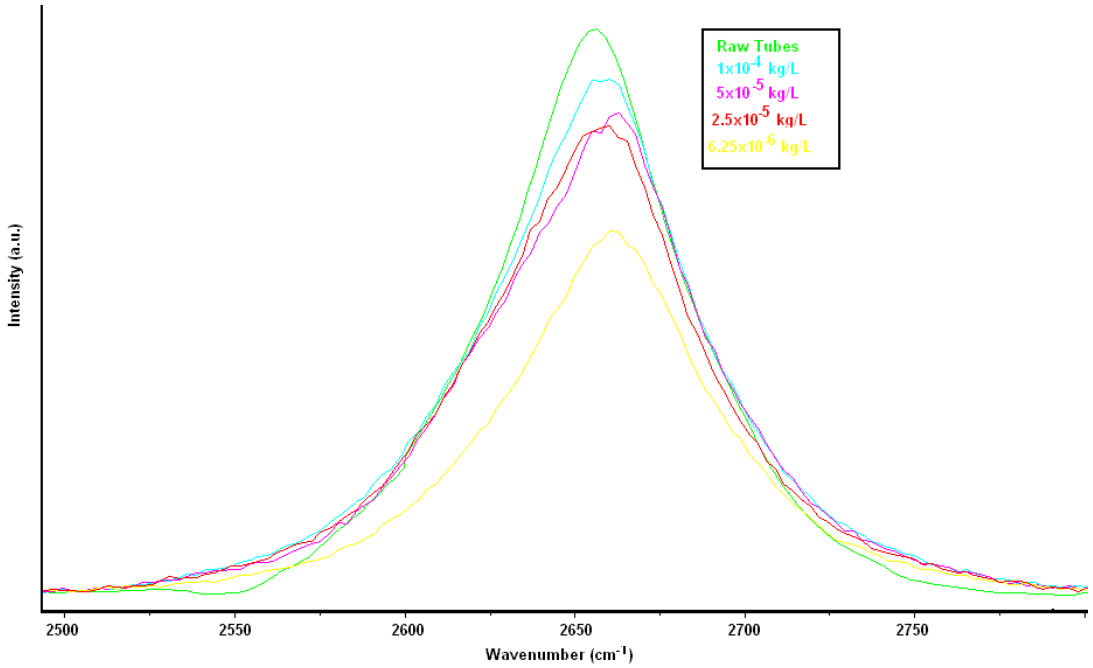

FIGURE 6.13: Relative change in the G*line with decreasing concentration for HiPco DCE dispersions at 514.5 nm. The yellow curve, 6.25 x 10^{-6} kg/L is below the dispersion limit

In summary, in addition to the accepted upshifts in the RBMs being indicative of debundling, it has been shown that upshifts also occur in all the characteristic lines. The upshifts occur abruptly in the regions of the dispersion limit. This occurs regardless of the excitation energy used. When debundling occurs there is a narrowing and eventual loss of the Breit-Wigner-Fano lineshape associated with metallic nanotubes. The same tubes are identifiable in both the bundled and debundled state, albeit with a revised formula. It has also been shown that discontinuties in the ratios of the characteristic line intensities is also indicative of debundling. Similar trends were seen at 514.5 nm to those seen at 633 nm.

However the changes are more pronounced for the metallic 514 nm spectra. Reduction in the relative size of the G*-line in metallic spectra also indicates debundling.

6.4 1, 2- Dichloroethane (DCE) – Arc Discharge Tube Solutions

The same procedure was carried out with arc discharge tubes. This was important to make sure that the simple indicators outlined in section 6.4 could be repeated with a different tube type.

Similar trends were observed in relation to characteristic peak positional changes and peak intensity ratios with respect to the dispersion limit as calculated from absorption spectroscopy. A comprehensive presentation of the results will not be made here but some representative data follows to illustrate the transferability of the discussion presented in section 6.3.

The dispersion limit calculated for arc discharge tubes in DCE was 2.00 ± 0.5 $x10^{-5}$ kg/L. Figure 6.14 shows the change in G* and D positions for the tubes at 514.5 nm. These tubes as shown in chapter 4 are semiconducting at 514.5 nm. Again the data within the red box is for concentration values below the dispersion limit.

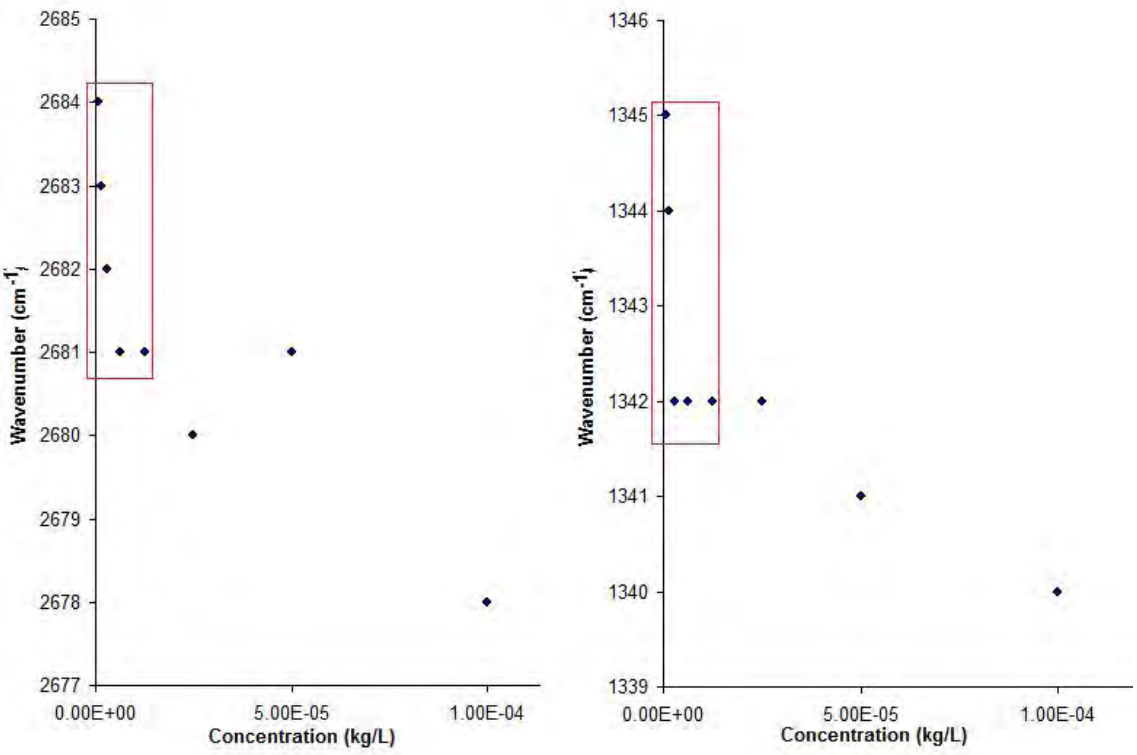

FIGURE 6.14: Characteristic G* and D lines on the left and right respectively for arc discharge tubes in DCE as a function of concentration at 514.5 nm

As before there is a shift in the line positions from the raw tube values of 2670 cm^{-1} for the G*-line and 1338 cm^{-1} for the D-line at all concentrations. These shifts are also seen in the G^+ and G^--lines. Ratios of the six characteristic line intensities are plotted in figures 6.15 and 6.16.

Discontinuities are again observed at the dispersion limits. With the exception of the G^+/G^- ratio, the same trends can be seen in the concentration dependence of the ratios as those observed for the HiPco tubes.

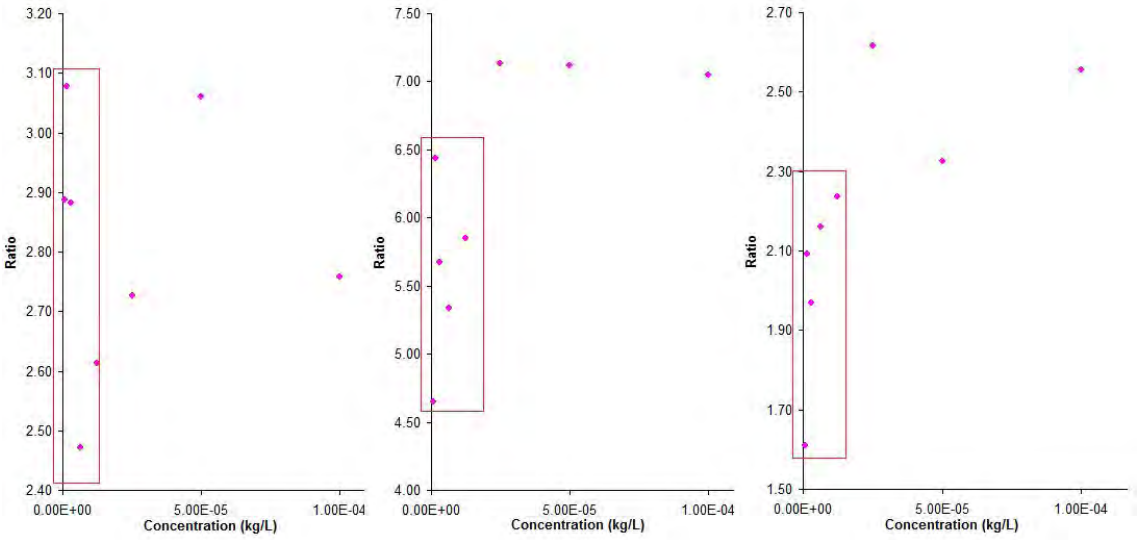

FIGURE 6.15: Ratios of G^+/G^-,G^+/G^* and G^-/G^* as a function of concentration for arc discharge DCE dispersions at 514.5 nm

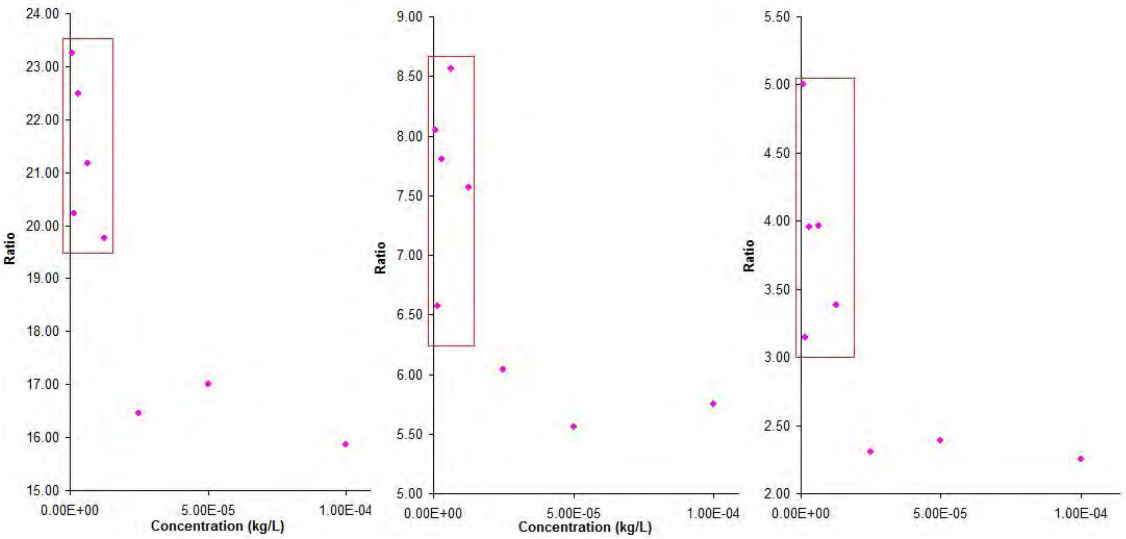

FIGURE 6.16: Ratios of G^+/D,G^-/D and G^*/D as a function of concentration for arc discharge DCE dispersions at 514.5 nm

As pointed out in chapter 4, the arc discharge tubes show a metallic signature at 633 nm. Again the ratios of the characteristic lines are consistent with those in 6.3 above. The loss of the Breit-Wigner-Fano lineshape with debundling and

the reduction in the relative value of the G*-line observed in 6.3 above are also observed, figure 6.17.

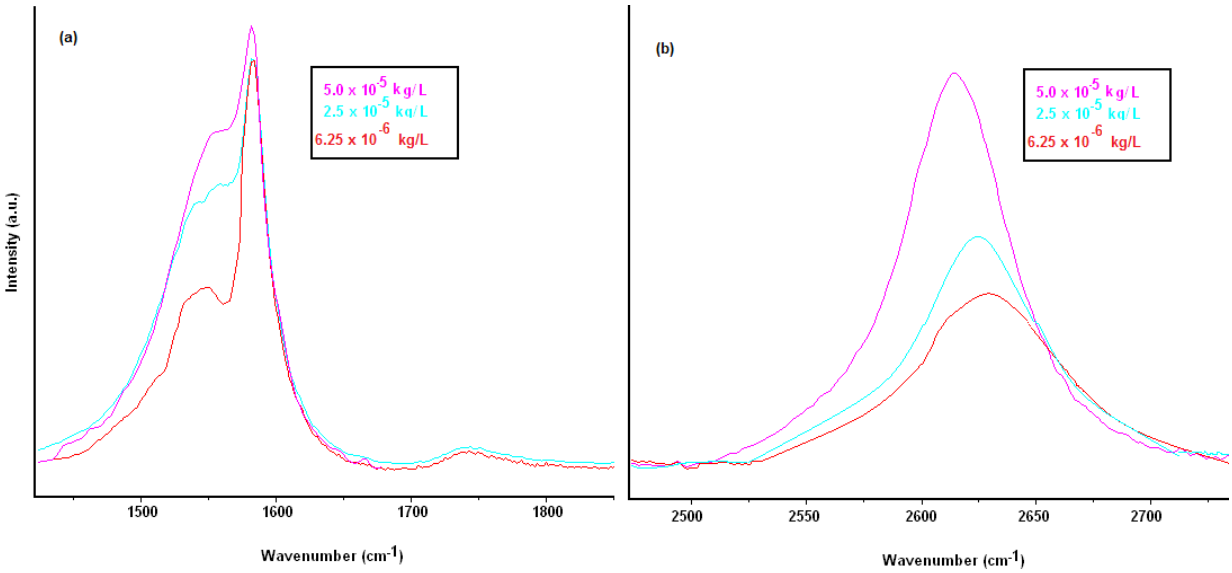

6.17: (a) G+ (b) G* lines for three arc discharge DCE solutions at 633 nm

In summary upshifts are seen in all characteristic lines upon debundling. Loss of the metallic Breit-Wigner-Fano lineshape is observed for debundled tubes at 633 nm. Discontinuties in the intensity ratios are observed at the dispersion limit. For the metallic tubes the G*-line intensity is reduced with debundling. In short all the observations made for the HiPco tubes universally apply to the arc discharge tubes.

6.5 Summary

In this chapter Raman spectroscopy was shown to confirm the debundling measured in chapter 5 using absorption spectroscopy, TEM and AFM by measuring shifts in the RBMs, a generally accepted method. Furthermore it was

found that not only do all the characteristic lines also upshift but there are discontinuities in the degree of shifting at the dispersion limits measured in chapter 5. The fact that some degree of shifting is observed at all concentration levels suggests that Raman is more sensitive to small changes in bundle size than absorption spectroscopy. A novel approach using the ratios of the characteristic line intensities was also shown to exhibit discontinuities at the dispersion limit. Loss of the Breit-Wigner-Fano lineshape and a reduction in the relative size of the large G*-line in metallic Raman spectra were also shown to be the result of debundling.

All of these measurements are easily and quickly made compared to such techniques such as TEM or AFM. Many deductions can be made from just one spectrum and the degree of analysis required to estimate debundling, is small. The observations and analysis indicate that Raman spectroscopy could be employed as a high throughput technique, involving relatively low capital costs, for the analysis of the aggregation state of SWNT's. Some of these techniques will be used in chapter 7 to explore some of the fundamental physical properties i.e. temperature dependence, of single walled carbon nanotubes both bundled and debundled.

6.6 References

[1] P.Baskar, H.J.Byrne J.Phys.Chem.C **112**, 332 (2008)

[2] M.Burghard, G.S.Duesberg, G.Philipp, J.Munster, S.Roth, Adv. Matter **10,** 584 (1998)

[3] A.M.Rao, J.Chen, E.Richter, U.Schlecht, P.C.Eklund, R.C.Haddon, U.D.Venkateswaran, Y.K.Kwon, D.Tománek, Phys.Rev. Lett. **86,** 17 (2001)

[4] T.G. Hedderman, S. M. Keogh, G.Chambers, H.J. Byrne, J. Phys. Chem. B, **110,** (9): 3895-3901 (2006)

[5] S.M. Keogh, T.G Hedderman, P Lynch, H.J Byrne J. Phys. Chem. B, **110,** (39): 19369-19374 OCT 5 (2006)

[6] A. Casey, M. Davoren, E. Herzog, F.M. Lyng, H.J. Byrne and G. Chambers, Carbon **45**, 34–40(2007)

[7] E.Smith, G.Dent *Modern Raman Spectroscopy – A Practical Approach* Wiley and Sons (2005)

[8] M.Milnera, J.Kűrti, M.Hulman, H.Kuzmany Phys.Rev. Lett. **84,** 1324 (2000)

[9] A.Jorio, R.Saito, J.H.Hafner, C.M.Lieber, M.Hunter, T.McClure, G.Dresselhaus, M.S.Dresselhaus, Phys.Rev.Lett. **86,** 1118 (2001)

[10] C.Jiang, K.Kempa, J.Zhao, U.Schlecht, U.Kolb, T.Basché, M.Burghard and A.Mews Phys. Rev. B,**66**, 161404 (2002)

[11] M.Paillet, P.Poncharai, A.Zahab, J.L.Sauvajol Phys. Rev. Lett. **95,** 237401 (2005)

CHAPTER 7

TEMPERATURE DEPENDENT RAMAN SPECTROSCOPY OF SINGLE WALLED CARBON NANOTUBES

7.1 Introduction

In chapter 6 it was shown that Raman spectroscopy could be used as a simple, quick, and relatively cheap method for studying the structure and nature of single walled carbon nanotubes. In chapter 7, following on the need to understand the fundamental properties of nanotubes, Raman spectroscopy will be used to study the behaviour of single walled nanotubes as a function of varying temperature and the behaviour observed for bundles of the raw nanotube samples will be compared to that observed for nanotubes dispersed using DCE as described in chapters 5 and 6. Electron-phonon coupling in carbon nanotubes is a key parameter in the electronic band structure as it controls not only Raman scattering[1] but also is the origin of resistance[2], thermal conductivity and sets the ultimate limit to high field ballistic transport[3][4]. A study of the temperature effects on the Raman spectra can provide important insights into the relationship between the spectra, electronic state distribution and structure of single walled carbon nanotubes as outlined in chapter 3.

7.2 Experimental Apparatus

The temperature dependent study for each carbon nanotube sample was carried out by attaching a Linkam THMS600 heating and cooling stage (figure 7.1) to the Raman microscope stage. This stage is capable of a 0.01K accuracy over the range 77 K to 873 K.

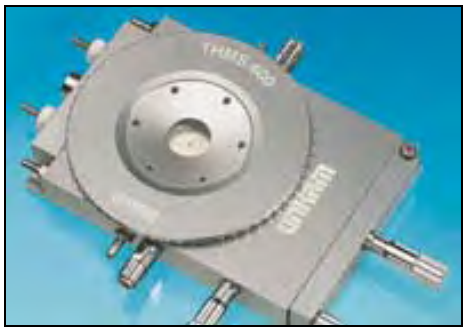

FIGURE 7.1: The Linkam Stage

The sample was placed on a 0.17 mm thick cover slip which in turn was placed on the highly polished silver heating element to ensure optimal heat transfer and extremely sensitive temperature measurement. A platinum resistor sensor, accurate to 0.01 K, was used to provide an accurate and stable temperature signal. The temperature was programmed by the Linksys software and controlled via a C194 computer interface controller. Rapid sample turnover, without compromising the accuracy of the temperature measurement, was achieved by heating to within a few degrees of the temperature of interest at a rate of 130 K /min then at a reduced rate of a few degrees a minute until the desired temperature was reached. To cool to sub-ambient temperatures, the LNP94/2 Cooling System was used. This system consisted of a control unit housing the pumps and a 2L Dewar for housing the liquid nitrogen required for cooling.

A schematic diagram of the Linkam unit and setup can be seen in figure 7.2[5].

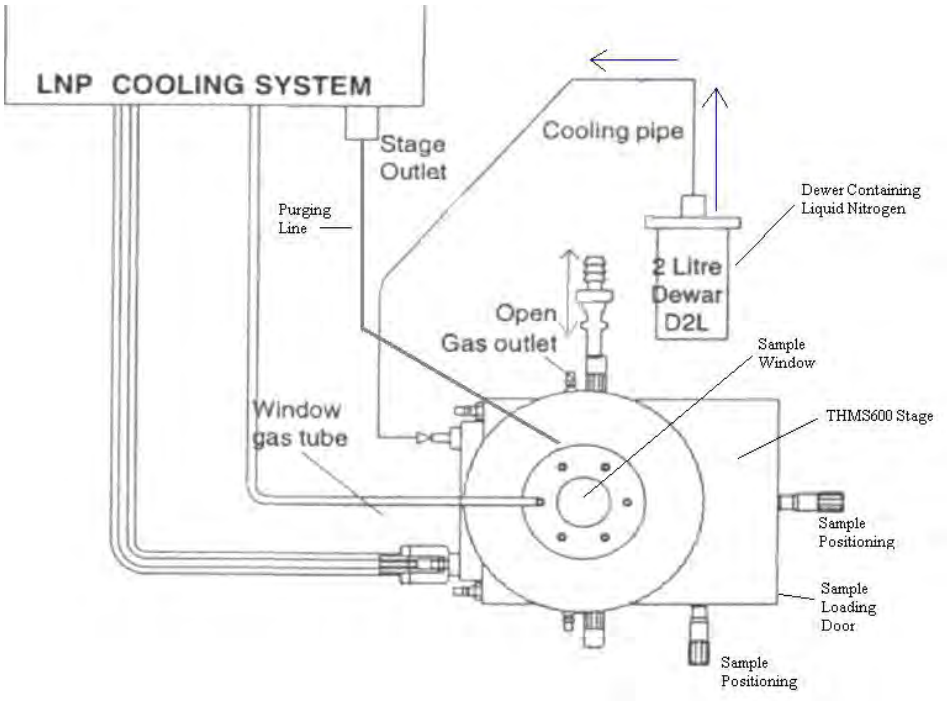

FIGURE 7.2: Schematic Diagram of Linkam Stage with LPN cooling system attached[5].

The ideal measurement conditions for use with the Raman spectroscopic microscope are depicted in figure 7.3.

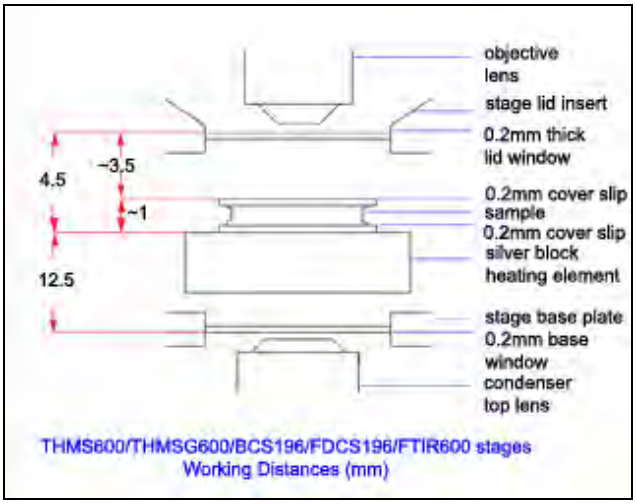

FIGURE 7.3: Working distances for the Linkam Stage[5]

The Linkam stage was placed directly beneath the Olympus BX40 microscope of the Raman Spectrometer ensuring that the sample window was directly beneath the objective lens. The stage was then clamped in place to prevent

movement once the pump was switched on. The LNP cooling system was then attached to the stage. The LNP connection was simply pushed into one of the cooling tubes on the stage. The 2 L Dewar was then filled with liquid nitrogen. The lid was placed on top of the Dewar before the liquid nitrogen stopped boiling. This prevented water vapour in the air condensing in the liquid nitrogen. The black capillary tube from the Dewar flask was then inserted into the second cooling tube on the stage. A white insulating tube surrounded the black capillary tube. This insulating tube was positioned over the stage cooling connection. The smaller tube, known as the purging line, was placed in position on top of the stage lid pointing at the sample window. This was used to de-mist the window and prevent further condensation. The temperature dependent study was carried out at 514.5 nm and 633 nm for HiPco and arc discharge tubes although results will only be presented for HiPco tubes.

7.3 Temperature Dependent Study of the Raman Frequencies of Bundled Single Walled Nanotubes

The nanotube samples used in this study were HiPco tubes purchased from Carbon Nanotechnologies Incorporated batch number P0288 (the same batch used in previous work described in chapters 4, 5 and 6). A small amount of the powdered sample was thinly spread on the small cover slide. It was then placed in the Linkam stage, as shown in figure 7.3. The temperature range used was 83 K to 523 K for the 633 nm study and 83 K to 343 K for the 514.5 nm study. Spectra were taken every 20 K in both cases.

Figure 7.4 shows the temperature dependence of the spectral positioning of the characteristic G^+ and G^- lines for raw HiPco tubes at 633 nm. The first thing to note is the upshift in the peaks at low temperatures compared to those observed at room temperature, evaluated in chapter 4, from 1586 cm^{-1} to 1590 cm^{-1} for the G^+ line and 1549 cm^{-1} to 1554 cm^{-1} for the G^- line. There is a steady shift in the peak positioning of both features as a function of temperature. The linear dependence of this shift is expected as previously described in chapter 3 equation 3.16 and the temperature coefficient of frequency is measured to be -0.023±0.004 cm^{-1}/K for both lines. $\Delta\omega_{G,}$ the difference in frequency between the G^+ and G^- lines, thus remains constant over the whole temperature range at 36 cm^{-1}, indicating no change in the bundling level of the sample.

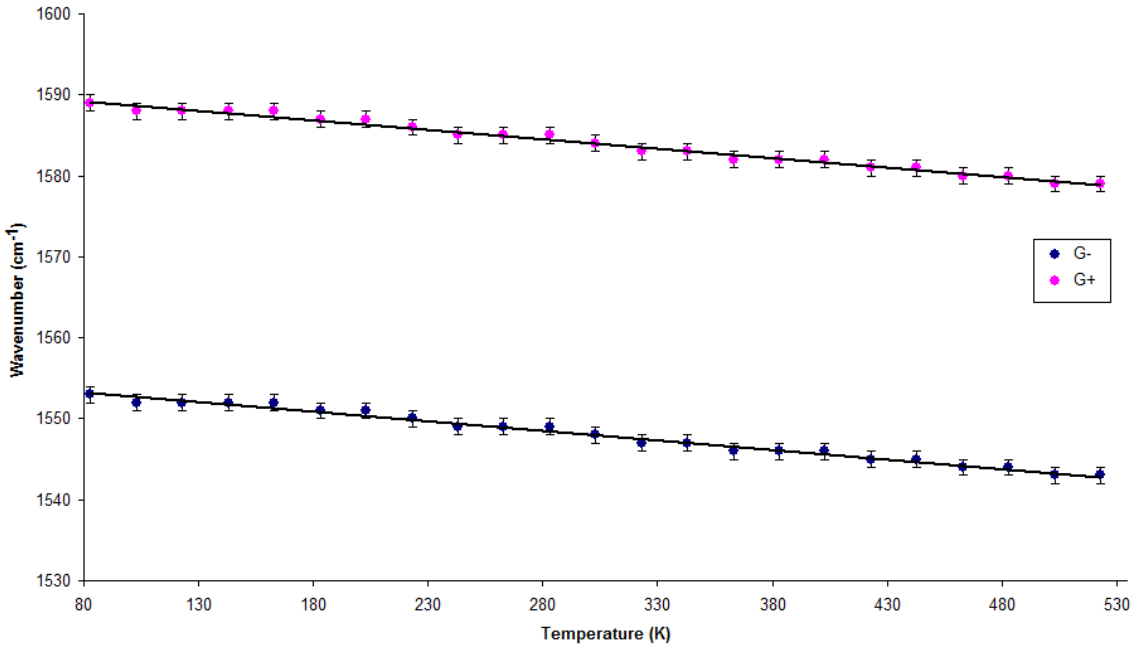

FIGURE 7.4: Temperature Dependent Raman for G^+ and G^- lines for Raw HiPco tubes at 633 nm

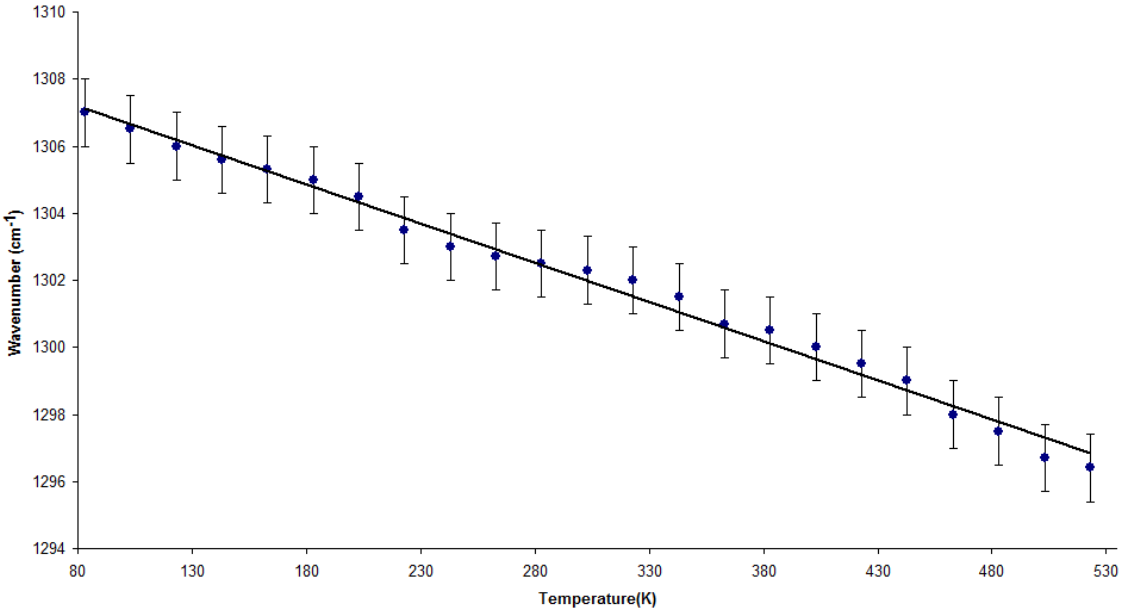

FIGURE 7.5: Raman Shift of D lines for HiPco tubes at 633 nm

The temperature dependence of the spectral positioning of the D-line is shown in figure 7.5. Again there is a continuous downshift of the peak with increasing temperature. The temperature coefficient of frequency of the D-line was calculated to be -0.024±0.005 cm^{-1}/K. The observed shifting of the G and D-lines is indicative of the behaviour of bundled tubes[6][7][8][9] and is due to competing effects of softening of the interatomic force constant due to thermal expansion of the C-C bonds and relaxation of the weak van der Waals interaction between SWNT's in bundles with increasing temperature[10]. The values of temperature coefficients measured are comparable to those previously measured[6][7][8][9][11]. Literature studies have shown the temperature coefficient of frequency of the D-line to be slightly smaller than that of the G-line. Within the error margins this could also be the case here.

The RBM spectral positions also change as a function of temperature, as seen in figure 7.6, which shows the RBM spectra from 83 K and 543 K. There is a

downshift of the peaks as the sample is heated. There is also a change in the relative intensities of each peak. This has been explained in chapter 3 to be due to the optical transition energies E_{ii} shifting with temperature[5][6].

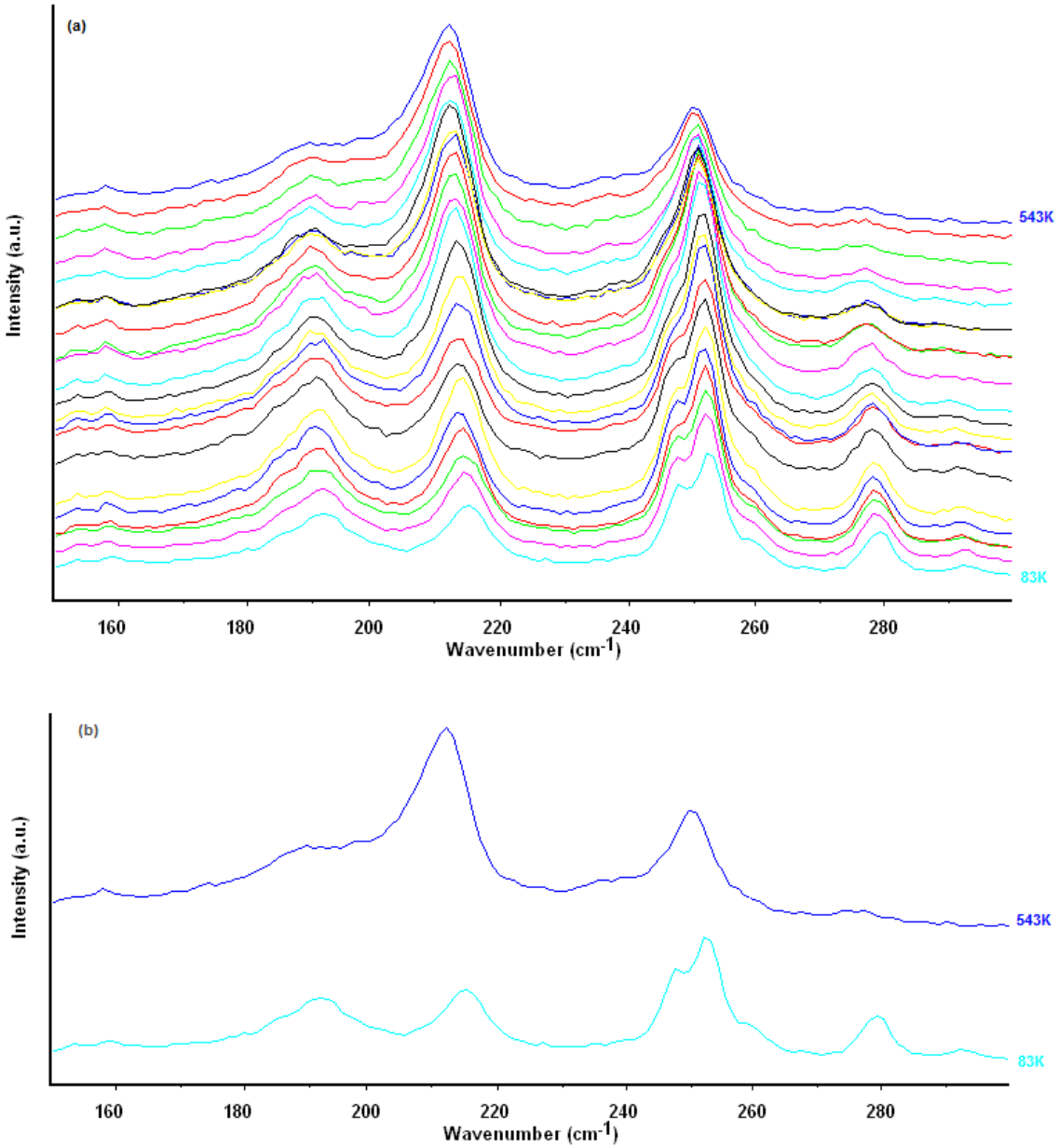

FIGURE 7.6: Stokes RBMs (a) over temperature range 83 K to 543 K (b) at 83 K and 535 K for HiPco tubes at 633 nm

When the RBM spectra are fitted, as seen in figure 7.7, the spectral downshifting is clearly seen. This spectral shifting is also seen in the anti-Stokes spectra, as shown in figure 7.8. In both the Stokes and the anti-Stokes spectra,

additional peaks become evident at higher temperatures, for example 237.1 cm^{-1} in figure 7.7.

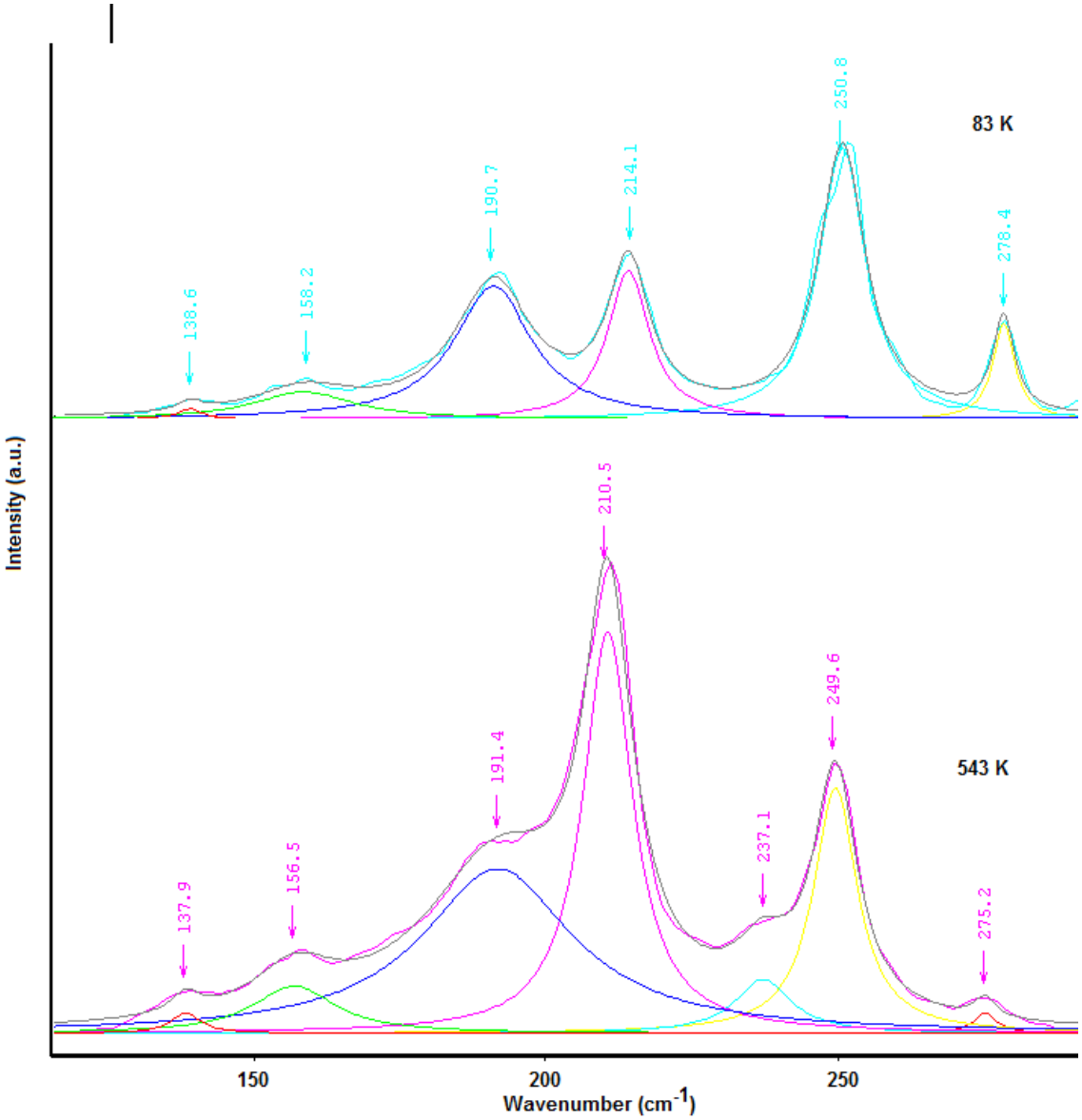

FIGURE 7.7: Fitted Stokes RBMs Spectra at 83 K and 543 K for HiPco tubes at 633 nm

This is due to the fact that as the optical transition energies shift with temperature, different nanotubes move in and out of resonance as the temperature is changed.

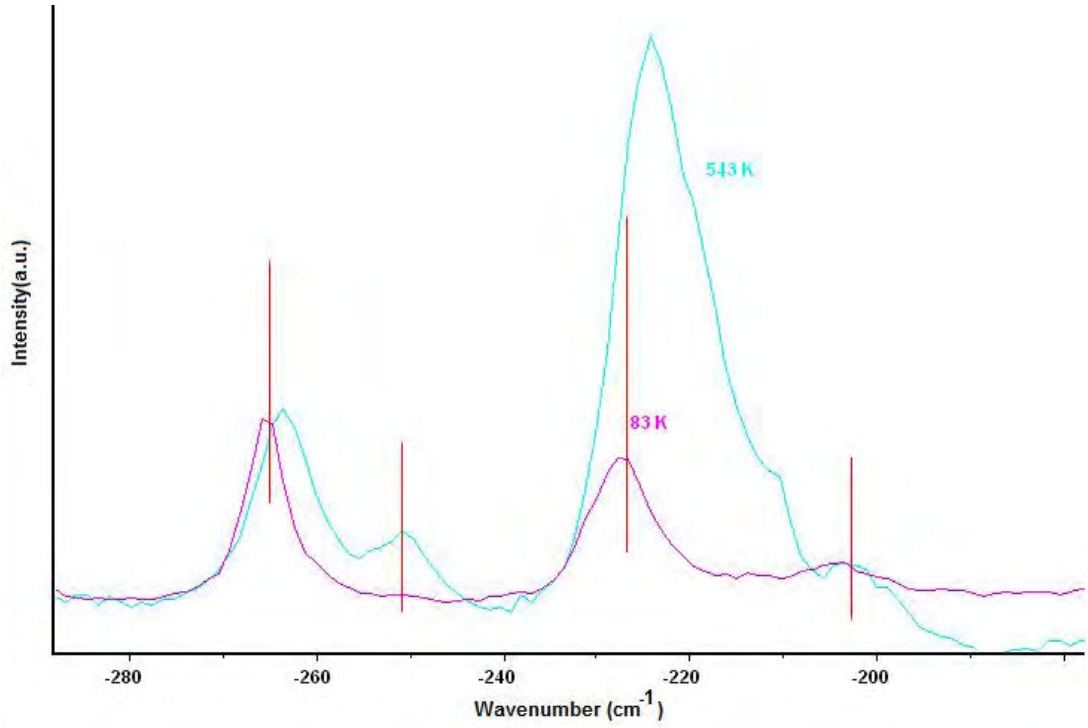

FIGURE 7.8: Anti-Stokes RBMs Spectra at (a) 543 K and (b) 83 K for HiPco tubes at 633 nm

The value of the temperature coefficient for each Stokes RBM is shown in table 7.1. These values are similar within error margins.

RBM cm^{-1}	278.4	250.8	214.1	190.7	158.2	138.7
$\frac{\Delta\omega_{RBM}}{\Delta T}$ cm^{-1}/K	-0.007	-0.003	+0.001	+0.002	-0.003	-0.002

TABLE 7.1: Temperature coefficients for HiPco Stokes RBMs at 633 nm. All values have an error margin of ±0.005 cm^{-1}/K

The temperature dependence of the G^{+}-line at 514.5 nm can be seen in figure 7.9. It should be noted that the temperature dependent study was carried out at 514.5 nm over the temperature range 83 K to 343 K.

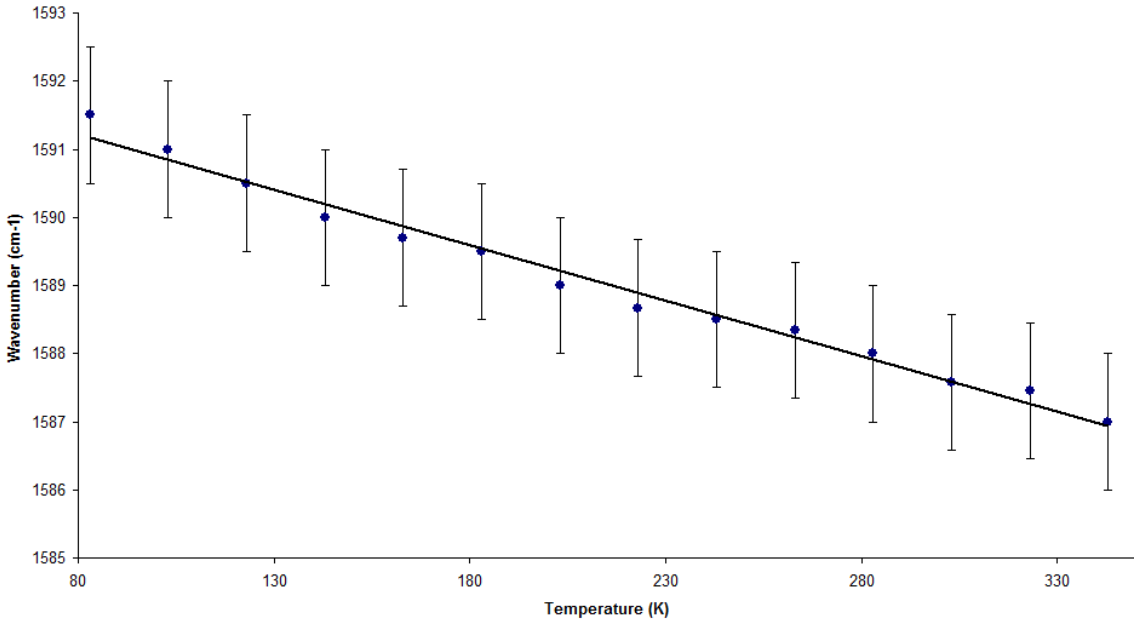

FIGURE 7.9: Temperature Dependent Raman for G^+ lines for Raw HiPco tubes at 514.5 nm

As before, there is a downshift in wavenumber with increasing temperature. The temperature coefficient was calculated to be -0.016±0.009 cm^{-1}/K. The G^--line also downshifts with a temperature coefficient of -0.016±0.001 cm^{-1}/K. The D-line similarly shows a downshift, as shown in figure 7.10 and the calculated temperature coefficient was found to be -0.036±0.006 cm^{-1}/K. The G^*-line was also seen to vary with temperature, as shown in figure 7.11. The temperature coefficient for the G*-line was found to be -0.072±0.003 cm^{-1}/K, notably double that of the D-line. This has been observed in other studies[3].

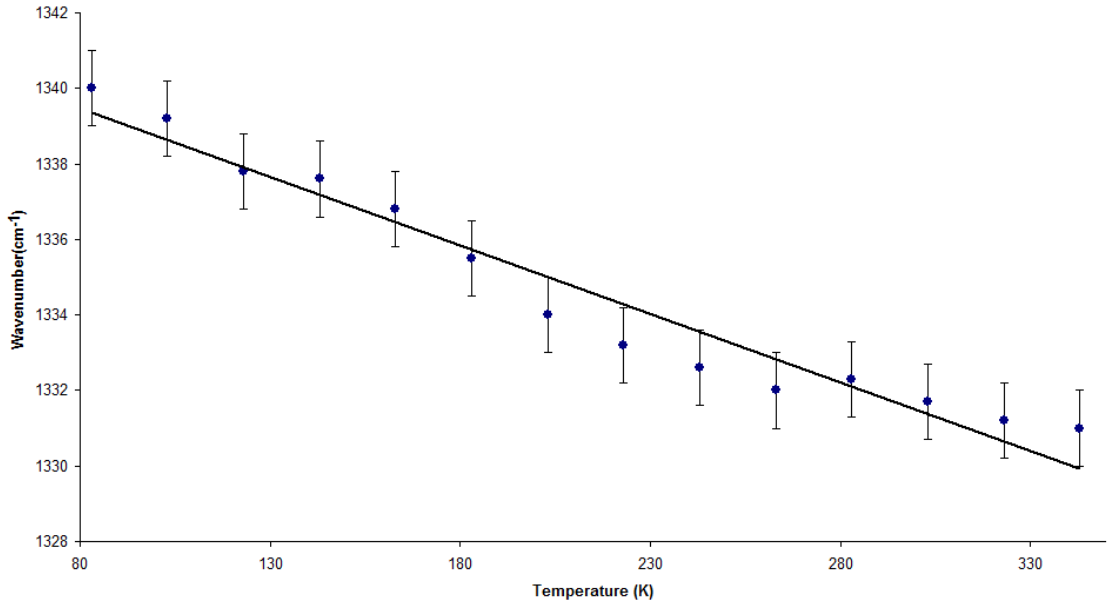

FIGURE 7.10: Raman Shift of D-lines for Raw HiPco tubes at 514.5 nm

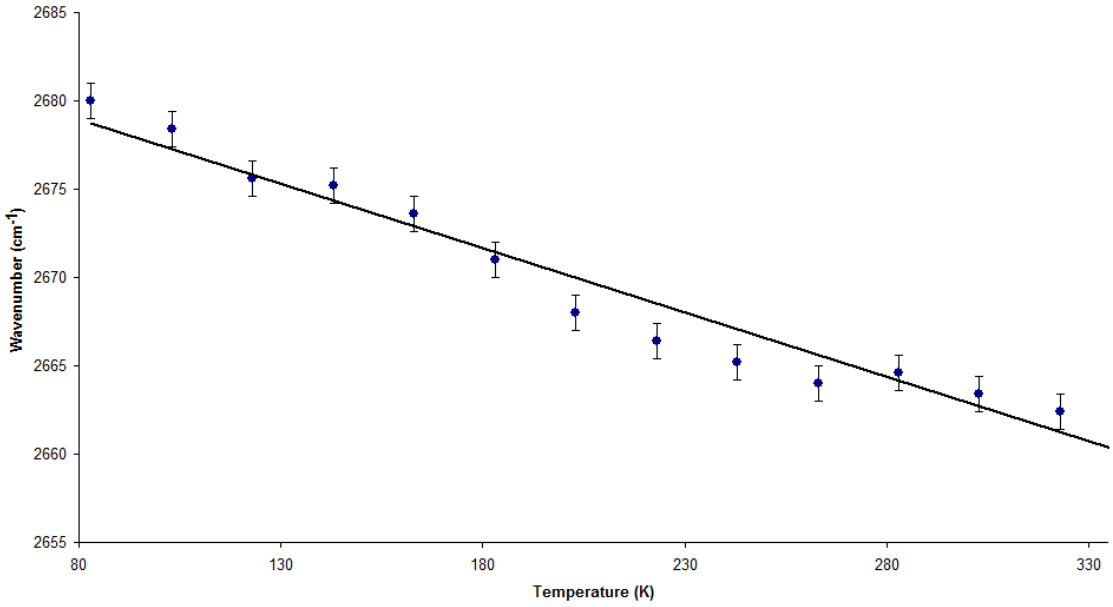

FIGURE 7.11: Raman Shift of G*- lines for Raw HiPco tubes at 514.5 nm

Again shifting of the RBMs is observed in both the Stokes and the anti-Stokes, using 514.5 nm as source, as shown in figures 7.12 and 7.13. Note the extra peak, seen in the red box, at the higher temperature.

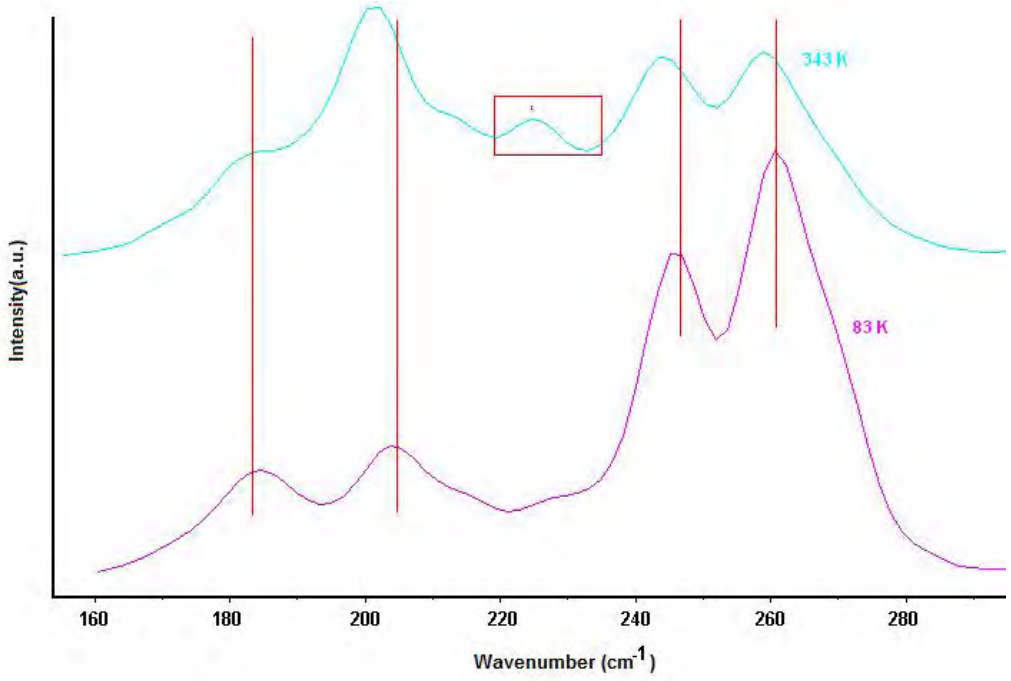

FIGURE 7.12: Stokes RBMs at 83 K and 543 K for Raw HiPco tubes at 514.5 nm

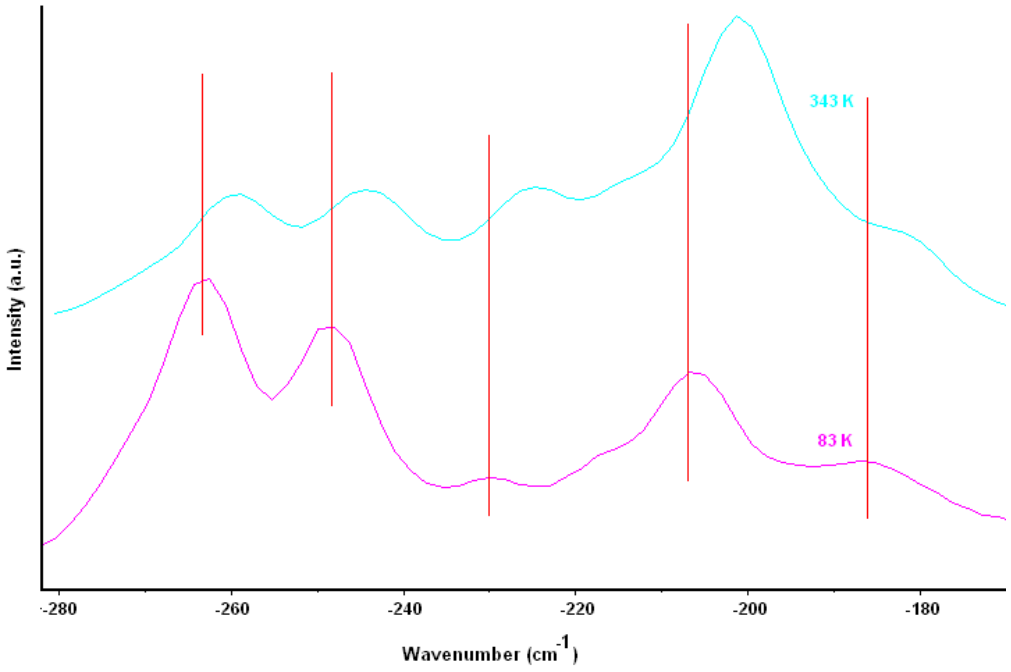

FIGURE 7.13: Anti-Stokes RBMs at 83 K and 343 K for Raw HiPco tubes at 514.5 nm

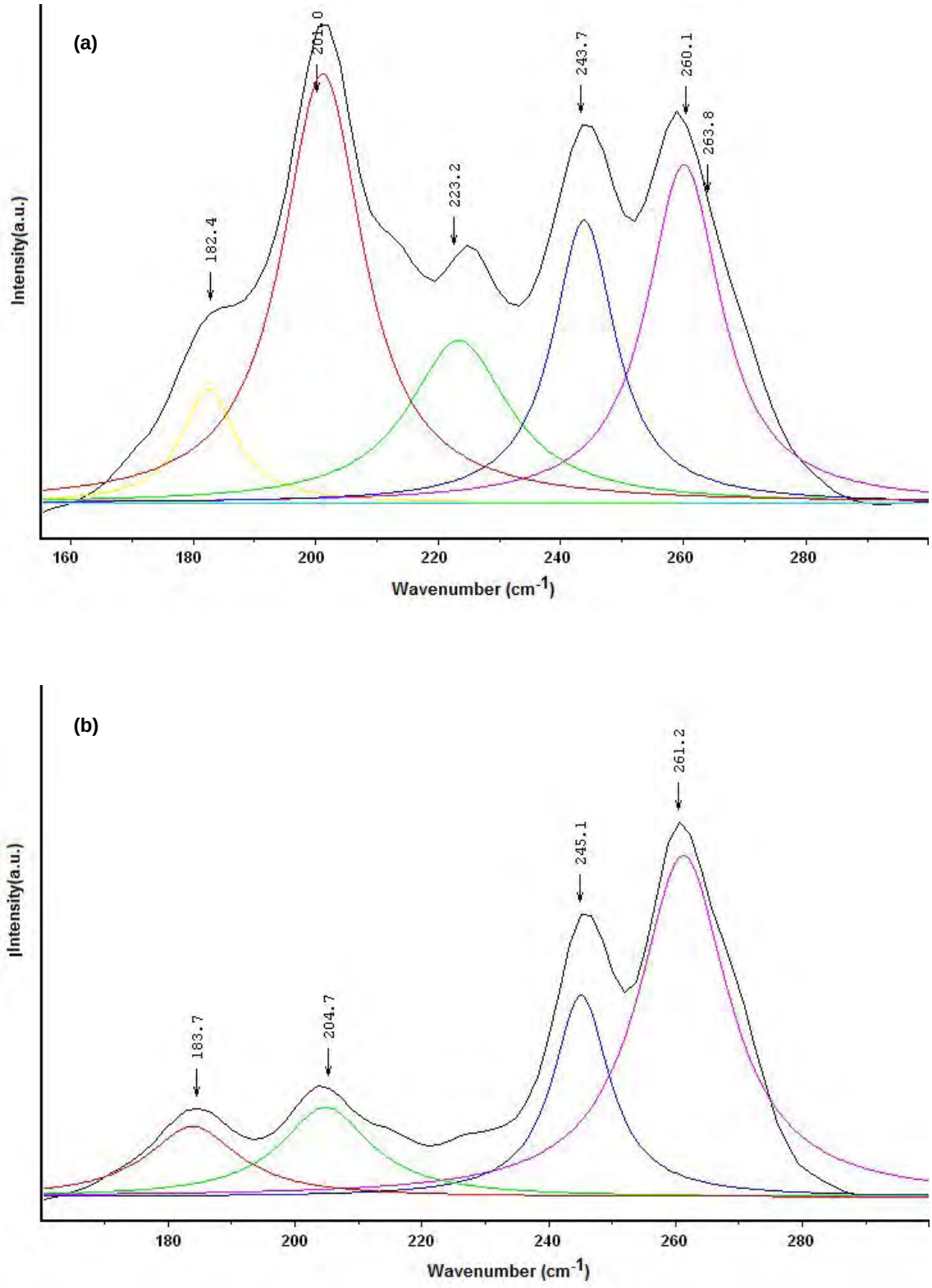

FIGURE 7.14: Fitted Stokes RBMs Spectra at (a) 343 K and (b) 83 K for Raw HiPco tubes at 514.5 nm

The fitted Stokes peaks are shown in figure 7.14 and the value of the temperature coefficient for each Stokes RBM is shown in table 7.2. These values are similar within error margins.

RBM cm^{-1}	261.2	245.1	204.7	183.7
$\frac{\Delta\omega_{RBM}}{\Delta T}$ cm^{-1}/K	-0.002	-0.003	-0.008	-0.003

TABLE 7.2: Temperature coefficients for HiPco Stokes RBMs at 514.5 nm. Each value has an error margin of ±0.005 cm^{-1}/K

A summary of measured parameters for HiPco tubes is found in table 7.3

Excitation Wavelength nm	$\frac{\Delta\omega_{G^+}}{\Delta T}$ cm^{-1}/K	$\frac{\Delta\omega_{G-}}{\Delta T}$ cm^{-1}/K	$\frac{\Delta\omega_{D}}{\Delta T}$ cm^{-1}/K	$\frac{\Delta\omega_{G^+}}{\Delta T}$ cm^{-1}/K
514.5	-0.016±0.009	-0.016±0.009	-0.036±0.006	-0.07±0.003
633	-0.023±0.004	-0.023±0.004	-0.024±0.005	-

TABLE 7.3: Temperature dependence coefficients for Raw HiPco tubes

In summary similar patterns were observed at 514 nm and 633 nm. All characteristic lines downshifted with increasing temperature. The temperature coefficients are similar for both the G and D phonon modes at 633 nm. However, they differ at 514.5 nm. It has been suggested by Browne et al.[12] that the D-line in metallic bundles behaves differently than in semiconducting bundles due to the effects of plasmon-phonon coupling. As previously seen in chapter 4, for this batch of HiPco tubes, metallic tubes are resonant at 514.5 nm. The larger value of temperature coefficient would suggest that the electron-phonon coupling is temperature dependent. This will be further discussed in

section 7. 5. The temperature coefficient for the G*-line is much larger than any of the other measured coefficients. Downshifts were observed in the RBMs in both the Stokes and the anti-Stokes. Additional RBMs become visible at higher temperatures due to the shifting of the optical transition energies with temperature.

7.4 Temperature Dependent Study of the Raman Frequencies of Debundled Single Walled Nanotubes

The nanotubes were debundled using DCE as described in chapter 5. Small glass cover slides were activated as described in chapter 6. For each of the dispersions, at different concentrations, samples were drop cast onto the activated cover slides. Temperature dependent Raman was carried out as in section 7.3 on each of the samples over a temperature range of 83 K to 343 K. Since there was very little observable difference in the results outlined in section 7.3 between the two excitation lines, only results from the 514.5nm study are discussed here. Similar findings were observed at 633nm. For the purposes of the following discussion two concentrations were chosen, 6.25 x 10^{-6} k/L and 2.5 x 10^{-5} k/L, the former below and the latter at or just above the dispersion limit of 2.0±0.5 x 10^{-5} k/L determined in chapter 5 and confirmed in chapter 6.

Figure 7.15 shows the temperature dependence of the frequency positioning of the G^{+}-line. At all temperatures the debundled tubes are upshifted compared to the debundled samples. This is not unexpected. In chapter 6 it was shown that upshifting of characteristic Raman lines is a function of debundling. What is unexpected is that the temperature coefficient is significantly different for the

two concentrations. At a concentration of 2.5 x10^{-5} kg/L it is found to be -0.018±0.009 cm^{-1}/K and at 6.25 x 10^{-6} kg/L it is -0.009±0.004 cm^{-1}/K, indicating that the small degree of bundling just above the dispersion limit is sufficient to significantly affect the temperature dependence of the Raman modes.

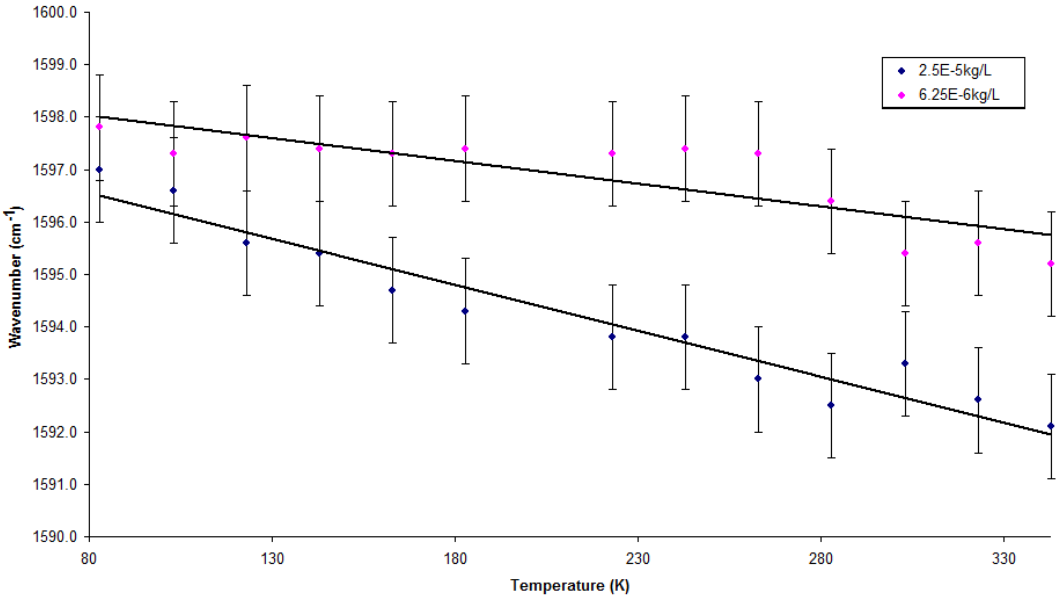

FIGURE 7.15: Temperature Dependence of G-line HiPco/DCE dispersions at 514.5 nm

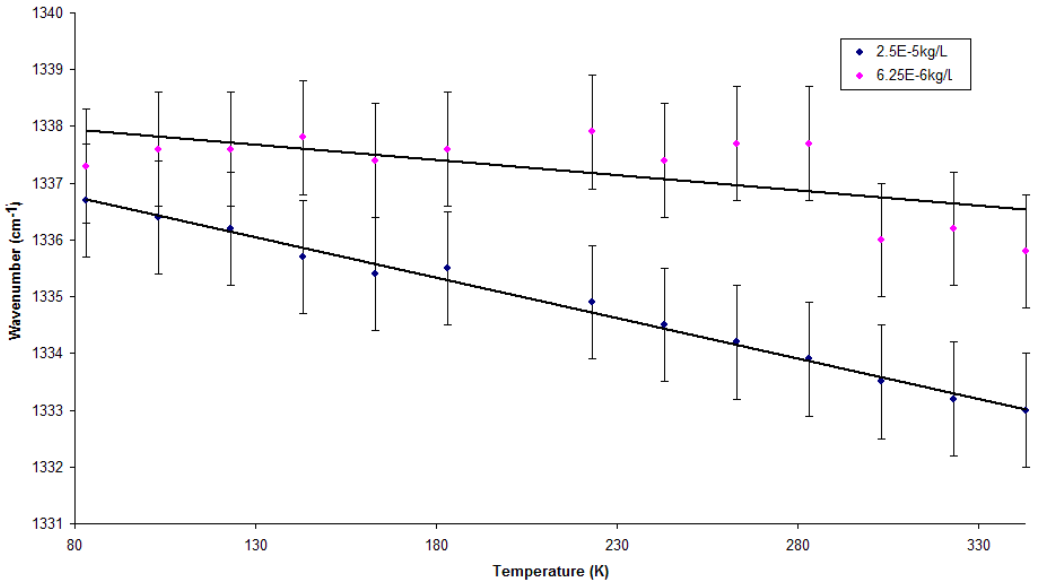

FIGURE 7.16: Temperature Dependence D-line HiPco/DCE dispersions at 514.5 nm

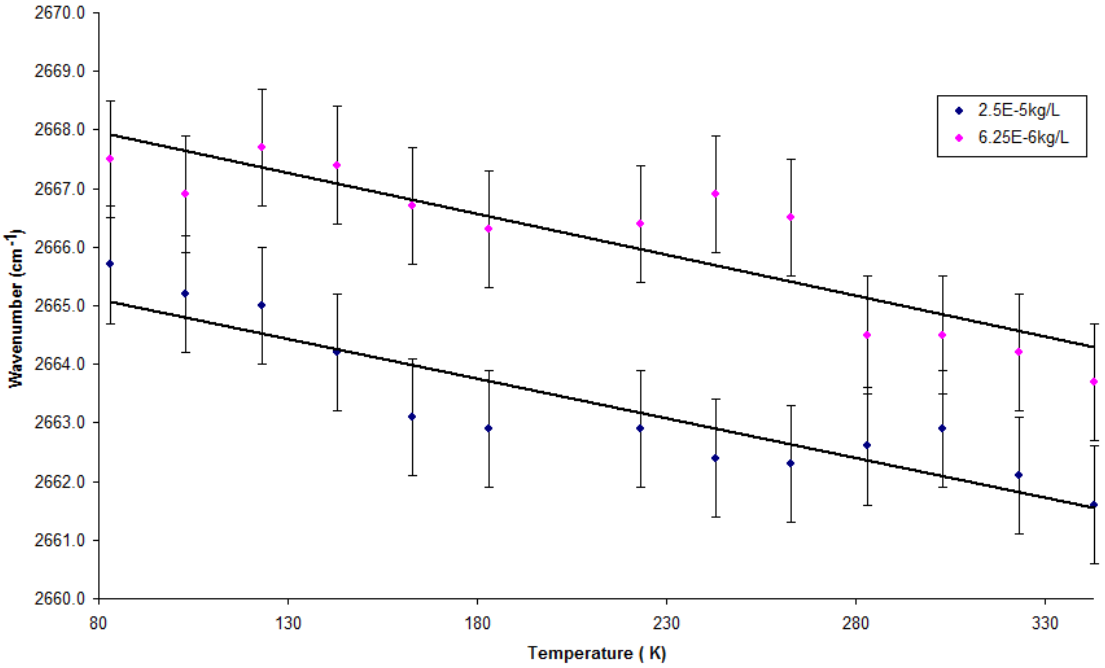

FIGURE 7.17: Temperature Dependence G*-line HiPco/DCE dispersions at 514.5 nm

This trend is again evident in the D and G*-lines shown in figures 7.16 and 7.17. A table of the temperature dependent coefficients of the characteristic lines at 514 nm for the bundled and debundled tubes are shown in table 7.4.

Sample	$\frac{\Delta\omega_{G^+}}{\Delta T}$ cm^{-1}/K	$\frac{\Delta\omega_{D}}{\Delta T}$ cm^{-1}/K	$\frac{\Delta\omega_{G^*}}{\Delta T}$ cm^{-1}/K
Bundles	-0.016	-0.036	-0.070
2.5x10^{-5} kg/L	-0.018	-0.014	-0.018
6.25 x 10^{-6} kg/L	-0.009	-0.005	-0.013

TABLE 7.4: Temperature coefficients of characteristic lines for Raw and Dispersions of HiPco tubes at 514.5 nm

In summary, all characteristic lines downshift with increasing temperature. The upshift of the lines with debundling as seen in chapter 6 was also seen here. The temperature coefficients for debundled tubes are smaller than for bundled tubes for all lines.

There are thus two factors that effect the characteristic line position (phonon mode frequency) in the Raman spectrum of a single walled carbon nanotube: (1) the temperature of the sample and (2) the level of bundling. As discussed in chapter 3, many references show that for graphene, below the Debye temperature of 2500 K, the temperature dependence of the Raman shift in a particular sample is linearly dependent on temperature such that

$$\omega = \omega_0 - \alpha\ T \qquad 7.1$$

where ω_0 is the frequency at 0 K, and α is the temperature coefficient[13][14]. The unit of α is cm^{-1}/K and it is a measure of the relative change in mode frequency with temperature. It is also well established that the frequencies of the characteristic lines are increased in bundles[15][16], such that

$$\omega = \omega_{ST} - A \qquad 7.2$$

where ω_{ST} is the frequency of a single tube and A is a damping factor which is a function of the bundle size (and possibly tube diameter).

Therefore, the highest frequency for a characteristic line will be at 0 K for a single tube. In this study it was observed that in fact this was the case. The highest wavenumber for any given line was observed for debundled tubes at low temperatures.

7.5 Temperature Dependent Study of the Intensities of the Raman Lines in Bundled and Debundled Single Walled Nanotubes

Using the same spectra previously discussed in sections 7.3 and 7.4, a study was carried out on the changes in intensity of the characteristic Raman lines as

a function of temperature. For nanotube bundles it was observed that the intensity of the characteristic lines decrease with increasing temperature, as shown in figures 7.18 for the G-lines at both 514.5 nm and 633 nm.

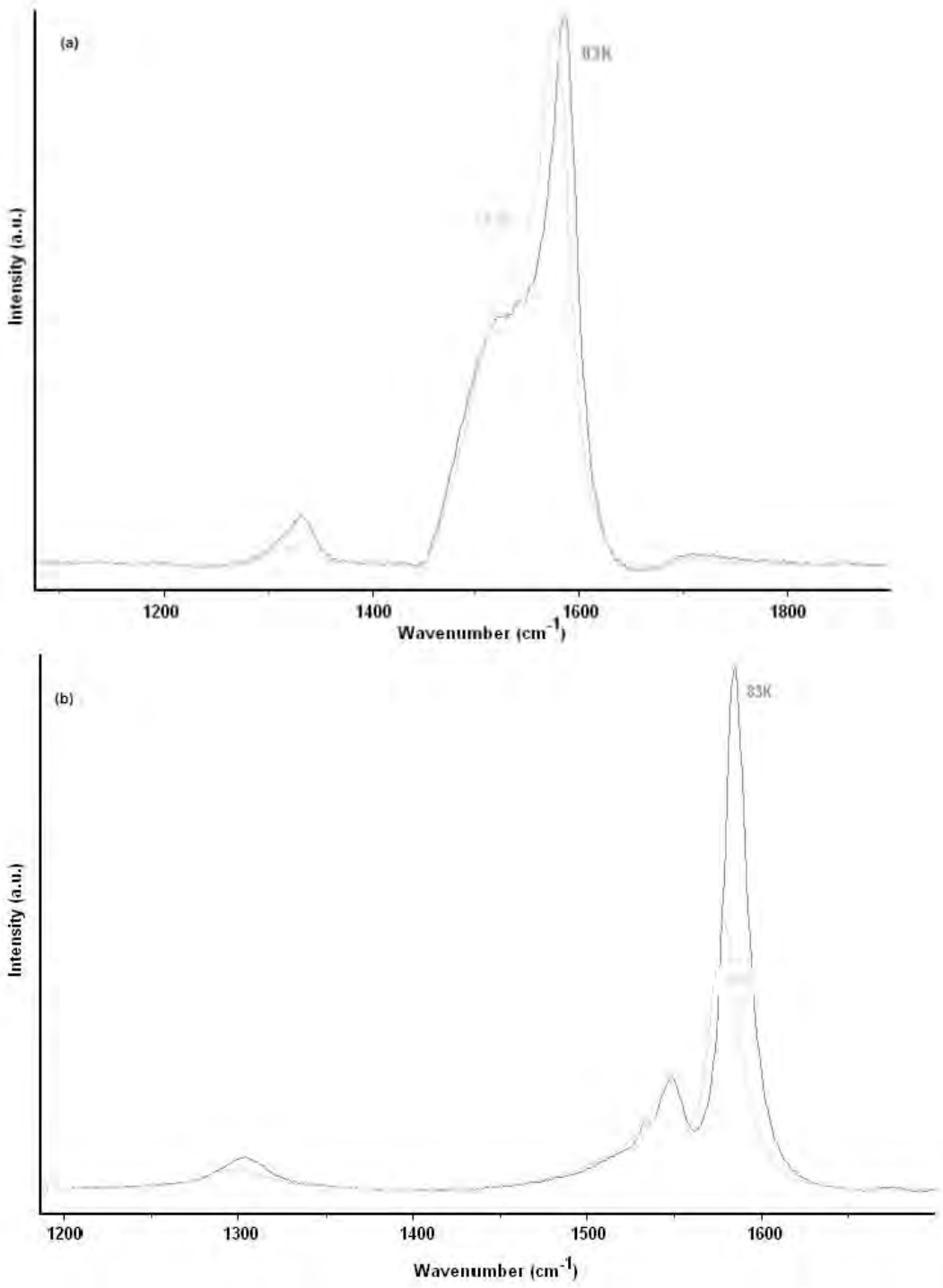

FIGURE 7.18: Part of the Raman spectrum(a) 83 K and 343 K at 514 nm (b) 83 K and 543 K at 633 nm for bundled HiPco tubes

Although a reduction in intensity is observed in both cases, the reduction is small in the case of the 514.5 nm spectrum. This decrease in intensity with increasing temperature is also observed for debundled tubes as seen in figure 7.19.

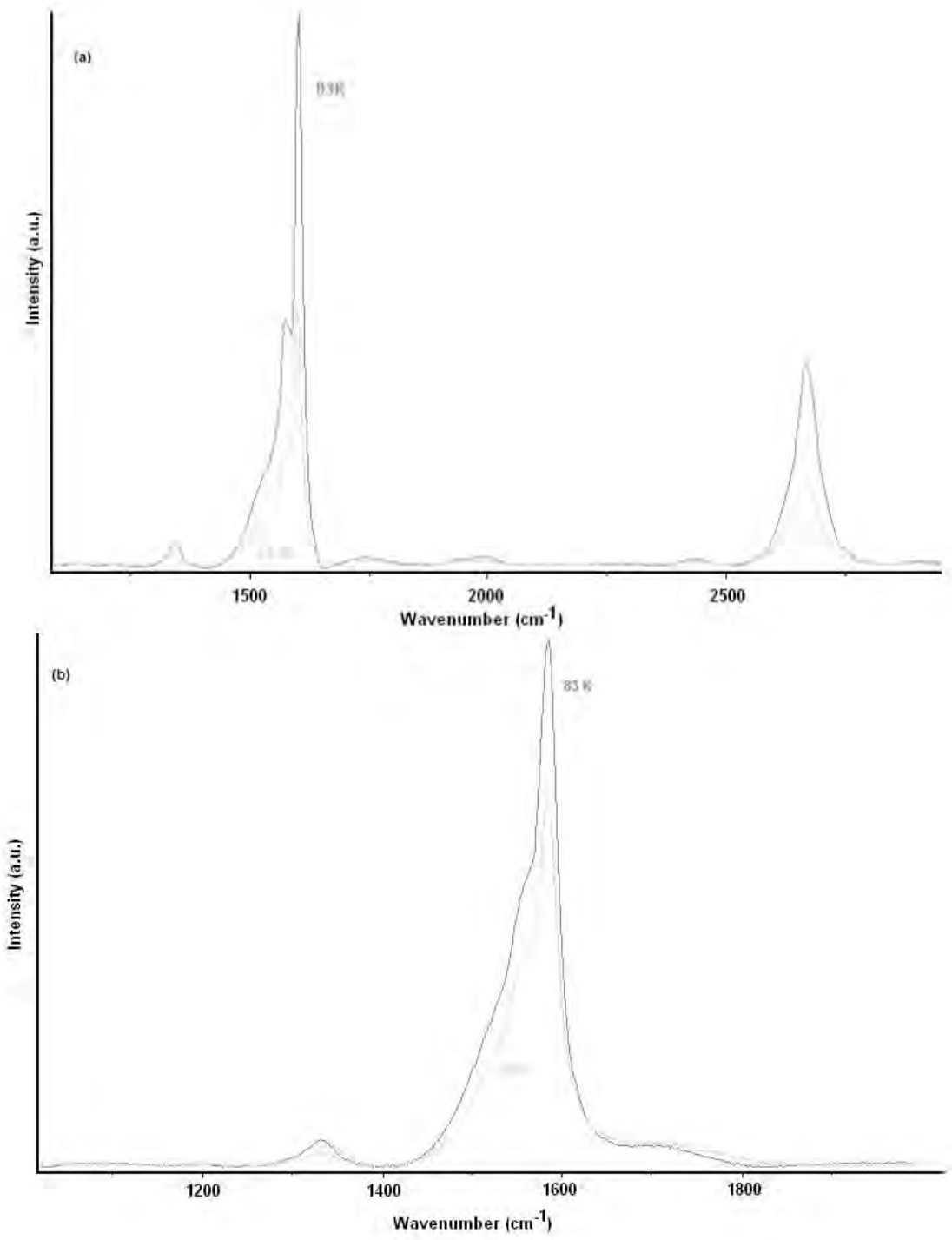

FIGURE 7.19: Part of the Raman spectrum at 83 K and 343 K for debundled HiPco tubes at (a) 514.5 nm (b) 633 nm

The main question which arises is why the reduction in the G-line intensities in bundles at 514.5 nm is significantly less than that observed at 633 nm and for debundled nanotube samples. Attempts to fit observed intensity changes with respect to temperature with any simple models, such as an Arrhenius-like activated behaviour were unsuccessful. Figure 7.20 shows as an example the temperature dependence of the G^+-line of debundled nanotubes at 514.5 nm in an Arrhenius-like representation.

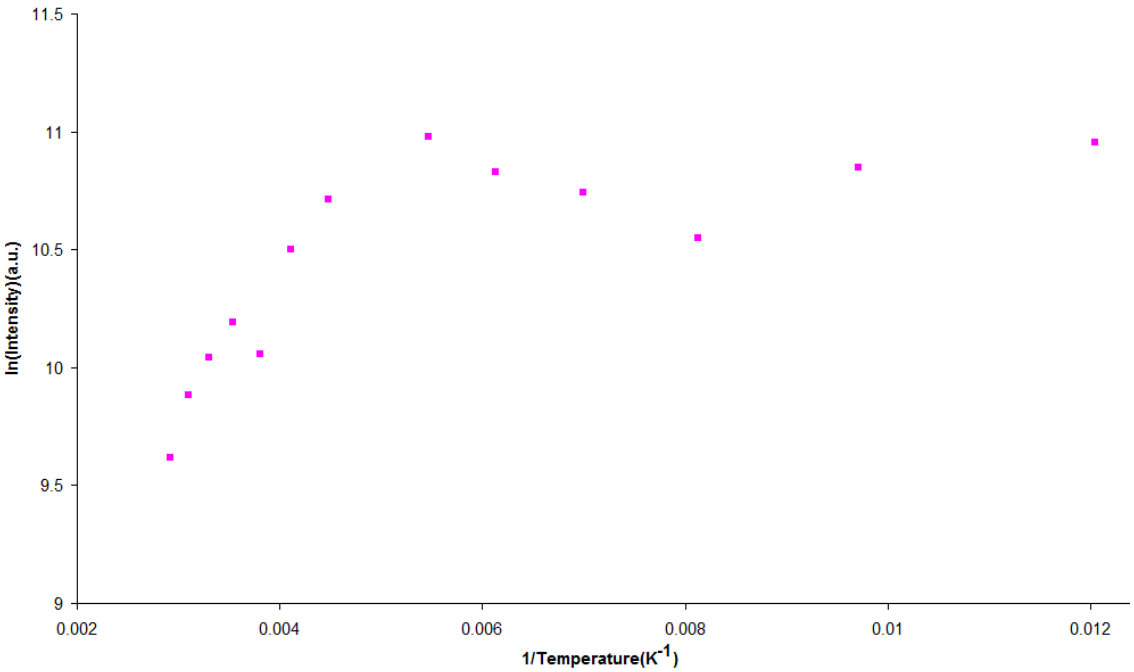

FIGURE 7.20: Peak G^+-line intensity versus inverse temperature for debundled HiPco tubes at 514.5 nm

In order to understand the observed temperature dependencies of the Raman intensities, it is necessary to consider the origin of the Raman scattering in terms of phonons, and the phonon-phonon and electron-phonon interactions which limit their lifetimes.

In a perfect crystal, the linewidth, γ, associated with of a phonon is determined by its interaction with other elementary excitations such as other phonons or electrons. Usually,

$$\gamma = \gamma^{an} + \gamma^{EP} \qquad 7.3$$

where γ^{an} is due to the interaction with other phonons and γ^{EP} with electron hole pairs. γ^{an} is determined by anharmonic terms in the interatomic potential and is omnipresent[17]. γ^{EP} is determined by electron-phonon coupling (EPC) and is only present if the electronic energy gap is zero. It has been shown that the EPC contribution to the G^+ and G^-- lines in semiconducting tubes and to the G^+-line in metallic nanotubes is zero [17]. So it is only in the G^--line in metallic tubes that an EPC contribution to the linewidth is to be found. Phonon lifetimes, τ, are typically estimated using the width of the Raman line shape; the uncertainity principle relates the full width at half maximum (FWHM) of the line shape[18], Γ, to the dephasing rate, T_2

$$1/T_2;\ \Gamma = 10.66/T_2 \qquad 7.4$$

in units of wave numbers and picoseconds[18]. The dephasing rate is equivalent to twice the relaxation time, T_1

$$T_2 = 2T_1 \qquad 7.5$$

Increases in FWHM values of the lineshapes result from decreases in the phonon lifetimes due to increased interaction of the phonons with the other

elementary excitations. Decreases in phonon lifetimes result in a decrease in the intensity of the relevant Raman line[18].

The FWHM values of both the G^+ and G^--lines were calculated for both bundled and debundled tubes. The 633 nm spectra of bundled tubes were fitted with 3 Lorentizan peaks, as shown in figure 7.22 (a). The G-line at 514.5 nm, as mentioned before in chapter 4, has a metallic character to it. It is not a typical metallic line shape but a mixture of semiconducting and metallic lineshapes. It was therefore fitted with 3 peaks, 1 Breit-Wigner-Fano and 2 Lorentizan peaks, as shown in figure 7.22 (b).

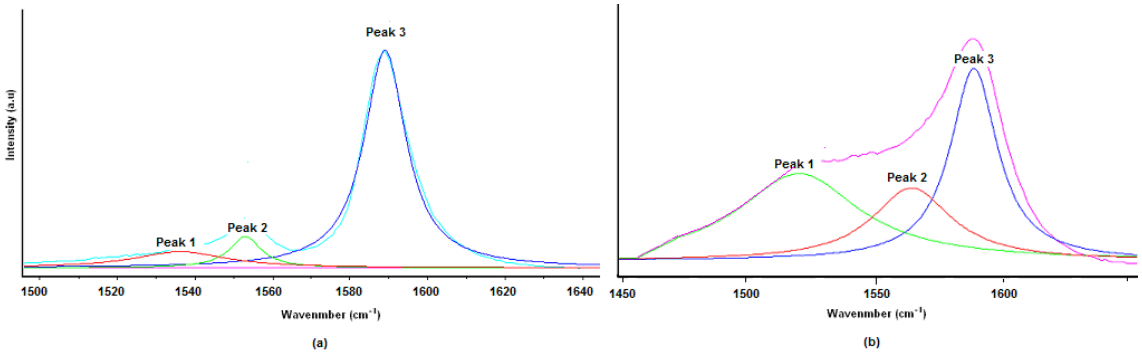

FIGURE 7.22: Fitted G-line spectra at 83K for debundled HiPco tubes at (a) 633nm and (b) 514.5nm

The temperature dependence of the FWHMs thus derived for bundled tubes can be seen in figures 7.23 and 7.24. The FWHM values for all peaks increases with increasing temperature except for that of the Breit-Wigner-Fano (peak 1 in figure 7.24) which decreases with increasing temperature. Since theory predicts no EPC associated with the other peaks in figure 7.23 and 7.24 the observed changes in FWHM values must be associated with temperature dependent changes in the phonon-phonon interaction. This is consistent with the fact that

the phonon-phonon interaction increases with increasing temperature as a result of the increased phonon population density[18].

The Breit-Wigner-Fano feature is the only feature which has significant contributions from EPC and exhibits a downward trend of the linewidth with increasing temperature. As discussed in chapter 3, the Breit-Wigner-Fano lineshape arises from (electron) plasmon – phonon interactions and is only evident in SWNT bundles. Plasmon formation enhances electron-phonon coupling. It has been shown that the intertube distance in nanotubes bundles increases with increasing temperature having a thermal expansion coefficient of $4.2 \times 10^{-5}/K$[18]. An increase in intertube distance as a function of temperature acts to reduce the formation of the plasmon band and therefore the electron-phonon interaction as seen by the increase in the FWHM of the Breit-Wigner-Fano line with temperature, in other words an increase in the LO phonon mode lifetime.

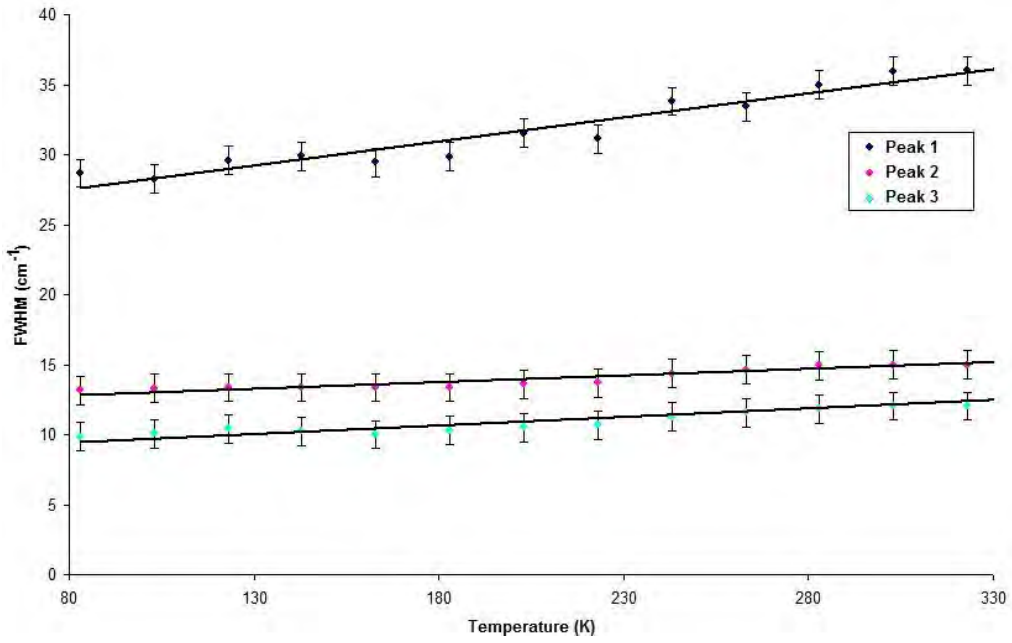

FIGURE 7.23: Temperature dependence of the fitted components of the G-line FWHM values for bundled HiPco tubes at 633 nm

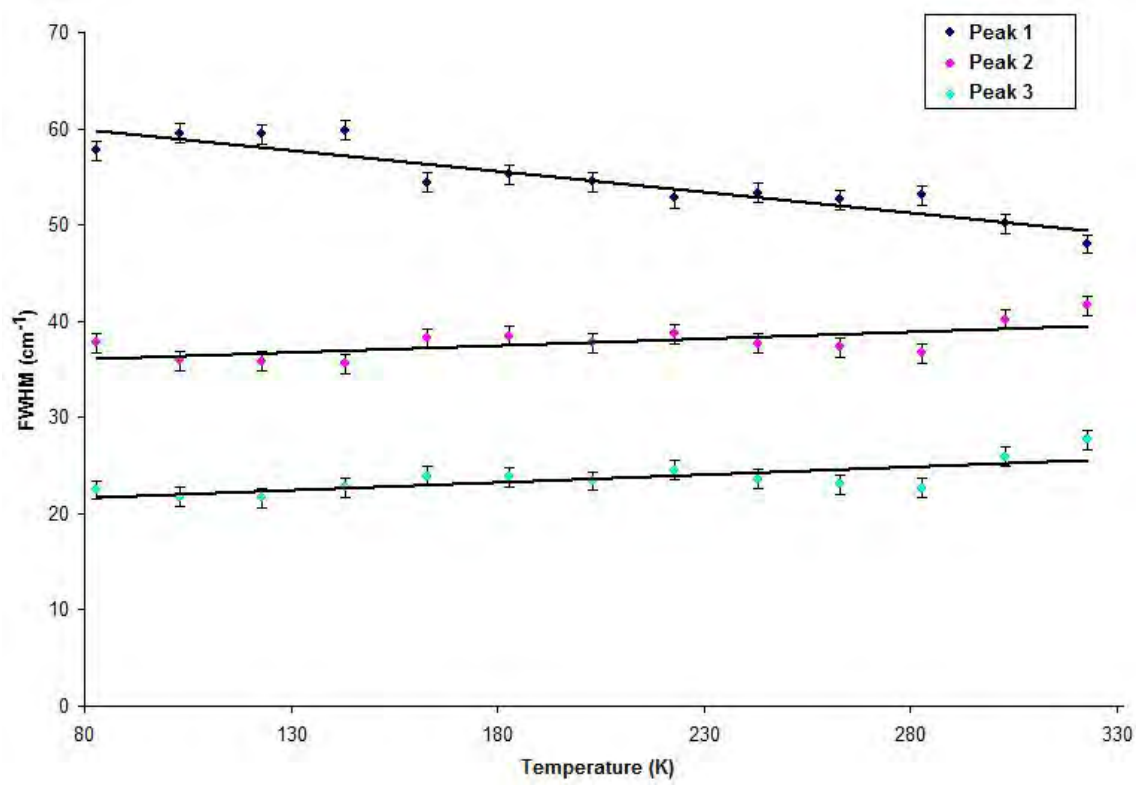

FIGURE 7.24: Temperature dependence of the fitted components of the G-line FWHM values for bundled HiPco tubes at 514.5 nm

The result on the overall spectra in the case of the bundles at 633 nm is a reduction in intensity with temperature accounted for by the decrease in all phonon lifetimes. However, in the case of the bundles at 514.5 nm, there are 2 competing effects – an increase in the phonon-phonon interaction and a decrease in the EPC. The former acts to decrease the phonon lifetime and thus Raman intensity whereas the former results in an increase. The net effect is the slight reduction in intensity observed.

The FWHM values of the fitted G-line peaks as a function of temperature for debunded tubes, obtained from the 6.25 x 10^{-6} k/L dispersion in DCE at 514.5 nm, is shown in figure 7.25. Note that this concentration is below the debundling limit discussed in chapters 5 and 6. It should also be noted that the

G-lines were fitted with 3 Lorentzian's, the Breit-Wigner-Fano lineshape having disappeared on debundling as shown in 6.3 and previously reported[21].

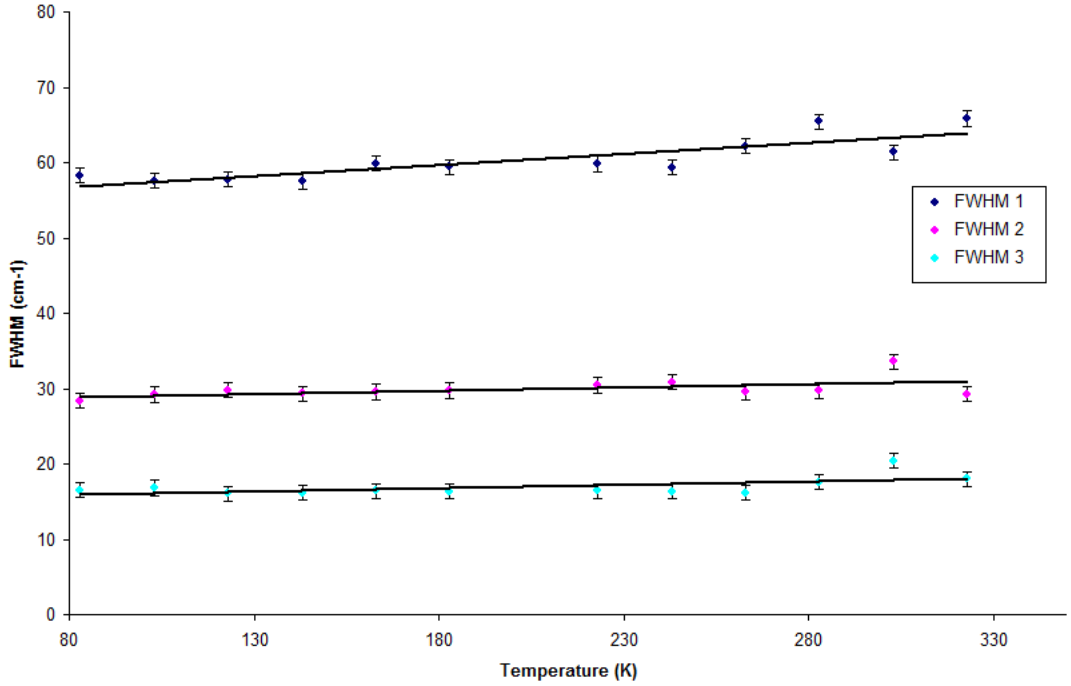

FIGURE 7.25: Temperature dependence of G line FWHM values for debundled HiPco tubes at 514.5 nm

The most noticeable aspect is that the FWHM of peak 1 for debundled tubes now increases with temperature in contrast to the case for bundled tubes where it decreased. The plasmon-phonon interactions seen in the bundled tubes have disappeared leaving just electron-phonon coupling. The temperature coefficients of the FWHM values are shown in table 7.5

	Bundled 633 nm cm^{-1}/K	Debundled 633 nm cm^{-1}/K	Bundled 514 nm cm^{-1}/K	Debundled 514 nm cm^{-1}/K
Peak 1	0.034±0.005	0.04±0.02	-0.043±0.006	0.030±0.011
Peak 2	0.010±0.002	0.007±0.001	0.014±0.010	0.009±0.001
Peak 3	0.012±0.007	0.008±0.001	0.016±0.014	0.009±0.011

TABLE 7.5: Temperature coefficients of FWHM values for bundled and debundled tubes at 514.5 nm and 633 nm

The changes of intensity with temperature, seen in figures 7.18 and 7.19 can now be discussed in terms of changes in phonon interactions. In the case of the semiconducting bundles, seen in figure 7.23, the FWHM values of all peaks increase with temperature. The phonon-phonon interaction is increasing with temperature, as expected, resulting in a reduction in the overall intensity of the G-line phonon modes. In the case of the metallic bundles, seen in figure 7.24, the relatively large negative FWHM temperature coefficient of the Breit-Wigner-Fano feature is indicative of a reduction of the plasmon–phonon interaction with increasing temperature. However, the Lorenzian features exhibit increasing FWHM values, due to increased phonon-phonon interaction with increasing temperature. The net result of the competing temperature responses is very little change in the intensity values over the temperature range used in this study. When the tubes are debundled the plasmon-phonon coupling present in bundles is removed and as seen in figure 7.25 the FWHM values of all peaks increase with increasing temperature resulting in a reduction in the intensity with increasing temperature.

Using equations 7.4 and 7.5, the lifetime of the plasmon – longitudinal optical phonon scattering at 88 k and 303K of the metallic nanotube bundles was calculated to be 0.09 ps and 0.1 ps. Values of 0.1 ps have been previously calculated[17][21][22]. Using equation 2.5 with values of bond length of 1.42 Å and C-C tight bonding overlap energy of 2.7 eV, the Fermi velocity was calculated to be 8.6×10^5 ms^{-1}. The mean free path due to plasmon-phonon scattering was calculated at 83 K and 303 K to be 0.08 μm and 0.10 μm. Room temperature values of 0.18 μm[23] and 0.46 μm[24] have been previously reported. The first

study used AFM as an electrical probe and the latter was theoretically calculated for tubes of diameter 1.4 nm. Using the same equations the electron-phonon scattering lifetimes in the debundled tubes were calculated to be 0.091 ps and 0.086 ps at 83 K and 303 K respectively. The electron-phonon scattering mean free path was calculated to be 0.08 μm at 83 K and 0.07 μm at 303 K. This would suggest that at room temperature, the transport properties of metallic bundles are better than those of single tubes.

7.6 Temperature Dependent Study of the Intensity Ratios of the Raman Lines in Bundled and Debundled Single Walled Nanotubes

The temperature dependence of some of the ratios examined in chapters 4 and 6 were measured. Figure 7.26 shows the temperature dependence of the G^+/D, G^-/D and G^+/G^- ratios for raw tubes at 633 nm. Statistical variation calculated from multiple data in the ratios were as follows G^+/D ±3.5, G^-/D ±0.3 and G^+/G^- ±0.3. Taking this into account there is no clear evidence of any change in these ratio values with temperature. Figure 7.27 shows the ratios taken at 514.5 nm. Again within the statistical variations of G^+/D±1, G*/D±0.4 and G^+/G^*±0.25 there is no evidence of change with temperature.

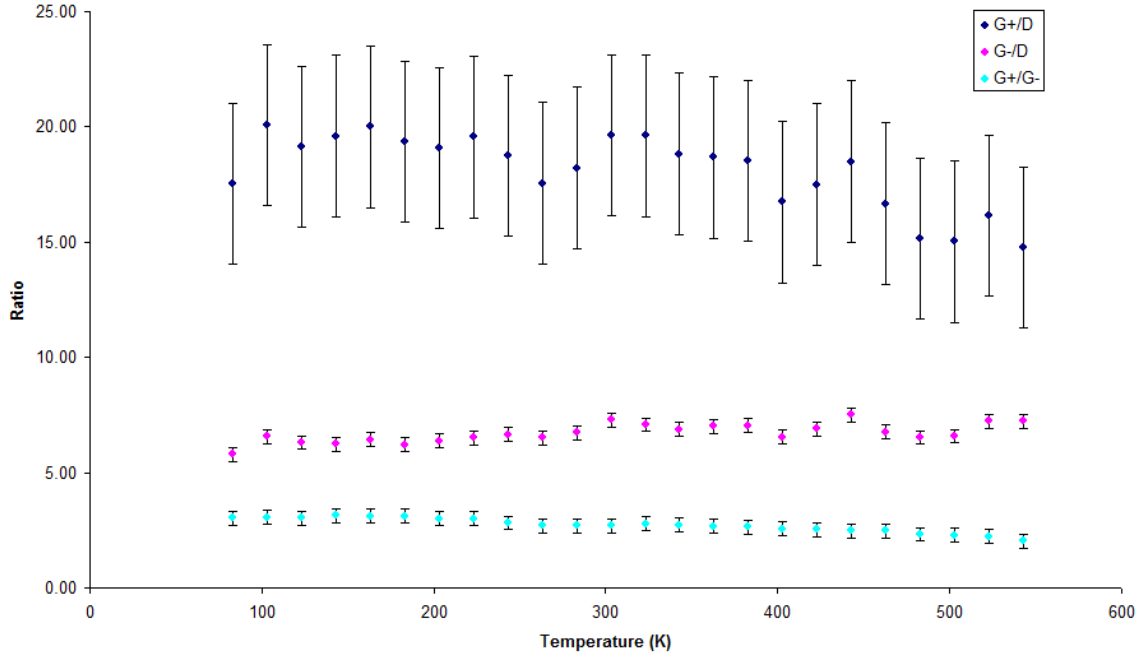

FIGURE 7.26: Ratio of G^+/D,G^-/D and G^+/G^- as a function of temperature for raw HiPco tubes at 633 nm

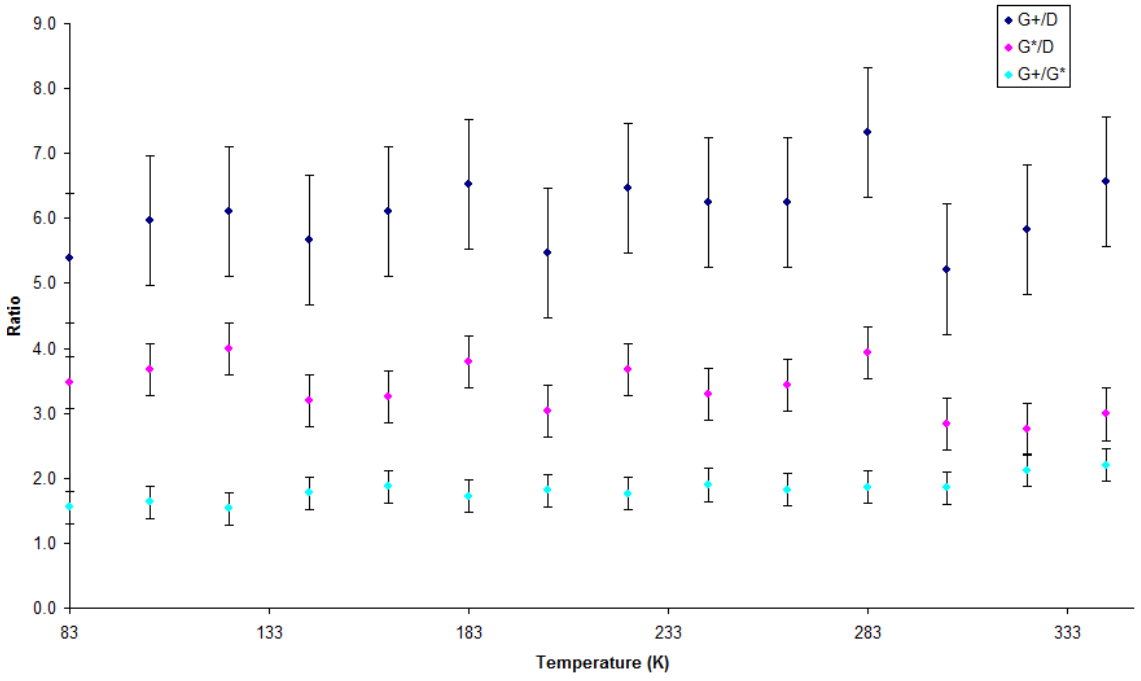

FIGURE 7.27: Ratio of G^+/D, G*/D and G^+/G^* as a function of temperature for raw HiPco tubes at 514.5 nm

The ratios of the characteristic lines were measured for the debundled samples. As in the case of the raw tubes, no temperature dependent variation was observed. This is illustrated in figure 7.28 for the G^+/D ratio.

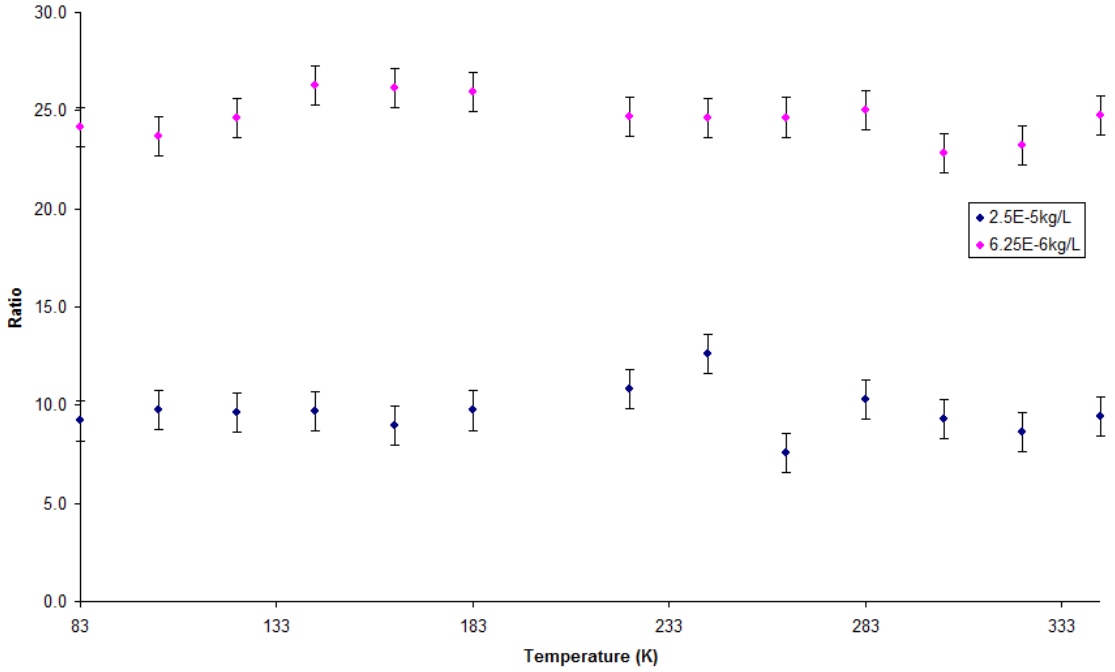

FIGURE 7.28: Ratio of G^+/D as a function of temperature for HiPco/DCE dispersions at 514.5 nm

Notice that the average value is higher for the debundled tubes. This was also observed in chapter 6 section 6.3. This in fact is the case for all the characteristic ratios as shown in table 7.6 (the values shown are average values over the temperature range examined).

Sample	G^+/D	G*/D	G^+/G^*
Bundles	6.1	3.4	1.9
$2.5x10^{-5}$ kg/L	9.8	5.3	2.0
6.25×10^{-6} kg/L	24.7	9.7	2.6

TABLE 7.6: Average values of the characteristic ratios for raw HiPco tubes and HiPco/DCE dispersions at 514.5 nm

The origin of the G*-line has been a mystery for some time. Certainly it is an overtone of the D-line, as the ratio of the wavenumbers consistently shows a value of between 1.99 and 2.0. However, the relative intensity of the G*-line is a different question. In chapter 4, the dominance of the G*-line line in metallic

Raman signatures was observed. In chapter 6 the G*-line was seen to behave independently of the other characteristic lines, decreasing in size for debundled tubes. Normalization of the G^+-lines was carried out for 2 samples, one partially bundled (2.5 x 10^{-5} kg/L) and the other debundled (6.25 x 10^{-6} kg/L) for a range of temperatures. The relative intensity of the G*-lines decreased for the partially bundled tubes but remained constant as a function of temperature for the debundled tubes as shown in figures 7.29 and 7.30. The D-line remained constant in both cases.

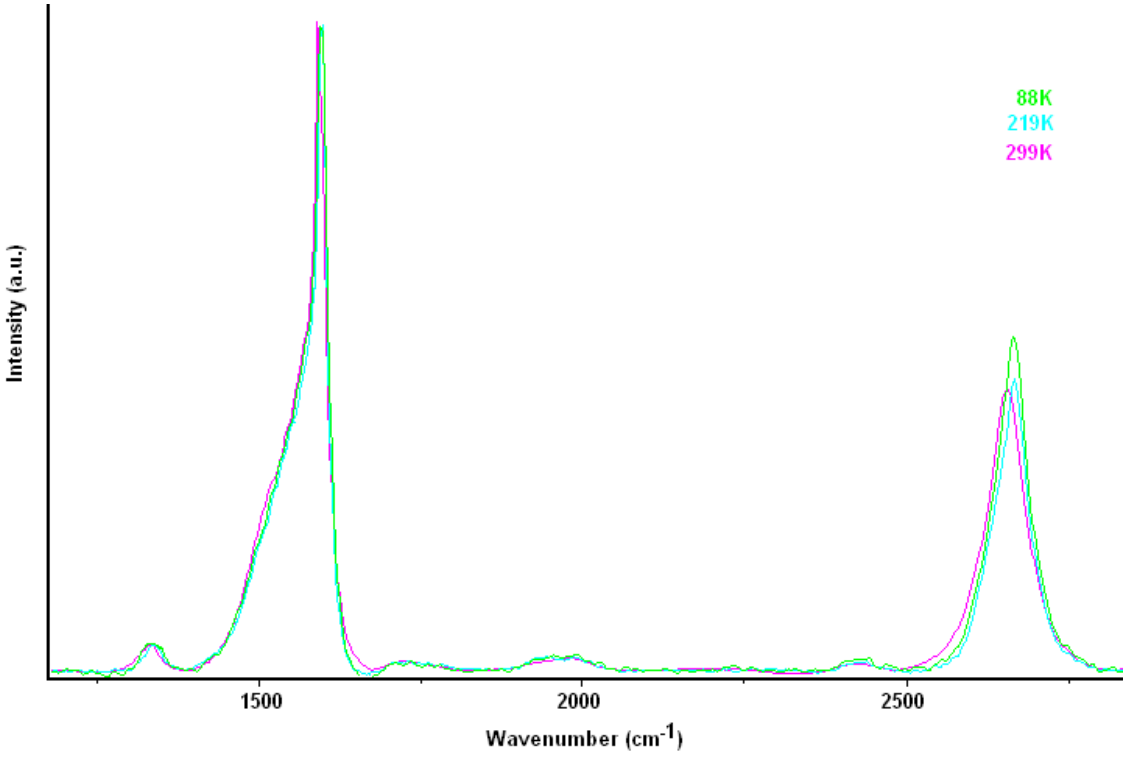

FIGURE 7.29: Normalised G –line spectra for a range of temperatures for partially debundled HiPco tubes

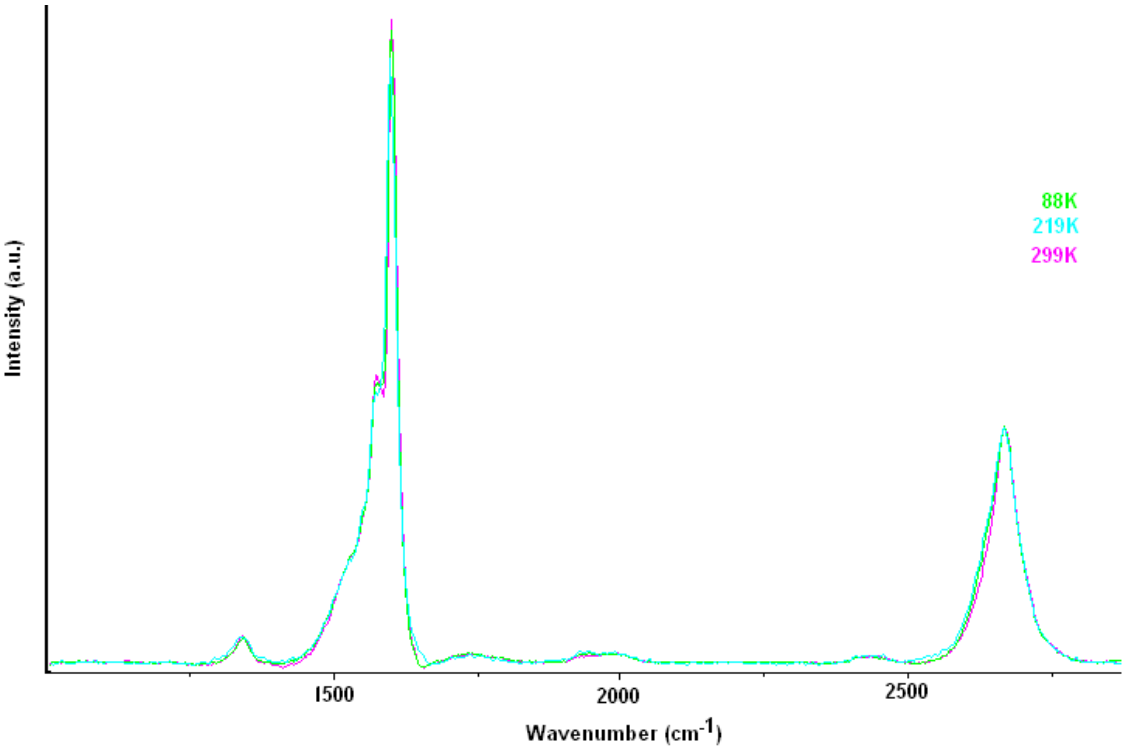

FIGURE 7.30: Normalised G –line spectra for a range of temperatures for debundled HiPco tubes

The fact that the G*-line was observed to have a temperature dependence for bundled tubes but not for debundled tubes would suggest that there is a contribution to the G*-line from plasmon-phonon coupling and that this, as in the case of the G band, decreases with increasing temperature. The unchanged D-line, would suggest that the G*-line, in addition to being an overtone of the D-line has in its own right extra information about the electronic character of the nanotube system.

7.7 Summary

The frequency of the characteristic lines downshift with increasing temperature. The temperature coefficients are smaller for debundled tubes. The RBMs show a complex shifting pattern with different tubes coming in and out of resonance with changing temperature. The intensity of the Raman spectral features reduce

with increasing temperature due to increased phonon-phonon interaction. This reduction in the intensity is not as strong in metallic bundles due to weakening plasmon–phonon coupling with increased temperature. However in debundled tubes the plasmon–phonon coupling disappears and is replaced with electron-phonon coupling which results in a decrease in intensity with increasing temperature. The mean free path due to plasmon-phonon scattering in bundled tubes was calculated at 83 K and 303 K to be 0.08 μm and 0.10 μm while the mean free path due to electron-phonon coupling in debundled tubes at 83 k and 303 K was calculated to be 0.08 μm and 0.07 μm. The G*-line in metallic tubes is found to have an additional electron – phonon coupling component not found in any of the other characteristic lines.

7.6 References

[1] M.S.Dresselhaus, G.Dresselhaus, R.Saito, A.Jorio Physics Reports **409,** 47-99 (2005)

[2] Z.Yao, C.L.Kane, C.Dekker Phys. Rev.Lett. **84,** 2941(2000)

[3] V.Perebeinos, J.Tersoff, P.Avouris Phys. Rev. Lett. **94,** 086802 (2005)

[4] J.Y.Park, S.Rosenblatt, Y.Yaish, V.Sazonova, H.Üstünel, S.Braig, T. A. Arias, P. W. Brouwer, P.L. McEuen Nano Lett **4,** 517 (2004)

[5] Linkam THMS600 heating and cooling stage operational manual

[6] R.M.Martin, L.M.Falicov, *Light Scattering in Solids I (Springer Series in Topics in Applied Physics Vol 8),* ed. M. Cardona (Berlin: Springer) chapter 3 pg 70 (1983)

[7] P.V.Huong, R.Cavagnat, P.M.Ajayan, O.Stephen, Phys. Rev. B **51,** 10048-51 (1995)

[8] F.Huang, K.T.Yue, P.Tan, S.L.Zhang, Z.Shi, X.Zhou, Z.Gu, J.Appl.Phys. **84,** 4022-4

[9] H.D.Li, K.T.Yue, Z.L.Lian, L.X.Zhou, S.L.Zhang, Z.J.Shi, Z.N.Gu, B.B.Liu, R.S.Yang, H.B.Yang, G.T.Zou, Y.Zhang, S Iijima Appl. Phys.Lett .**76,** 2053-5 (2000)

[10] Q.Zhang, D.J.Yang, S.G.Wang, S.F.Yoon, J.Ahn Smart Materials and Structures **15,** S1-S4 (2006)

[11] C.Fantini, A.Jorio, M.Souza, M.S.Strano, M.S.Dresselhaus, M.A.Pimenta Phys.Rev.Lett **93,** 147406 (2004)

[12] S.D.M.Brown, A.Jorio, M.S.Dresselhaus, G.Dresselhaus, Phys.Rev.B, **64**, 073403 (2001)

[13] H.Herchen and M.A.Cappelli Phys. Rev. B **43,** 1(1991)

[14] M.Balkanski, R.F.Wallis and E.Haro Phys. Rev. B **28,** 1928(1983)

[15] M.Milnera, J.Kűrti, M.Hulman, H.Kuzmany, Phys.Rev. Lett. **84,** 1324 (2000)

[16] A.Jorio, R.Saito, J.H.Hafner, C.M.Lieber, M.Hunter, T.McClure, G.Dresselhaus, M.S.Dresselhaus, Phys.Rev.Lett. **86,** 1118 (2001)

[17] M.Lazzeri, S.Piscanec, F.Mauri, A. C. Ferrari, J. Robertson Phys. Rev B **73**, 155426 (2006)

[18] D.D.Dlott, Annu.Rev.Phys. Chem.**37,** 157 (1986)

[19] Y.Maniwa, R.Fujiwara, H.Kira, H.Tou, H.Kataura, S.Suzuki, Y.Achiba, E.Nishibori, M.Takata, M.Sakata, A.Dujiwara, H.Suematsu, Phys.Rev.B **64,** 241402 (2001)

[20] M.Paillet, Ph.Ponvharal, A.Zahab, J.L.Sauvajol, Phys.Rev.Lett. **94,** 237401 (2005)

[21] A.Jorio, C.Fantini, M.S.S.Dantas, M.A.Pimenta, A.G.Souza, Filho, G.G.Samsonidze, V.W.Brar, G. Dresselhaus, M.S.Dresselhaus, A.K.Swan, M.S.Űnlű, B.B.Goldberg, R.Saito, Phys.Rev.B **66,** 115411 (2002)

[22] M.Oron-Carl, F.Hennrich, M.M.Kappes, H.v.Löhneysen, R.Krupke, Nano.Lett. **5,** 1761 (2005)

[23] J.Park, S.Rosenblatt, Y.Yaish, V.Sazonova, H.Ustunel, S.Braig, T. A. Arias, P. Brouwer, P.L. McEuen, *Nano Lett.* **4**, 517 (2004)

[24] G.M.Zhao Cond.Mat 0208201v2 (2002)

CHAPTER 8

CONCLUSIONS

8.1 Discussion of Results

The aim of this study was to explore the use of the relatively inexpensive, high throughput technique of Raman spectroscopy to characterise single walled carbon nanotube samples and to show how this relatively simple technique could be used to characterise and predict their fundamental properties. Commercially available carbon nanotubes are bundled, impure and relatively difficult to process. Despite the extensive research into their physical properties, the literature can be misleading due to the lack of differentiation between bundled and debundled sample, and the use of a range of processing techniques which can themselves alter the fundamental properties.

In this study a range of common organic solvents, DCE, DMF and toluene were chosen to disperse and debundle commercially available nanotube samples produced by the HiPco and the arc discharge techniques. The solvents were chosen for different reasons. Both DCE and DMF are non-polar solvents and on the basis of “like dissolves like” should be suitable for dispersing nanotubes. In addition, from the consensus of previous studies as discussed in chapter 1, both should be good candidates as they exhibit high electron pair donicity due to the lone pair on the nitrogen bond in the case of DMF and on the chlorine in the case of DCE. Toluene was chosen as an example of a solvent with a poor ability to solubilise nanotubes. Nonlinearities in the concentration dependent UV/Vis/NIR absorption indicated that smaller bundles as well as debundled tubes were produced below a critical dispersion limit and this was confirmed using TEM and AFM. Both the bundled and debundled samples were characterised using Raman spectroscopy and the subtle changes occurring in

the Raman spectrum between samples identified and thus the changes to the fundamental characteristics as a result of the perturbations induced by bundling were elucidated.

While absorption spectroscopy is a valuable tool for monitoring the characteristics of a SWNT sample, the true absorption characteristics of the nanotube sample are often masked by the strong scattering of bundles in suspension. An integrating sphere was used in this study to differentiate scatter from the suspensions from absorption and to yield a more accurate absorption spectrum. Monitoring of the concentration dependence of the scatter and absorption was used to identify the critical debundling point and to semi-quantitatively compare the degree of solubilisation and relative bundle sizes of the different solvents. It was found that DCE, DMF and toluene can be used to solubilise single wall nanotubes to varying degrees of efficacy. DCE and DMF are much better than toluene, which even at low concentrations doesn't seem to completely disperse the tubes.

It was shown that for DCE the calculated extinction coefficients, taken as a measure of tube solubility, was roughly the same for both types of tube and was larger than that of the other solvents. DMF was similar to DCE for arc discharge tubes but much lower for HiPco tubes. It is suggested that the non polar DMF had greater difficulty in dispersing the HiPco tubes due to an increased binding energy between the tubes in the bundles resulting from the increased chemical activity of the individual tubes due to the smaller tube diameter. From visual observation, in all 3 solvents the arc-discharge tubes went into dispersions

more readily than the HiPco tubes. The impurity content of the arc-discharge tubes is greater than the HiPco tubes and this may reduce the bundle packing density and aid the dissolution process. The extinction coefficient values for toluene were clearly less than either DCE or DMF for both tube types.

The dispersion limit for both DCE/HiPco and DCE/arc discharge dispersions was found to be 2.0±0.5 $x10^{-5}$ kg/L. The average bundle size for HiPco tubes had previously been found to be 30 nm. Using AFM it was found that below the dispersion limit the average bundle size had fallen to 2-3 nm. Single tubes were also found.

The Raman studies showed that the bundled samples were found to contain both semiconducting and metallic tubes, which were found to be resonant at different laser energies. Although the initial study of the bundled tubes was carried out using three laser lines, 488 nm, 514.5 nm and 633 nm, most of the interesting changes are observed between the spectra obtained using 514.5 nm and 633 nm as source. All future work was carried out using only these laser lines.

Notably, it was found was that although the samples were bundled, the characteristics of individual tubes could still be seen. This indicated that even though bundling perturbs the Raman spectra by inhomogeneous broadening, and damping due to the constained local environment, within the samples contributions of specific tubes could still be determined. Specifically, this was

observed through deconvolution of the RBMs and the shape and size of the G-line.

A concentration dependent study of the debundled samples showed that in addition to the accepted upshifts in the RBMs being indicative of debundling as reported in literature, upshifts also occur in all the characteristic Raman lines. The upshifts occurred abruptly in the regions of the dispersion limit, which was calculated using the absorption spectroscopy. The fact that some degree of shifting was observed at all concentration levels suggests that Raman is more sensitive to small changes in bundle size than absorption spectroscopy. A novel approach using the ratios of the characteristic line intensities was also shown to exhibit discontinuities at the dispersion limit. Such discontinuities are indicative of debundling and occurred regardless of the excitation energy used. However, the changes were more pronounced for the metallic nanotube spectra. Where debundling occurred, there was a narrowing and eventual loss of the Breit-Wigner-Fano lineshape associated with metallic nanotubes. This is due to a reduction and eventual loss of the intertubular plasmon phonon coupling originally responsible for the lineshape. FWHM values for the D and G*- lines were smaller in value than in the case of bundled tubes. Reduction in the relative size of the G*- line in metallic spectra was also found to be indicative of debundling.

The temperature dependent study showed that all characteristic lines downshifted with increasing temperature regardless of whether the samples were bundled or not. In the bundled samples the temperature coefficients were

similar for both the G and D modes for semiconducting tubes but different for metallic tubes due to the effects of electron phonon coupling. The larger value of temperature coefficient for the D-line suggested that the electron phonon coupling was temperature dependent. This in fact was shown to be the case. The temperature coefficient for the G*- line was found to be much larger than any of the other measured coefficients in the debundled samples. Downshifts were observed in the RBMs in both the Stokes and the anti-Stokes. Additional RBMs become visible at higher temperatures due to the shifting of the optical transition energies with temperature.

As a result of these studies two equations are proposed which can be used to find the characteristic line position (phonon mode frequency) in the Raman spectrum of a single walled carbon nanotube, one depending on the temperature of the sample and the second depending on the level of bundling. The first is

$$\omega = \omega_0 - \alpha\ T$$

where ω_0 is the frequency at 0K, and α is the temperature coefficient. The second is

$$\omega = \omega_{ST} - A$$

where ω_{ST} is the frequency of a single tube and A is a damping factor which is a function of the bundle size (and possibly tube diameter). The highest frequency for a characteristic line will be at 0 K for a single tube.

The intensity of the Raman spectral features reduces with increasing temperature due to increased phonon-phonon interaction. This reduction in the intensity is not as strong in metallic bundles due to weakening plasmon – phonon coupling with increased temperature. Measuring the FWHM values of the G^-- line, the longitudinal optical, LO, phonon mode, allowed the phonon relaxation times to be measured. From this the phonon mean free paths could be calculated. The mean free path due to Plasmon-phonon scattering in HiPco tube bundles was calculated at 83 K and 303 K to be 0.08 μm and 0.10 μm and the mean free path due to electron-phonon scattering in debundled HiPco tubes at 83 K and 303 K to be 0.08 μm and 0.07 μm. This shows that the interaction of phonons with electrons and plasmons are different. It also suggests that at room temperature bundled metallic tubes have better transport properties than single tubes.

Throughout this study the dominance of the G*-line in the metallic tube spectra of both bundled and debundled tubes was noticeable. Normalisation of the Raman spectra for different temperatures showed the G*-line in metallic tubes to have an additional electron – phonon coupling component not found in any of the other characteristic lines. This explains its dominance in metallic tube spectra.

In conclusion it is evident that Raman spectroscopy can be used to carry out a much needed systematic study of carbon nanotube samples. Although the Raman spectrum of bundles of tubes looks like that of single tubes, with small perturbations, there are differences which can be evaluated and which are of

importance when it comes to studying the fundamental properties of carbon nanotubes.

Appendix 1

Tube	Diameter	E_{ii}	E_{Stokes}	$E_{anti\text{-}Stokes}$
(6,6)	0.81	3.12	3.32	2.92
(10,1)	0.83	3.05	3.25	2.85
(9,3)	0.85	2.98	3.18	2.78
(8,5)	0.89	2.84	3.04	2.64
(12,0)	0.94	2.69	2.89	2.49
(7,7)	0.95	2.66	2.86	2.46
(11,2)	0.95	2.66	2.86	2.46
(10,4)	0.98	2.58	2.78	2.38
(9,6)	1.02	2.48	2.68	2.28
(13,1)	1.06	2.39	2.59	2.19
(12,3)	1.08	2.34	2.54	2.14
(8,8)	1.09	2.32	2.52	2.12
(11,5)	1.11	2.28	2.48	2.08
(10,7)	1.16	2.18	2.38	1.98
(15,0)	1.18	2.14	2.34	1.94
(14,2)	1.18	2.14	2.34	1.94
(13,4)	1.21	2.09	2.29	1.89
(9,9)	1.22	2.07	2.27	1.87
(12,6)	1.24	2.04	2.24	1.84
(11,8)	1.29	1.96	2.16	1.76
(16,1)	1.29	1.96	2.16	1.76
(15,3)	1.31	1.93	2.13	1.73
(14,5)	1.34	1.89	2.09	1.69
(10,10)	1.36	1.86	2.06	1.66
(13,7)	1.38	1.83	2.03	1.63
(18,0)	1.41	1.79	1.99	1.59
(17,2)	1.42	1.78	1.98	1.58
(12,9)	1.43	1.77	1.97	1.57
(16,4)	1.44	1.76	1.96	1.56
(15,6)	1.47	1.72	1.92	1.52
(11,11)	1.49	1.70	1.90	1.50
(14,8)	1.51	1.68	1.88	1.48
(19,1)	1.53	1.65	1.85	1.45
(18,3)	1.54	1.64	1.84	1.44
(17,5)	1.56	1.62	1.82	1.42
(13,10)	1.56	1.62	1.82	1.42
(16,7)	1.6	1.58	1.78	1.38

Stokes and anti-Stokes resonance energies for metallic tubes in the diameter range 0.81 nm to 1.60 nm

Publications

[1]“Stokes/anti-Stokes Raman spectroscopy of HiPco single –walled carbon nanotubes”, E. Gregan, S.M. Keogh, T.G. Hedderman, B. McCarthy, G. Chambers, H.J Byrne, International Winterschool on Electronic Properties of Novel Materials, Kirchberg, Austria, March (2002).

[2]“Raman studies of polymer – HiPco SWNT composites” S.M. Keogh, T.G. Hedderman, A.B. Dalton, B. McCarthy, E. Gregan, G. Chambers, H.J. Byrne. International Winterschool on Electronic Properties of Novel Materials, Kirchberg, Austria, March (2002).

[3]“Specific interaction of SWNTs with small organic molecules” T.G. Hedderman, L. O’Neill, S.M. Keogh, B. McCarthy, E. Gregan, G. Chambers, H.J. Byrne. International Winterschool on Electronic Properties of Novel Materials, Kirchberg, Austria, March (2002).

[4]“Single wall carbon nanotubes as templates for organic molecules”, T.G. Hedderman, L. O’Neill, A. Maguire, S.M. Keogh, E. Gregan, B. Mc Carthy, A.B. Dalton, G. Chambers, H.J. Byrne, “Opto-Ireland 2002, Optics and Photonics Technologies and Applications”, W.J. Blau, J.F. Donegan, A.F. Duke, B.D. MacCraith, J. A. McLaughlin, N.D. McMillan, G.M. O’Connor, E. O’Mongain and V. Toal eds., SPIE Proceedings

[5]“Physical Interactions between HiPco SWNTs and Semi-Conjugated Polymers” S.M. Keogh, A Maguire, T.G.Hedderman, E Gregan, G Farrell, AB Dalton, B McCarthy, G Chambers, H.J Byrne, “Opto-Ireland 2002, Optics and Photonics Technologies and Applications”, W.J. Blau, J.F. Donegan, A.F. Duke, B.D. MacCraith, J. A. McLaughlin, N.D. McMillan, G.M. O’Connor, E. O’Mongain and V. Toal eds., SPIE

[6]“Stokes/anti-Stokes Raman Spectroscopy Of HiPco Single Walled Carbon Nanotubes” E. Gregan, S.M. Keogh, T.G. Hedderman, G. Chambers, H.J. Byrne, “Opto-Ireland 2002, Optics and Photonics Technologies and Applications”, W.J. Blau, J.F. Donegan, A.F. Duke, B.D. MacCraith, J. A. McLaughlin, N.D. McMillan, G.M. O’Connor, E. O’Mongain and V. Toal eds., SPIE Proceedings Volume 4876, (2003),

[7]“The Physical Interactions Between Hipco SWNTs And Semi-Conjugated Polymers” S.M. Keogh, A. Maguire, T.G.Hedderman, E Gregan, G Chambers, HJ Byrne, Proceedings of International Winterschool on Electronic Properties of Novel Materials, Kirchberg, March (2003)

[8]“Interaction of SWNT with Simple Dye Molecules”, T.G. Hedderman, L. O’Neill, S.M. Keogh, E. Gregan, G. Chambers, H.J. Byrne, Proceedings of International Winterschool on Electronic Properties of Novel Materials, Kirchberg, March (2003)

[9]“Purification and Isolation of SWNTs”, E Gregan, SM Keogh, A Maguire, TG Hedderman, L O Neill, G Chambers, HJ Byrne, European Materials Research Society, Strasbourg, June (2003), Carbon, 42, 1031-1035 (2004)

[10]“Physical Interactions between HiPco single walled carbon nanotubes and Semi Conjugated Polymers” S.M. Keogh, T.G Hedderman, E.Gregan, G. Chambers, H.J Byrne. J. Phys. Chem. B, 108,

[11]“The Solubilisation of SWNT with Organic Dye Molecules.” Theresa G. Hedderman*, Sinead M. Keogh, E Gregan, Gordon Chambers, Hugh J. Byrne, J. Phys. Chem. B108, 18860-18865 (2004)

[12]“Temperature Dependent Spectroscopic studies of HiPco SWNT composites.” S.M. Keogh, T.G. Heddermann, M. Ruether, E. Gregan, G.F. Farrell,G. Chambers ,H.J. Byrne, Synth. Metals, 154, 289

[13]“Temperature induced nucleation of poly (p-phenylene vinylene-co-2, 5-dioctyloxy-m-phenylene vinylene) crystallization by HiPco Single-Walled Carbon Nanotubes”, S.M. Keogh, T.G Hedderman, M.G. Rüther, F.M. Lyng, E.Gregan, G. F. Farrell, G. Chambers, H.J Byrne, J. Chem. Phys. B, 109 (12): 5600-5607 (2005)

[14]“Use of Raman Spectroscopy in the investigation of debundling of single walled carbon nanotubes”, E. Gregan, S.M. Keogh, T.G. Hedderman, G. Chambers, H.J. Byrne, in the Proceedings of OptoIreland 2005, SPIE vol 5826, 56 (2005)

[15]“Fluorescence concentration studies of HiPco SWNTs and Semi-Conjugated Polymers”, S..M. Keogh, T.G.Hedderman, E. Gregan, G. Farrell , P. Lynch, G. Chambers, F.M. Lyng, H.J Byrne, in the Proceedings of OptoIreland 2005, SPIE vol 5826, 67 (2005)

[16]“Effects of chlorinated aromatic solvents on the dispersion of HiPco SWNTs” Q. Cheng, S. Debnath, E. Gregan and H. J. Byrne, Phys. Stat. Sol. (b), 245, 1947-1950 (2008)

[17]"Effect of solvent solubility parameters on the dispersion of Single-walled carbon nanotubes" Q.Cheng, S. Debnath, E. Gregan, H. J. Byrne, J. Phys. Chem. C, 112, 20154-20158 (2008)